Toward fast and robust *in vivo* MR quantification of microvasculature

SoHyun Han

Department of Biomedical Engineering

Graduate School of UNIST

2016

Toward fast and robust *in vivo* MR quantification of microvasculature

SoHyun Han

Department of Biomedical Engineering

Graduate School of UNIST

Toward fast and robust *in vivo* MR quantification of microvasculature

A thesis/dissertation
submitted to the Graduate School of UNIST
in partial fulfillment of the
requirements for the degree of
Doctor of Philosophy of Science

SoHyun Han

12. 04. 2015 of submission
Approved by

Advisor
HyungJoon Cho

Toward fast and robust *in vivo* MR quantification of microvasculature

SoHyun Han

This certifies that the thesis/dissertation of SoHyun Han is approved.

12. 04. 2015 of submission

Advisor: HyungJoon Cho

GilJin Jang

Woongkyu Jung

Taekwan Lee

SeYoung Chun

Abstract

Magnetic resonance imaging (MRI) assessments of microvascular anatomy and function in diseases, such as cancer and neurodegenerations are important for detecting abnormal vascular behavior and monitoring therapeutic progress in a noninvasive manner. In MRI, quantitative microvascular biomarkers such as vessel permeability, orientation, blood volume, vessel size index are actively being developed for *in vivo* applications.

Firstly, quantitative vessel permeability information is typically measured by dynamic contrast enhanced (DCE) – MRI, which uses extravasating contrast agent (Gd-DOTA). Following pharmacokinetic modelling is usually applied to dynamical signal change curve after the administration of contrast agent to extract vessel-permeability related parameters. On the other hand, it is generally accepted that there are certain limitations in conventional DCE – MRI acquisitions in terms of its accuracy, and the acquisition speed due to the demanding spatio-temporal tradeoffs for dynamic studies. For example, gradient echo based sequence is typically used for DCE – MRI for high temporal resolution requirements, but induces T_2^* decay that we often neglect, but becomes significant for high contrast agent concentration regions such as artery or kidney. Tradeoff between spatial and temporal resolution also limits the desired spatial coverage or temporal accuracy of time intensity curves. Secondly, vessel orientation, blood volume, and vessel size index are usually measured by detecting transverse relaxation difference before and after the administration of intravascular T_2 contrast agent, such as superparamagnetic iron oxide nanoparticles (SPION). However, transverse relaxation is well known to be affected by unwanted environmental conditions such as air-tissue interface and vessel orientation, which frequently causes severe error in the measurement of blood volume and vessel size index.

The subjects and goals of this thesis can be categorized by two sub-sections. In the first section, fast and accurate DCE – MRI was achieved by applying compressed sensing (CS) algorithms, which mitigates the spatio-temporal resolution competition of dynamic acquisitions. Firstly, the optimization for the implementation of compressed sensing to conventional fast low-angle shot (FLASH) sequence which is generally used for DCE – MRI acquisition was performed. After optimization step, temporal or spatial resolution improvements were demonstrated by *in vivo* experiment, especially in the tumor model. Secondly, compressed sensing was implemented to turbo spin echo (TSE) sequence to minimize transverse artifact by replacing T_2^* to T_2 without reducing temporal resolution and slice coverage. This minimized transverse artifact realized calibration-free T_1 estimation from T_1-weighted signal intensity. Finally, ultrafast 3D spin echo acquisition was developed by applying compressed sensing to multiple-modulation-multiple-echo (MMME) sequence. Improved enhancement in developed sequence was observed, compared to conventional FLASH sequence with 3D coverage.

In the second section, alternative methods to improve accuracy in detecting vessel orientation, blood volume, and vessel size index were developed. Firstly, alternative way to measure blood volume, and vessel size index was suggested and demonstrated by using ultra-short echo time (UTE) sequence. UTE sequence realized the measurement of blood volume with the change of longitudinal relaxation before and after administration of contrast agent, not from that of transverse relaxation. Consequently, accurate blood volume measurement was achieved by longitudinal relaxation which is not sensitive to environmental conditions such as air-tissue interface and vessel orientation. Moreover, alternative vessel size index including longitudinal relaxation showed the potential to reduce the error from environmental conditions. Finally, the new concept of obtaining MR tractography with magnetic field anisotropy was introduced. Compared to the conventional way using susceptibility-induced anisotropic magnetic field inhomogeneity studies, this method doesn't need re-orientation of the subject utilizing the interference pattern between internal and external field gradients.

Developed several methodologies in this thesis for the fast and robust *in vivo* quantification of microvasculature such as vessel permeability, orientation, blood volume, and vessel size index demonstrated the potentials to improve not only the speed of acquisition but also the accuracy of the *in vivo* microvascular measurements via efficient sensing and reconstruction MR techniques.

Contents

List of figures

3.3 Improved contrast enhancement using ultrafast 3D spin-echo acquisition with CS-MMME

Chapter 4. Alternative methods to improve accuracy in detecting microvasculature

4.1 Robust assessment of cerebral blood volume and mean vessel size using SPION

4.2 MR tractography using magnetic field anisotropy

List of tables

Chapter 1. Introduction

1.1 Purpose

The goal and content of the research can be summarized into two distinct subjects. One is to **develop fast and accurate DCE – MRI methods** to improve both temporal and spatial resolutions without deteriorating one of them by employing compressed sensing sensing/reconstruction algorithms. The other is to develop and apply **the alternative methods to improve accuracy in quantifying microvasculatural parameters** such as vessel orientation, blood volume, and vessel size index.

The detailed objectives of research are followings:

First section includes the below topics,

(1) Temporal/spatial resolution improvement with compressed sensing optimized FLASH

(2) Temporal resolution improvement of calibration-free DCE – MRI with CS-TSE

(3) Improved contrast enhancement using ultrafast 3D spin-echo acquisition with CS-MMME

Second section included the below topics,

(1) Robust assessment of cerebral blood volume and mean vessel size using SPION

(2) MR tractography using magnetic field anisotropy

1.2 Outline

The thesis begins with the introduction of the overall research theme in Chapter 2. Firstly, the image formation in MRI is elaborated to understand how the image is formed. Secondly, basic concepts of fast imaging methods (FLASH, TSE, and MMME), dealt in this thesis are explained. Thirdly, the theory of compressed sensing is described because this theory is applied to the FLASH, TSE, and MMME sequences for realizing sparse sampling and reconstruction scheme to conventional fast imaging techniques. Finally, the basic concept of DCE – MRI and its importance in perfusion measurements are described. Next, Chapter 3 is focused on describing the development and application of fast and accurate DCE – MRI, employing compressed sensing techniques. The optimization and the *in vivo* applications of compressed sensing algorithms to FLASH, TSE, and MMME are described. In Chapter 4, the improvement of the accuracy in quantification of microvascular parameters, such as vessel orientation, blood volume, and vessel size index is elucidated. Finally, the summary and conclusions of this thesis work is explained in Chapter 5, suggesting the potentials of developed methods to accelerate the speed of acquisition with enhanced accuracy in the quantification of *in vivo* microvasculature parameters.

1.3 Abbreviations

AIF	Arterial input function
ADC	Apparent diffusion constant
CA	Contrast agent
CBV	Cerebral blood volume
CCC	Concordance correlation coefficient
CE	Contrast enhanced
CS	Compressed sensing
DCE-MRI	dynamic contrast enhanced – magnetic resonance imaging
DCT	Discrete Cosine transforms
DSC	Dynamic susceptibility contrast
DTI	Diffusion tensor imaging
DWT	Discrete Wavelet transforms
EPI	Echo planar imaging
ETL	Echo train length
FA	Flip angle
FLASH	Fast low-angle shot
FOV	Field of view
FPM	Finite perturber method
GE	Gradient echo
IRSE	Inversion recovery spin echo
MC	Monto carlo
MEGE	Multi echo gradient echo
MMME	Multiple modulation multiple echo
MSME	Multi slice multi echo
mVSI	mean Vessel size index
MVV	Microvascular volume
NA	Number of averages
NR	Number of repetitions
PFG	Pulsed field gradient
RARE	Rapid acquisition with relaxation enhancement
ROI	Region of interest
SE	Spin echo
SNR	Signal to noise ratio

SPION	Superparamagnetic iron oxide
SR	Signal ratio
TE	Echo time
TI	Inversion time
TR	Repetition time
TSE	Turbo spin echo
TTP	Time to peak
UTE	Ultra-short echo time

Chapter 2. Background

2.1 Image formation (*k*-space)

The signal from the excited spins with a transverse component in the presence of the change in magnetic field corresponds to a Fourier transform of the effective spin density along the gradient direction. The transform variable is the spatial frequency called k_r in the direction of r. With transform variable, we can express the Fourier transform of the spin density in *k*-space. The signal from an excitation with a set of three orthogonal gradients can be represented as follows,

$$s(\vec{k}) = \int \rho(\vec{r}) e^{-2\pi i \cdot \vec{k} \cdot \vec{r}} d^3 r \qquad (2.1.1)$$

where *k* vector is defined as,

$$k_x(\mathrm{t}) = \frac{\gamma}{2\pi}\int^{t'} G_x(t')dt' \,, k_y(\mathrm{t}) = \frac{\gamma}{2\pi}\int^{t'} G_y(t')dt' \,, k_z(\mathrm{t}) = \frac{\gamma}{2\pi}\int^{t'} G_z(t')dt' \qquad (2.1.2)$$

Generally, the *x* direction is called frequency encoding dimension and the *y*, *z* directions are defined as the phase/slice encoding dimension. The following sequence diagram in **Figure.2.1.1(A)** is for 2D *k*-space mapping example. This diagram is for the case of non-slice selective RF pulse to cover 2D *k*-space shown in **Figure.2.1.1(B)**.

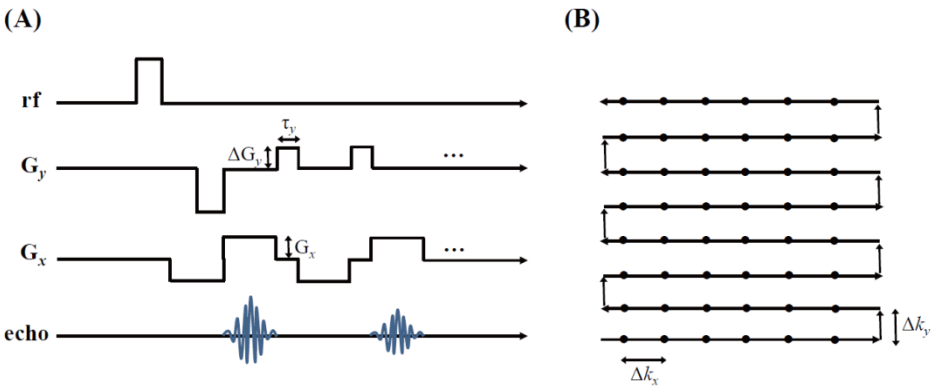

Figure 2.1.1 (A) Pulse sequence diagram of 2D imaging of gradient echo. *x* gradient is rewound to recover echoes. The phase encoding gradient (G_y) is applied after acquiring echoes. **(B)** *k*-space diagram for 2D imaging. Each dot represents a sampled point and the interval is determined by G_x and dwell time.

G_x and G_y correspond to horizontal and vertical lines in **Figure.2.1.1(B)**, respectively. The readout sampling through the horizontal line is carried out with discrete measurement for each Δt, which is called dwell time. The interval in the k_x direction can be calculated as,

$$\Delta k_x = \frac{\gamma}{2\pi} G_x \Delta t \qquad (2.1.3)$$

After one horizontal line is sampled, vertical line is shifted by applying phase encoding gradient represented as Δk_y.

$$\Delta k_y = \frac{\gamma}{2\pi} \Delta G_y \tau_y \qquad (2.1.4)$$

τ_y is the duration of phase encoding gradient as depicted in **Figure.2.1.1(A)**. By repeating these steps, two dimensional *k*-space can be filled for Cartesian coordinate system.

2.2 Fast imaging sequences

2.2.1 Fast low-angle shot (FLASH)

As one of the fast imaging methods, fast gradient echo imaging sequence which is called fast low-angle shot (FLASH) [1] with very short repetition time (TR) will be discussed in this section. The schematic sequence diagram for FLASH is shown in **Figure 2.2.1**. In this pulse sequence, the residual transverse magnetization after acquiring echo is typically removed by a spoiler gradient along the slice direction. The amplitude of the spoiler gradient is varied to avoid coherence buildup in the transverse magnetization before the next excitation step.

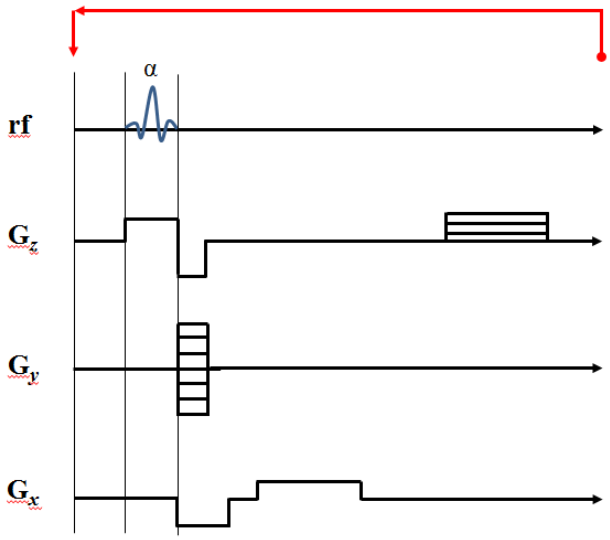

Figure 2.2.1 Sequence diagram of FLASH. The residual transverse magnetization after acquiring echo is removed by a spoiler gradient in the slice direction. The amplitude of the spoiler gradient is varied to nullify the existence of transverse coherence.

The steady-state signal from a repetitive RF pulses assumes that repetition time (TR) << T_2, therefore, transverse magnetization before next rf pulse is non-zero. In other words, the transverse magnetization after the encoding with very short TR has not been completely dephased before the next encoding step. By applying spoiling gradient, we can eliminate remained transverse magnetization for the simplicity of signal behavior. The steady-state signal intensity equation with completely spoiling transverse magnetization can be expressed as follows

$$S_{ss} = S_0 \frac{1-e^{-TR/T1}}{1-cos\alpha e^{-TR/T1}} sin\alpha \cdot e^{-TE/T_2^*} \qquad (2.2.1)$$

where S_{ss} is the steady-state signal intensity, S_0 is proton density intensity, α is flip angle, TR is repetition time, TE is echo time, T_1 is longitudinal relaxation time, and T_2^* is gradient echo induced transverse relaxation time. This equation reflects that the signal intensity is dependent upon the acquisition parameters, such as flip angle and TR along with intrinsic longitudinal and transverse relaxation times.

2.2.2 Turbo spin echo (TSE)

As one of the fast imaging methods, fast spin echo imaging, which is called turbo spin echo (TSE) [2] will be discussed in this section. The schematic sequence diagram for TSE is shown in **Figure 2.2.2**. In this pulse sequence, *N* echoes can generated by applying *N* 180° rf pulses in TR loop.

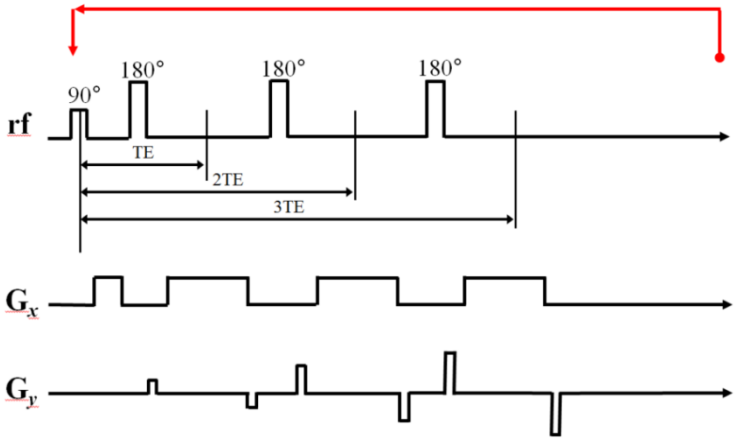

Figure 2.2.2 Sequence diagram of TSE. This example generates 3 echoes after 90° pulse. Each echo is encoded to different position of *k*-space line.

If a total number of encoding is N_{enc} and *N* echoes are encoded to different *k*-space line, the number of excitations (N_{exc}) can be reduced by

$$N_{exc} = \frac{N_{enc}}{N} \qquad (2.2.2)$$

Therefore, a factor of *N* called turbo factor can accelerate the speed of scan time compared to the

conventional spin echo imaging. On the other hand, turbo factor should be carefully selected because T_2 effect is inevitably contained at later echoes and associated imaging blurring artifacts may arise with echo train imaging without multiecho compensation

2.2.3 Multiple Modulation Multiple Echo (MMME)

As one of the fast imaging methods, multiple modulation multiple echo (MMME) sequence [3] will be discussed in this section. The generation of multiple echoes by separating a few RF pulses properly and applying magnetic field gradient is well characterized by a coherence pathway formalism. The schematic sequence diagram for MMME with five RF pulses is shown in **Figure 2.2.3**.

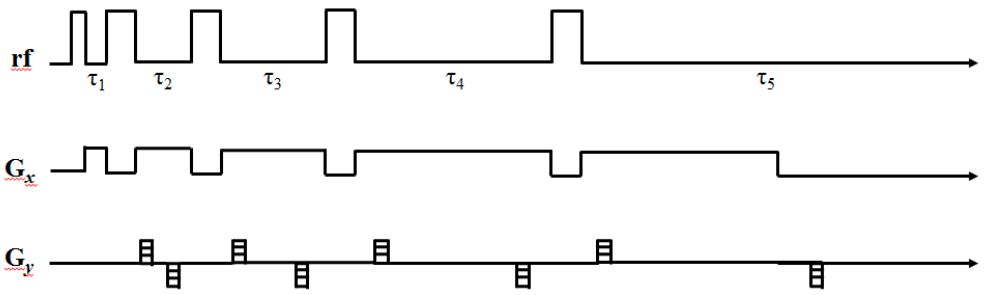

Figure 2.2.3 Sequence diagram of MMME with five rf pulses.

A magnetic field gradient (G_x) creates a modulation of the magnetization and RF pulses result in a rotation and splitting transverse and longitudinal magnetizations. Consequently, a number of several coherence pathways exist even with a small number of RF pulses. Theoretically, the different coherence pathways with *N* RF pulses are able to form *n* echoes with the following equation,

$$n = \frac{3^{(N-1)}-1}{2} + 1 \qquad (2.2.3)$$

When τ_2 is set to $3\tau_1$, all echoes are formed with interval τ_1. In the same way, the time periods of τ_2, τ_3, τ_4 as $3\tau_1$, $9\tau_1$, and $27\tau_1$ will maintain the echo spacing of τ_1 to maximize the number of echoes for given number of RF excitations, which constitutes the most economical echo generation with minimized RF excitations

2.3 Compressed sensing (CS)

In general, images are able to be compressed without significant loss of information [4]. Especially, medical images are known to be compressible even though compression in medical images was avoided [5-6]. Compression by using transformations is well-accepted strategy in JPEG, JPEG-2000, and MPEG. For example, first, sparsifying transformation is applied to the image, then, the image is converted to the vector of sparse coefficients. After that, the only partial significant coefficients are selected. The examples of sparsifying transformations are Discrete Cosine transforms (DCT) for JPEG and Discrete Wavelet transforms (DWT) for JPEG-2000 [4]. Fortunately, magnetic resonance images have been well known to be sparse in many transformations like Fourier or wavelet [7-9]. For example, in the case of angiograms which depict blood vessels of the body, images primarily show only blood vessels and other regions are void, which means images are already sparse even in image domain. Moreover, dynamic MR images are also able to be highly compressed by taking advantage of sparsity in temporal Fourier transformation domain with the assumption that dynamic process is somewhat periodic along the temporal domain

There are two advantageous properties in MR images, which enable successful CS application. One is transform sparsity. As mentioned above, MR images can be sparse with sparsifying transformations such as Fourier or wavelet. The other is incoherence of under-sampling artifacts. Satisfying incoherence by random under-sampling results in noise-like artifact in the image. After satisfying those two requirements, nonlinear reconstruction is performed to enforce both sparsity and consistency of the reconstruction.

Nonlinear reconstruction is performed by minimizing the l_1-norm of the compressed reconstruction which is constrained to match the acquired data by solving the following optimization equation,

$$minimize \ \|\Psi s\|_1 \qquad (2.3.1)$$

$$subject\ to \ \|Fs - k\|_2 < \varepsilon \qquad (2.3.2)$$

where the reconstruction image is a vector s and Ψ is the transformation operator which is a sparsing representation such as Fourier or wavelet transformations. k is under-sampled k-space, F is the under-sampled Fourier transform, and ε is the constraint which can control the fidelity of the reconstruction to the measured data and is set to below the noise level of k-space.

Minimizing $\|\Psi s\|_1$ boosts sparsity [10], and the constraint (2.3.2) reinforces the reconstruction consistency.

2.4 Dynamic contrast enhanced (DCE) – MRI

DCE – MRI is fast T_1-weighted imaging method by minimizing TR for given geometry and required slice coverage. DCE – MRI methodologies are often used to characterize tumor perfusion biology and its treatment response because this method provides good temporal and spatial resolution information of vascular permeability [11]. The direct advantages of DCE – MRI based on the facts that quantitative parameters can be extracted by pharmacokinetic modelling, which can give the biologically relevant information and robust measurement without variation by environmental factors such as the scanner system, injection dose, weight and so on. Before pharmacokinetic modelling application, T_1-weighted signal intensity should be converted to concentration of contrast agent. To convert the signal intensity to the concentration, two components are generally required. One is intrinsic T_1 value, which should be reduced as the contrast agent concentration is increasing by the following equation,

$$\frac{1}{T_1} = \frac{1}{T_{10}} + r_1 C \qquad (2.4.1)$$

where r_1 is T_1 relaxivity, T_1, and T_{10} are longitudinal relaxations in presence and absence of contrast agent, respectively.

The other is the requirement of accurate information of RF flip angle. The most conventional and widely used pulse sequence for DCE – MRI application is FLASH acquisition whichutilizes low flip angle. The signal intensity of FLASH is clearly defined as following equation,

$$S = S_0 \frac{\left(1-e^{-\frac{TR}{T_1}}\right)\sin(FA)}{1-e^{-\frac{TR}{T_1}}\cos(FA)} \qquad (2.4.2)$$

where S_0 and S are the signal intensity before and after administration of contrast agent, respectively.

After converting signal intensity to the concentration in time-intensity curves, pharmacokinetic analysis can be applied to characterize the tumor perfusion biology. Usually, pharmacokinetic modelling uses the concept of compartmental modeling to simplify the biological process. The simple compartment model usually contains two compartmentations for vessel and tissue, which is called Tofts model [12], and the schematic of corresponding two-compartment model is shown in **Figure 2.4.1**.

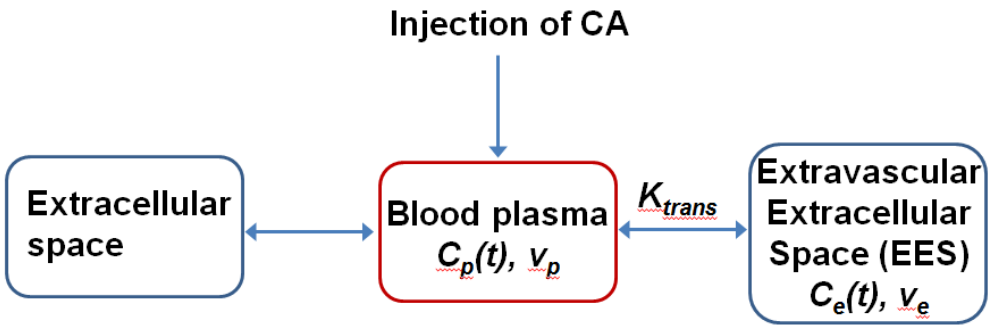

Figure 2.4.1 Schematic of two compartment model called Tofts model.

Chapter 3. Fast and accurate DCE – MRI with compressed sensing

3.1 Temporal/spatial resolution improvement with compressed sensing optimized FLASH

3.1.1 Introduction

Dynamic contrast-enhanced magnetic resonance imaging (DCE – MRI) gives important information with respect to tumor perfusion and permeability by time series acquisition of signal increase after the administration of contrast agent (CA) [13-18]. Usually, the CA arrives faster and larger in well-perfused, highly vascular and permeable regions. This vascular perfusion and permeability information of tumor is able to be obtained from pharmacokinetic modeling of DCE – MRI data [19-20]. To realize accurate and reproducible measurements of this information, both temporal and spatial resolutions are required [13-16]. On the other hand, there is a limit to improve spatial resolution maintaining enough temporal resolution to represent time series information with conventional data acquisition methods. For example, the negative effect of poor temporal resolution in determination of the pharmacokinetic parameters has been simulated and shown in previous study [21].

Recently, compressed sensing (CS) has proved that only a small fraction of the samples is sufficient to reconstruct sparse or compressible signals [22-24]. Fortunately, magnetic resonance images have been well known to be sparse in various transformations such as Fourier or wavelet [25-27]. Therefore, CS has potential to improve spatial and temporal resolutions simultaneously so that we can enhance the accuracy in extracting perfusion/permeability information in DCE – MRI. Previously, several simulations from fully sampled DCE – MRI data have been conducted [28-35]. However, the actual implementation of CS to pulse sequence has not been done for *in vivo* DCE – MRI studies, which can directly prove the feasibility of CS application to DCE – MRI.

In this work, we demonstrated the implementation of *in vivo* DCE – MRI in an animal tumor model with CS-optimized fast low angle shot (FLASH) sequence in a similar manner to k-t FOCUSS [36]. Firstly, design parameters necessary for the development of CS-FLASH sequence were optimized by simulation from fully sampled DCE – MRI data of animal tumors. Secondly, the CS-optimized phase encoding scheme was implemented to the conventional FLASH sequence and water phantom experiments were performed to check the feasibility of CS-FLASH sequence. Finally, *in vivo* DCE –

MRI acquisition was performed on mouse flank tumor xenografts. Temporal resolution improvement was shown by comparing uptake curves and spatial resolution improvement was demonstrated by comparing Ak_{ep} maps from the CS-FLASH sequence with those obtained from the conventional FLASH sequence.

3.1.2 Materials and Methods

Optimization of CS-FLASH parameters for acquisition and reconstruction

CS application to DCE-MRI can be primarily described as the reconstruction of dynamic images from under-sampled data by optimizing for the sparsity under the predetermined compressive transformation. Sparse reconstruction is achieved by minimizing the l_1-norm of the compressed reconstruction which is constrained to match the acquired data by solving the following optimization problem,

$$minimize \ \|\Psi s\|_1 \qquad (3.1)$$

$$subject\ to \ \|Fs - k\|_2 < \varepsilon \qquad (3.2)$$

where the reconstruction image is a vector s and Ψ is the transformation operator which is a sparse representation such as Fourier or wavelet transformations. k is the undersampled k-space, F is the undersampled Fourier transform, and ε is the constraint which can control the fidelity of the reconstruction to the measured data and is usually set to below the noise level of k-space.

For the implementation of CS-FLASH for dynamic studies, five variables were optimized, which are (i) the optimal compressive transformation, (ii) the under-sampling scheme for the phase encoding, (iii) the incoherent sampling scheme for the temporal domain, (iv) the constraint ε, and (v) the acceleration factor. Optimizations were performed using a Dunning R3327-AT prostate tumor DCE data in a rat with heterogeneous perfusion/permeability parameters [18].

First, the optimal compressive transformation along the image and temporal domain were determined by comparing the relation between the fraction of transform coefficients and corresponding fraction of the total signal. In the second place, under-sampled data were created retrospectly from fully sampled DCE – MRI data and reconstructed with CS algorithms with various compressive transformations. By minimizing the residual values between CS reconstructed and fully sampled image, optimal transformations along the image and temporal domain were determined.

Second, the under-sampling scheme for the phase encoding was generated by keeping the center part of k-space and the remaining part of k-space were sampled following Gaussian distribution. This scheme ensures a good signal-to-noise ratio (SNR) by sampling low k values, while collecting enough

samples for higher *k* values to reconstruct the details of the image as well as maintaining sampling incoherence for CS. Different random phase encoding scheme were applied for each temporal domain to increase the incoherence for CS reconstruction as well.

Third, the optimal segment size of the sampling along the temporal domain was determined by reconstructing and comparing the reconstructed data with fully sampled data by varying the segment size. This avoids an unnecessarily large phase encoding array for CS-FLASH sequence and increases the flexibility of the implementation of the CS-FLASH sequence.

Fourth, the constraint ε handles the least square difference which impacts the total computation time required for the CS reconstructions. Generally, the constraint is set below the noise level of *k*-space, where it will add this noise in addition to the error from under-sampling. A loosened constraint would result in faster reconstruction time but inevitably cause the poor reconstruction quality because the algorithm over-compresses the image. Constraint and the reconstruction time were optimized by acquiring the residual map between CS reconstructed images with different constraints and the fully sampled image.

Finally, the acceleration factor was optimized by showing the degradation of the image quality and corresponding Ak_{ep} parameters with acceleration factors of 4, 8, 10, 12 and 16. Residual maps were calculated for both the images and Ak_{ep} maps. Pharmacokinetic modeling of the uptake curve was performed with the Hoffmann/Brix model [19] to compare Ak_{ep} value which implicates perfusion/permeability information.

All reconstructions were performed on a personal computer with an Intel Core i3 3.19-GHz central processing unit and 4GB of memory on the Windows 7 platform and the data were reconstructed by the software developed with MATLAB R2010a (MathWorks, Natick, MA, USA) by using two packages: spgl v.1.7 for the l_1-norm minimization [37] and Wavelab v.8.02 for using wavelet transform [38].

Statistical and DCE-MRI analysis

For the quantitative comparison of the image and Ak_{ep} value between fully sampled data and CS reconstructed data, the concordance correlation coefficient (CCC) value was used as a standard metric. The CCC value represents the agreement of CS reconstruction image with respect to a fully sampled image by following equation,

$$\rho_c = \frac{2\rho\sigma_x\sigma_y}{\sigma_x^2+\sigma_y^2+(\mu_x-\mu_y)^2} \qquad (3.3)$$

where σ, μ, and ρ represents to standard deviation, mean and correlation coefficient, respectively.

And Ak_{ep} value from the Hoffmann/Brix model was used for the measurement of DCE – MRI parameter. k_{ep} means the movement of contrast agent between the interstitial space and the plasma and A is the amplitude of the two compartment model. This value reflects both the degree of relative MR signal enhancement and an exchange rate, which can characterize the velocity of MR signal increase and provide relevant information regarding tumor perfusion/permeability. Ak_{ep} value was fitted with the uptake curve by the following equation [19],

$$\frac{S(t)}{S(0)} = 1 + Ak_{ep}\left(\frac{e^{-k_{ep}t} - e^{-k_{el}t}}{k_{el} - k_{ep}}\right) \qquad (3.4)$$

Implementation of CS-FLASH and application to in vivo DCE – MRI

We modified the phase encoding scheme of conventional FLASH sequence with CS-optimized phase encoding scheme to experimentally verify the improvement of spatial/temporal resolutions. Water phantom was acquired to show the functionality of the developed pulse sequence. The matrix size was 128 (read) × 128 (phase) × 32 (temporal domain) for eight slices and the experiment was performed on an 4.7 T MRI system (Bruker BioSpin, Billerica, MA, USA) at the acceleration factors of 4 and 8.

The Institutional Animal Care and Use Committee of the Korea Basic Science Institute approved the *in vivo* animal experiments conducted for this study. For the animal tumor model, U-87 MG (human glioblastoma-astrocytoma, epithelial-like) cells, suspended in phosphate-buffered saline (PBS; pH 7.4), were subcutaneously implanted into the flank of female mice (10^6 cells/0.05 ml PBS per mouse). The contrast agent Gd-DTPA (0.015 mmol/ml;Dotarem, Laboratoire Guerbet, Aulnay-sous-Bois, France) was administrated as a bolus into the tail vein, followed by the time series acquisition of the images with conventional FLASH or CS-FLASH sequences for the direct comparisons.

To verify the temporal resolution improvement at a fixed spatial resolution, the matrix size was varied according to the number of phase encoding steps and repetitions, while holding the total acquisition time constant. For three different mice, conventional FLASH, CS-FLASH(×4), and CS-FLASH(×8) were performed with the matrix size at 128×128×128, 128×32×512, 128×16×1024 (read, phase, repetitions), respectively. For all experiments, repetition time (TR) and echo time (TE) were 100, and 2.2 ms, and eight slices with 1.5 mm slice thickness were acquired.

To verify the spatial resolution improvement at a fixed temporal resolution, a longitudinal DCE – MRI study was performed. Firstly, DCE – MRI study was performed with conventional FLASH. After 5 hours later for clearing CA, DCE – MRI study was conducted with the CS-FLASH sequence with the same temporal resolution as 4.2s. TR/TE was 130/3.1 ms, and four slices with 1.5 mm slice thickness were acquired.

3.1.3 Results

Compressive transformations

To determine the optimal compressive transformation for the image, the relation between the fraction of coefficients after compression and the fraction of the total signal for water phantom and an animal tumor was shown in the top row of **Figure 3.1.1**: (blue) no transform, (green) wavelet (symlet) transform only along the image axes, (turquoise) wavelet (symlet) transform along the image axes with Haar transform along the time axis and (red) wavelet (symlet) transform along the image axes with the Fourier transform along the time axis. Wavelet transform along the image axes and the Fourier transform along the time axis were sparser than all other cases as shown in **Figure 3.1.1**. And CS reconstructed images were generated with different combination of compressive transformations. The residual image between CS reconstructed image and fully sampled image were shown in the bottom row of **Figure 3.1.1**. For a clear visualization, the maximum scale of residual images was set to 30% of the maximum signal intensity of the fully sampled image. The CCC value was calculated for each case as shown in **Figure 3.1.1**. An optimal value of CCC as 0.974 was observed for the wavelet transform along the image axes and the Fourier transform along the time axis. Based on the result, CS was reconstructed by applying the wavelet transform along the image axes and the Fourier transform along the time axis.

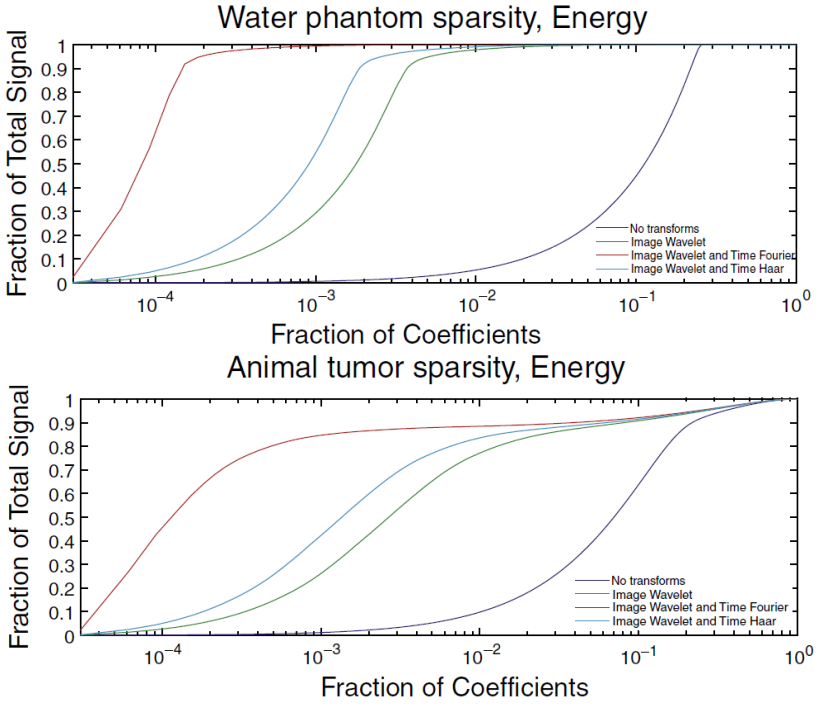

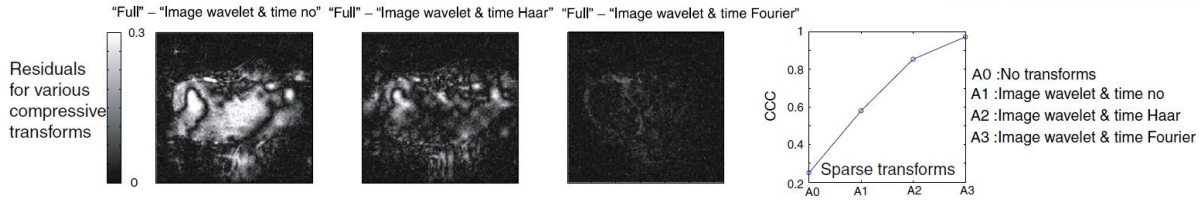

Figure 3.1.1 In the top row, the accumulated signal is plotted with respect to the corresponding fraction of coefficients for the selected transform to water phantom and an animal tumor. No transform (blue), image wavelet only (green), image wavelet (symlet) and time Haar (turquoise), image wavelet (symlet) and time Fourier (red). In the bottom row, the residual images of each CS reconstructed image from fully sampled image are shown for various transforms along with the corresponding CCC values.

Segment size in temporal domain and constraints

The segmentation of phase encoding schemes to the temporal domain can reduce the reconstruction time as it reduces the size of data for CS reconstruction. For example, the size of input data would reduce from a single vector of 128 (read)×128 (phase)×128 (repetitions) to four vectors of 128 (read)×32 (phase)×32 (repetitions) in the case, when the segment size as 32 with acceleration factor of 4. Reduced size of data resolves memory overflow problem in the spectrometer that can occur when using randomized phase encoding schemes for large number of repetitions.

To estimate an optimal segment size (*n*), each block of *n* temporal domain out of 256 repetitions was reconstructed separately, and the residual image from CS reconstructed image with respect to the fully sampled image was compared as shown in **Figure 3.1.2 (A)**. CCC values were calculated for the segment size as 1, 8, 16, 32, and 64, and the CCC value saturated near 0.974 for the segment size as 32 as shown in **Figure 3.1.2 (A)**. For this reason, the optimized segment size was set to 32.

To determine the optimal value of the constraint, we undersampled at the acceleration factor of 4 from a fully sampled DCE-MRI data, and ran CS reconstruction with a variable ε chosen based on the noise level σ and compared CS reconstruction image to the fully sampled image. No significant difference between the constraint as 2σ, σ, 0.5σ, 0.1σ was shown in the CCC value in **Figure 3.1.2 (B)**. Therefore, optimized constraint was set to noise level σ.

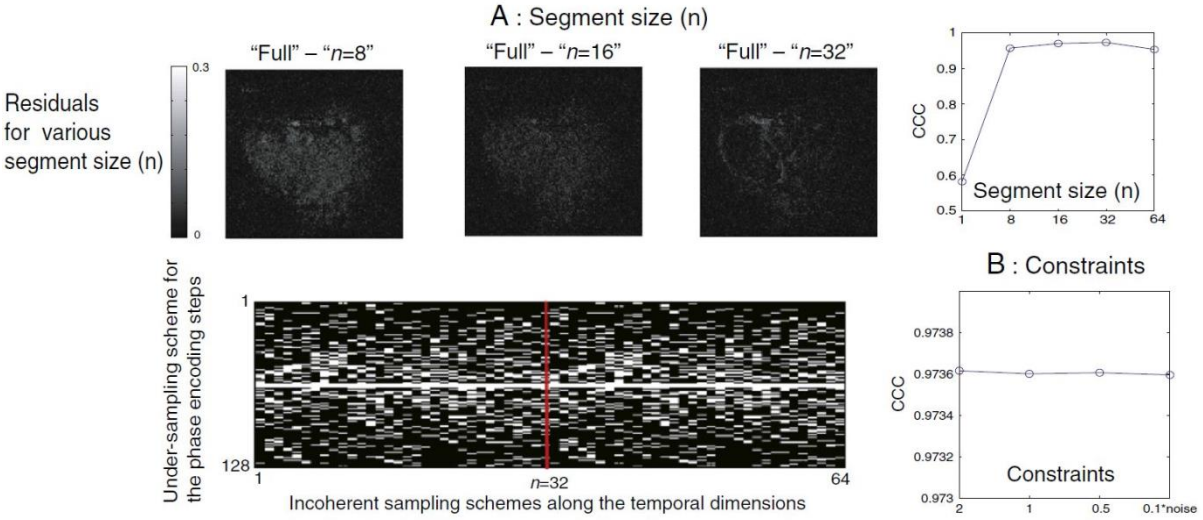

Figure 3.1.2 (A) Residual images and CCC values are shown as a function of segment size. Optimized sampling scheme of phase encoding is shown for 64 repetitions. **(B)** CCC values for CS reconstructed images with various constraints.

Acceleration factor

CS reconstruction was performed at five different acceleration factors which are 4, 8, 10, 12, and 16 with optimized compressive transformations, segment size and constraint. The residual images and corresponding CCC values for five acceleration factors were shown in **Figure 3.1.3 (A)**. There is a significant degradation of the image quality as the acceleration factor is increased, especially from the acceleration factor of 10. For this reason, the acceleration factors as 4 and 8 were selected. As an example, the fully sampled image was shown in **Figure 3.1.3 (B)** and CS reconstructed image with the acceleration factor of 4 was shown in **Figure 3.1.3 (C)**.

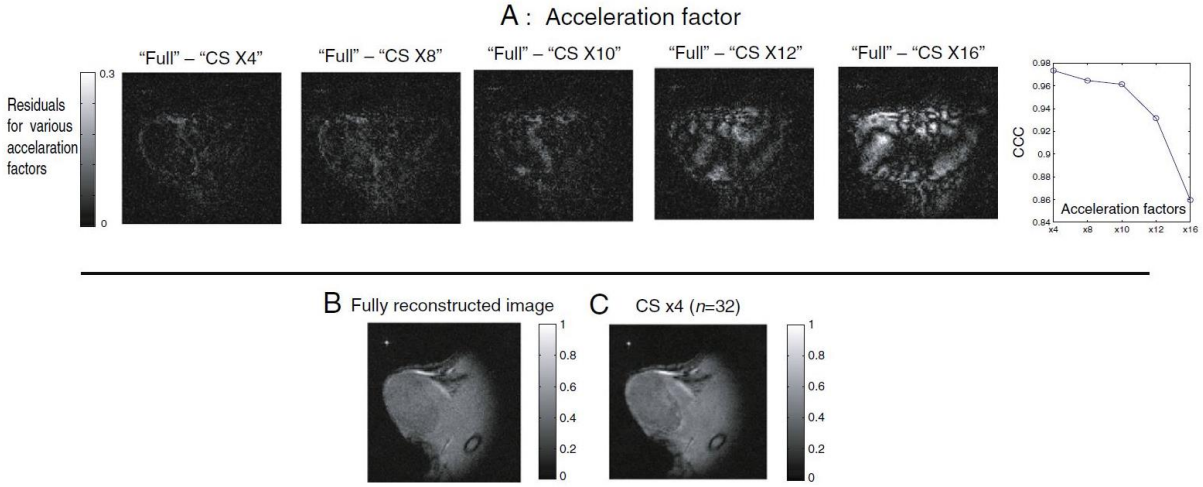

Figure 3.1.3 (A) Residual images and CCC values for five acceleration factors. **(B)** Fully sampled image. **(C)** CS reconstructed image with the acceleration factor of 4.

Correlation of Ak_{ep} map between full and CS DCE – MRI data

The feasibility of CS to DCE – MRI must be validated not only with the image quality but also with the change of the signal intensity due to the injection of CA, i.e., uptake curve, further, perfusion/permeability information (Ak_{ep}) from uptake curve. Representative uptake curves from three different regions of tumor labeled (i), (j), and (k) on Ak_{ep} map were shown in **Figure 3.1.4 (A)**. The fast (i), intermediate (j) and slow (k) initial slopes of uptake curves were shown at the acceleration factor of 4 and 8 with full data set as reference. There is no difference in uptake curve between full and CS reconstructed data, which demonstrates the feasibility of CS-FLASH for DCE – MRI even in heterogeneously perfused tumor. After that, Ak_{ep} maps with various acceleration factors were shown in **Figure 3.1.4 (B)**. High Ak_{ep} values in peripheral region and low Ak_{ep} values in the center region were appeared in CS reconstructed maps, which were consistent with Ak_{ep} map from fully acquired data set. On the other hand, residual values from full data set with CS reconstruction data were increased as the acceleration factor was increased as shown in **Figure 3.1.4 (C)**. And corresponding CCC values were plotted in **Figure 3.1.4 (E)**. A scatter plot of Ak_{ep} values from full data and CS reconstructed data with the acceleration factor of 4 in **Figure 3.1.4 (D)** represents the high correlation between them.

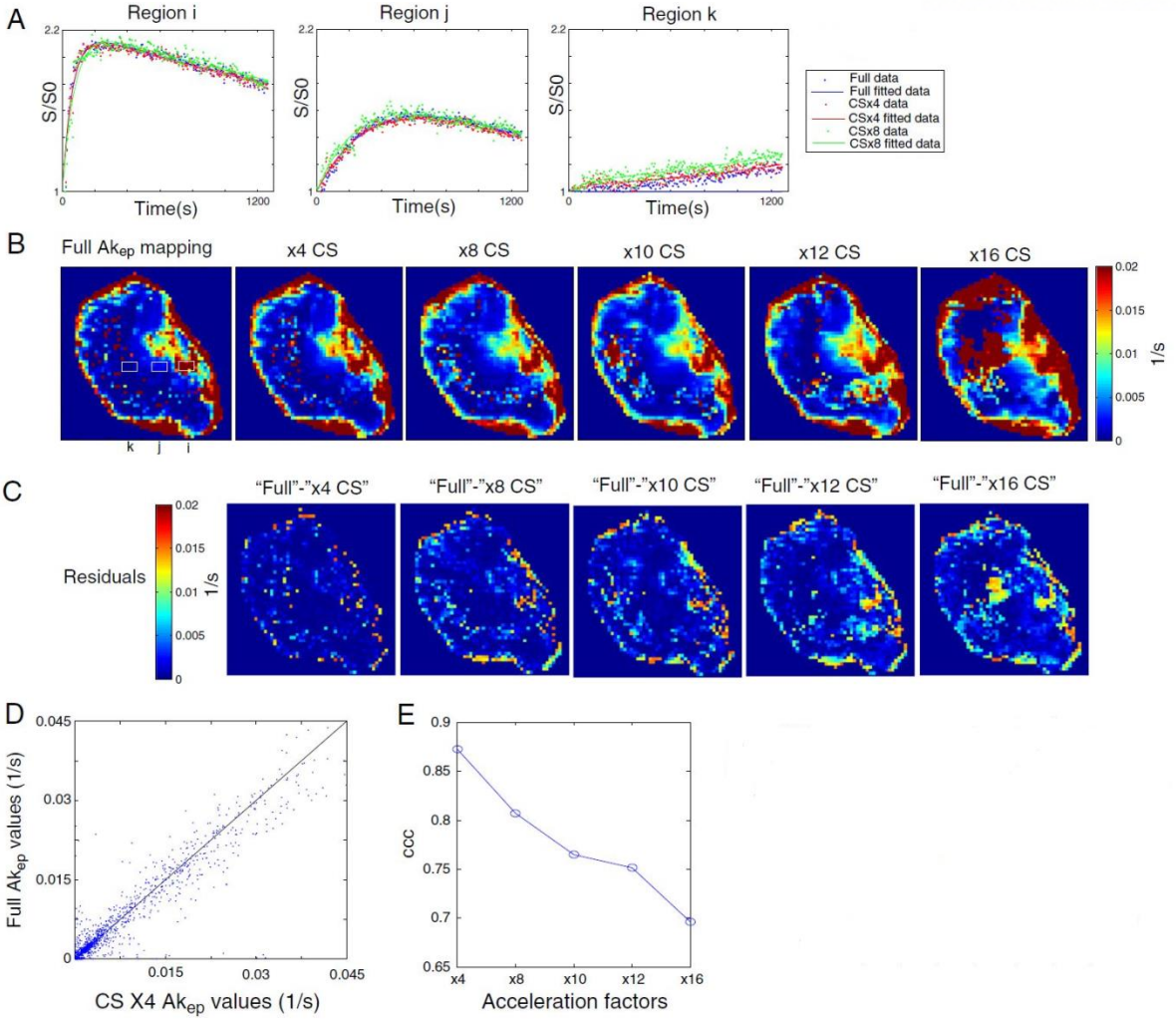

Figure 3.1.4 (A) Representative uptake curves from three different tumor regions indicated as (i), (j), and (k). Fast (i), intermediate (j), and slow (k) uptake curves are shown at full data and CS reconstructed data with the acceleration factors of 4 and 8. **(B)** Ak_{ep} maps of full data and CS reconstructed data with various acceleration factors. **(C)** Residual maps of Ak_{ep} maps from CS reconstructed data with respect to that from full data. **(D)** Scatter plot between Ak_{ep} values from CS reconstructed data with the acceleration factor of 4 and those from full data. **(E)** CCC values with varying the acceleration factors.

Feasibility of CS-FLASH in water phantom

The CS-FLASH sequence with optimal parameters was tested on a water phantom to prove the feasibility of the developed pulse sequence. Reconstructed images with CS-FLASH at acceleration factor of 4 and 8 were shown in **Figure 3.1.5 (A)**. The *k*-space from CS-FLASH acquisitions was compared with undersampled *k*-space from fully sampled *k*-space as shown in **Figure 3.1.5 (B) and (C)**. The signal intensity line profiles across the sample as indicated by the horizontal lines in **Figure**

3.1.5 (A) were compared and demonstrated that no signal loss from CS as shown in **Figure 3.1.5 (D)**. The Pearson correlation coefficients between full data and CS reconstructed data for the acceleration factors of 4 and 8 were 0.9985, and 0.9986, respectively, ensuring designed implementation of CS-FLASH acquisition.

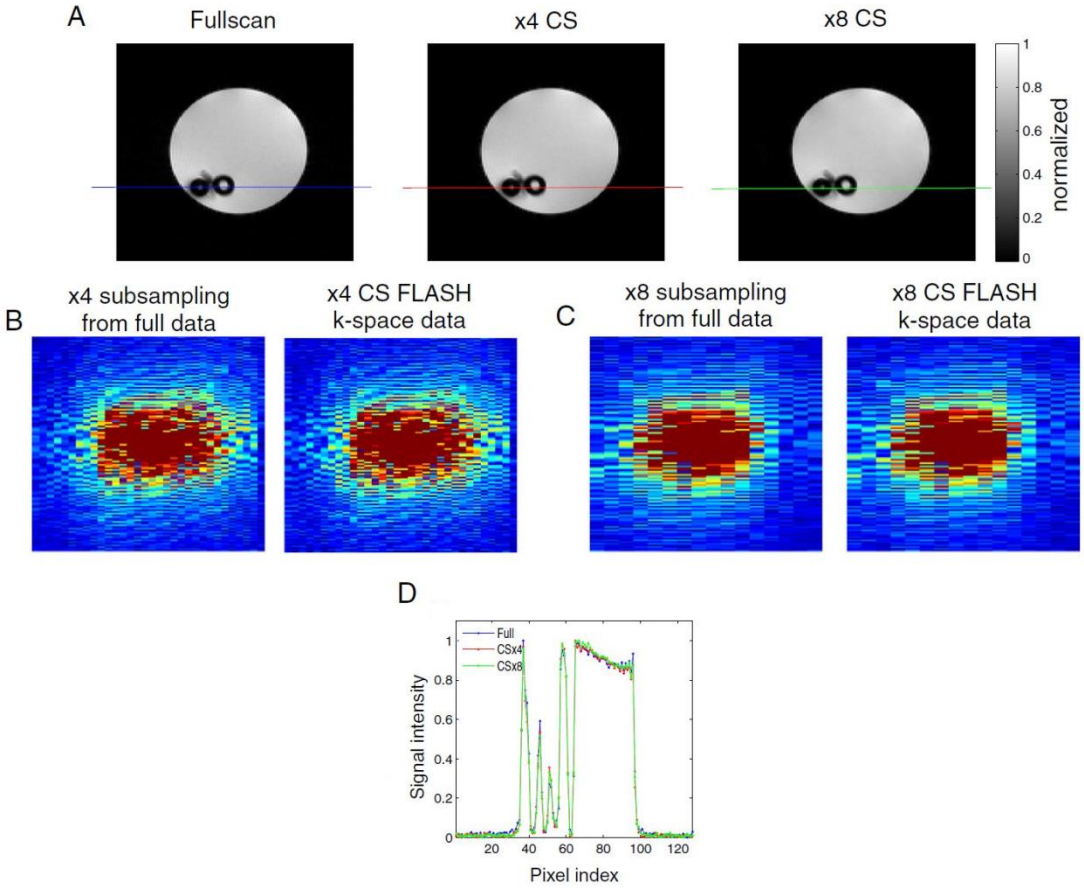

Figure 3.1.5 (A) The water phantom images from FLASH sequence and CS-FLASH sequence with the acceleration factors of 4 and 8. **(B-C)** *k*-space from CS-FLASH acquisitions and undersampled *k*-space from FLASH acquisition. **(D)** The signal intensity line profile across the sample.

In vivo tumor model application

First, DCE – MRI was performed on three different mice using conventional FLASH, CS-FLASH with the acceleration factors of 4 and 8 at fixed spatial resolution to test the improvement of temporal resolution. **Figure 3.1.6 (A)** represents the image and uptake curve with conventional FLASH sequence with the matrix size of 128×128 and the temporal resolution of 12.8s. **Figure 3.1.6 (B)** and **(C)** represent the image and uptake curve with the CS-FLASH sequence at the acceleration

factors of 4 and 8 with the temporal resolution as 3.2s, and 1.6s, respectively. The increase in the number of temporal points for the same acquisition time demonstrates that the increased temporal resolution.

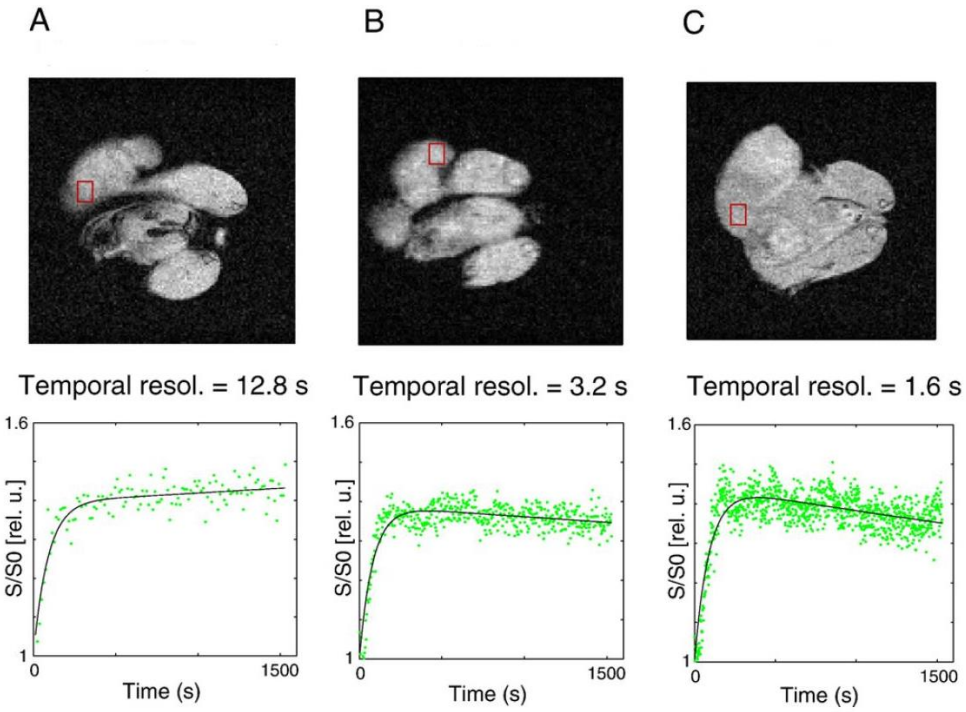

Figure 3.1.6 (A) MR image and uptake curve from FLASH with the matrix size of 128 × 128 and the temporal resolution of 12.8s. **(B-C)** CS reconstructed images and uptake curves at the acceleration factors of 4 and 8 with temporal resolutions of 3.2s and 1.6s, respectively.

Second, a longitudinal DCE – MRI study was performed to test the improvement of spatial resolution at fixed temporal resolution. Firstly, DCE – MRI experiment was performed with conventional FLASH with the matrix size of either 128×32 or 128×16. After 5 hours which are clearance time of CA, DCE – MRI experiment was repeated with CS-FLASH at the acceleration factors of 4 or 8. Ak_{ep} maps from three tumors were shown in **Figure 3.1.7**. High agreement of the heterogeneous Ak_{ep} distribution between conventional FLASH and CS-FLASH were observed and improved spatial resolution was also observed.

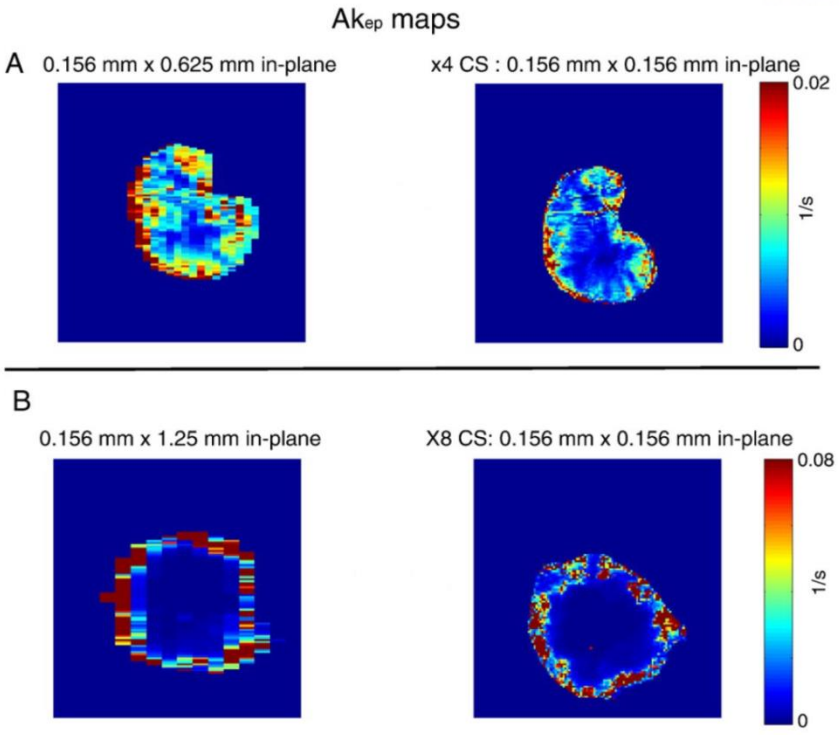

Figure 3.1.7 (A) Ak_{ep} maps from FLASH and CS-FLASH with the acceleration factor of 4. **(B)** Ak_{ep} maps from FLASH and CS-FLASH with the acceleration factor of 8.

3.1.4 Discussion and conclusions

We improved the spatial and temporal resolution for *in vivo* DCE – MRI by implementing CS-FLASH sequence. Temporal resolution improvement was shown by comparing conventional FLASH with CS-FLASH at fixed temporal resolution. And spatial resolution improvement was proved by acquiring longitudinal Ak_{ep} map. Better spatial resolution in CS-FLASH shows the potential to delineate the tumor region more accurately and characterize perfusion/permeability information more finely.

As the FLASH sequence is well accepted for the acquisition of DCE – MRI for *in vivo* studies, the improvement of spatial/temporal resolutions has a great potential to assist preclinical and clinical investigations of tumor microenvironment. Especially, improved temporal resolution can be helpful to the measurement of arterial input function (AIF), which is very challengeable to acquire due to its fast wash-out. In conclusion, this work offers a promising and straightforward process for improving the spatial/temporal resolution of DCE – MRI with CS algorithm and has potential to be applicable to many preclinical and clinical investigations with widely used FLASH acquisitions.

3.2 Temporal resolution increase of calibration-free DCE – MRI by CS-TSE

3.2.1 Introduction

DCE – MRI provides a quantitative diagnosis of microvascular changes [39-40]. Fast gradient-echo based T_1-weighted sequence, such as fast low-angle shot (FLASH) [41], is typically used with careful control of the administration dose of the gadolinium (Gd)-chelate contrast agent to neglect T_2^*-relaxation. On the other hand, the inversion of the signal enhancement to T_1 value from FLASH using a theoretical equation, often causes errors because of associated imperfections, such as flip angle heterogeneities and uncompensated transverse relaxations [42]. To reduce such limitation, the calibration approach can be used to pre-establish the calibration curve of signal enhancement *versus* the T_1 relationship with the phantoms [42-44] or the double gradient echo sequence [45] can acquire two different gradient echoes to compensate for the potential T_2^*-decay by fitting TE dependent signal decay. Additionally, quantitative approach with arterial input function (AIF) improves the reproducibility and reliability of DCE – MRI when the longitudinal investigation is performed or different acquisition parameters are employed [46-47]. For this reason, AIF measurement is preferable. However, AIF measurement in rodent model is challenging due to high heart rates up to 600 beats/min and the requirement of high spatial resolution [48]. Specifically, temporal resolution below a second is required to assess first-pass AIF acquisition considering their high heart rates [48].

An alternative method to overcome T_2^*-induced limitations of gradient echo based dynamic T_1-weighted acquisitions is to use a spin-echo based fast imaging sequence, i.e., turbo spin echo (TSE) [2]. With minimized T_2^* effect by replacing T_2^* with T_2, calibration-free T_1 inversion from signal enhancement using theoretical equation may be robustly applied for *in vivo* quantification of high Gd-concentration regions. At the same time, to match the demanding spatio-temporal resolution of DCE – MRI applications including AIF measurements with TSE acquisition, turbo factor is typically increased for the large *k*-space coverage of phase encodings for each echo train, which inevitably worsens slice coverage at short repetition time (TR) for T_1-weightings and further induces significant T_2 contributions.

Recently, compressed sensing (CS) demonstrated that only a small fraction of the samples is necessary with the assumption that signal is sparse [22-25]. The application of CS to DCE – MRI verified the benefit of accelerating sampling requirements for the perfusion measurements [28-30]. The application of CS to dynamic TSE acquisition has potential to improve the temporal resolution without increasing turbo factor, and thus maintaining necessary slice coverage at minimized TR

values for calibration-free DCE – MRI.

In this study, firstly, CS-optimized TSE (CS-TSE) was implemented by optimizing sparse sampling scheme from fully-sampled data, and applied to slice-selective DCE – MRI studies at the temporal resolution of 0.96s, with the number of slices of 4. Secondly, the feasibility of calibration-free quantification and the degree of enhancement were investigated with Gd-doped phantoms of varying concentrations from 0.1 to 6mM for FLASH, TSE, and CS-TSE acquisitions. Thirdly, kidney feeding AIF measurements at multiple administration doses of 0.1, 0.2, and 0.3mmol/kg were performed to demonstrate the benefit of CS-TSE in capturing first-pass AIF without compromising slice coverage, in comparison with conventional TSE. Direct comparisons between calibration-free and calibrated inversions of *in vivo* Gd-concentration were also conducted to demonstrate the feasibility of calibration-free inversion of CS-TSE signal. Finally, kidney perfusion heterogeneity between cortex and medulla regions was compared between FLASH and CS-TSE acquisitions to show the improved contrast enhancement and faithful reflection of *in vivo* Gd-concentration from CS-TSE acquisitions. Proposed CS-TSE acquisition with sub-second temporal resolution without slice coverage reduction provides calibration-free dynamic MR quantification of high Gd-concentration regions including kidney and AIF for a rodent model.

3.2.2 Materials and Methods

Animal, MR system and contrast agent

A total of 22 female C57BL/6 mice (17–22 g, 10 weeks of age) were used with approval from the Institutional Animal Care and Use Committee of Ulsan National Institute of Science and Technology. The contrast agent used was gadoterate meglumine (Gd-DOTA, DOTAREM; Guerbet, Paris, France). All experiments were performed on a horizontal 7T MRI system (Bruker BioSpin, Billerica, MA, Paravision 6, gradient strength up to 780 mT/m) with the bore size of 16 cm using a 40 mm volume coil.

Optimization of compressed sensing to dynamic TSE

For the DCE – MRI application of TSE acquisition, short TR (T_1 contrast increase) and minimized turbo factor (transverse relaxation reduction) is required with reasonable slice coverage. However, there is trade-off between the turbo factor and the number of slices because the maximum value of turbo factor × number of slices is limited at fixed TR. In other words, increasing turbo factor reduces the possible number of slices, and vice versa. To acquire reasonable number of slices for DCE – MRI application including AIF measurement, we set TR as 60ms, and the number of slices as 4, which fixed the turbo factor of 2 and the temporal resolution of 3.84s for 128 × 128 matrix. Resulting

temporal resolution is not enough to capture the fast first-pass AIF. If the turbo factor is increased by 8 to attain a sub-second temporal resolution, the number of slices would be reduced to 1, and the transverse relaxation effect would increase as well. These limitations of conventional TSE for the application of sub-second DCE – MRI led us improve the temporal resolution by applying CS without sacrificing the number of slices or increasing the turbo factor. The schematic pulse sequence diagram and acquisition parameters for CS-TSE was described in **Figure 3.2.1**.

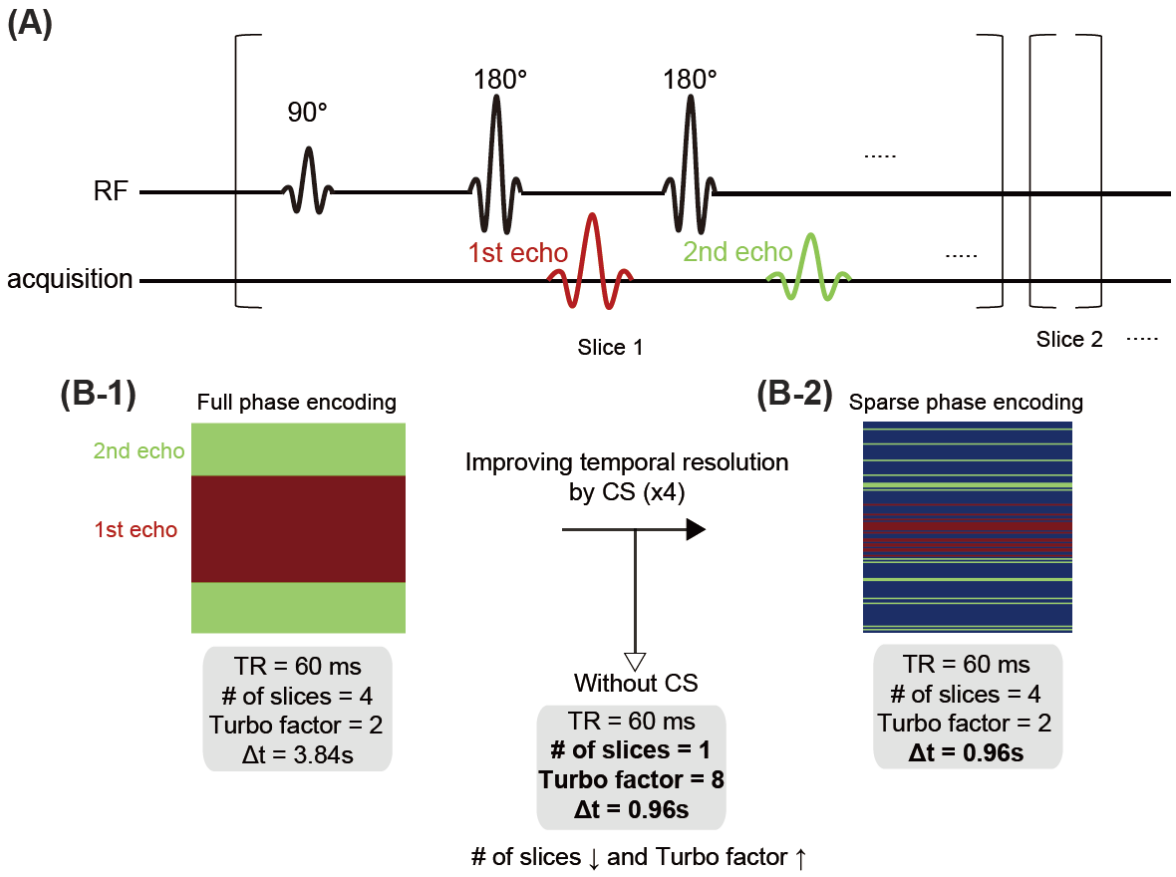

Figure 3.2.1 (A) Schematic diagram of TSE pulse sequence with turbo factor of 2. **(B-1)** Centric allocation of *k*-space in conventional TSE. **(B-2)** Centric allocation of *k*-space of CS-TSE with CS acceleration factor of 4.

Compressed sensing can be described as reconstructing the signal from under-sampled data by minimizing the l_1-norm of the signal over the sparse domain, which is an operation known as the compressive transform. This is achieved by solving the following constrained minimization problem,

$$minimize \ \|\Psi s\|_1 \qquad (3.2.1)$$

$$subject\ to \ \|Fs - k\|_2 < \varepsilon \qquad (3.2.2)$$

where s is the reconstructing image, ψ is a sparse transform operator such as wavelet or Fourier transformations. The acquired under-sampled k-space is k, F is the Fourier transformation operator, and ε is the constraint that controls the accuracy and the speed of reconstruction. The reconstruction was performed with the code developed in MATLAB (MathWorks, Natick, MA, USA) and two external packages: spgl v.1.7 [37] for solving the l_1-norm minimization problem and Wavelab v.7.01 [38] for applying the wavelet transformation using a personal computer with an Intel Core i7 2.60GHz central processing unit and 16GB of memory on the Windows 8.1 platform.

Optimizations were retrospectively performed using fully-sampled DCE – MRI data, especially focused on the kidney region. Fully-sampled DCE – MRI data were generated by modifying TSE sequence to obtain full k-space signals for each echo in the TSE acquisition. The parameters for fully-sampled DCE – MRI with TSE were as follows: TE/TR = 5.04/60 ms, turbo factor = 2, slice thickness = 1 mm, the number of slices = 4, the number of average (NA) = 1, matrix size = 128 × 128, spatial resolution = 352 × 352 μm^2, the number of repetitions (NR) = 128, temporal resolution = 7.68s, and total acquisition time = 16min 23s with the administration time of 2min after starting the acquisition. Note the doubling of the temporal resolution due to full k-space signals for each echo in the TSE acquisition.

To adjust CS acquisition/reconstruction parameters for the TSE, five variables were optimized; (1) acceleration factor for CS, (2) the variance of Gaussian weighting for generating sparse sampling scheme, (3) the portion of k-space center sampling, (4) the segmentation size for the temporal incoherence, and (5) the constraint for reconstruction (ε).

First, to find optimal random sparse sampling scheme to increase incoherence in k-space, the variance of Gaussian weighting and the portion of k-space center sampling were varied. The variance (α) of Gaussian weighting ($e^{-\alpha x}$) was varied from 1 to 20, which determined the degree of acquisition for high k-space values. The portion of k-space center sampling was varied by controlling the center keep fraction (f) from 0.1 to 0.6. The number of k-space center sampling of phase encodings was calculated by the number of phase encoding / CS acceleration factor × center keep fraction (f). Second, to determine the sufficient segmentation size along the temporal domain, a random sparse sampling scheme was varied for each time point for n times (segmentation size), and temporally varying sparse samplings were repeated for the following segmentations of the same sizes. The segmentation size (n) was varied from 16 to 128 with fixed α of 13, f of 0.1, and CS acceleration factor of 4. The optimization of the segmentation size was to avoid redundantly large phase encoding array, while maintaining the image quality. Third, the constraint (ε) for reconstruction which controls least squares difference between acquired data and reconstructed data was optimized by considering both computation time and reconstructed image quality, as the constraint is significantly related to the total computation time for reconstruction [49]. To find optimal constraint, the constraint (ε) was varied

from 10^{-2} to 10^{-5} after normalizing acquired *k*-space data with fixed α of 13, *f* of 0.1, CS acceleration factor of 4, and *n* of 32. Finally, the image quality study was conducted with CS acceleration factors of ×4, ×8, and ×16 with fixed α of 13, *f* of 0.1, and *n* of 32 to find optimal CS acceleration factor. For the quantitative comparison between fully-sampled image and CS reconstructed image, the concordance correlation coefficient (CCC) value was calculated as a metric of the quality of the reconstruction by the following equation [50],

$$CCC\ value = \frac{2\rho\sigma_{full}\sigma_{reconstructed}}{\sigma_{full}^2 + \sigma_{reconstructed}^2 + \left(\mu_{full} - \mu_{reconstructed}\right)^2} \quad (3.2.3)$$

where ρ, σ, μ are the correlation coefficient, mean, and standard deviation.

Calibration-free and calibrated inversions of the FLASH and CS-TSE signals in Gd-doped phantoms

A total of 7 phantoms of saline solution with Gd-DOTA in the range of 0.1 to 6 mM were used to show the feasibility of calibration-free quantification of corresponding T_1 values with CS-TSE signal. Reference T_1 values were pre-measured using an inversion-recovery spin echo sequence (IRSE) for all phantoms with the following parameters: TE/TR = 5.04/8500 ms, inversion time (TI) = 8.6 to 8000 ms (26). T_2 values were measured using MSME sequence with the following parameters: TR = 6000 ms, TE = 5.1 to 127.5 ms (25). The parameters for FLASH were as follows: TE/TR = 2.5/30 ms, and flip angle (FA) = 30° with RF spoiling. The parameters for TSE were as follows: TE/TR = 5.04/60 ms, and turbo factor = 2. The parameters for CS-TSE were as follows: TE/TR = 5.04/60 ms, turbo factor = 2, CS acceleration factor = 4. The matrix size = 128 × 128, spatial resolution = 352 × 352 μm^2, slice thickness = 1 mm, the number of slices = 4, and the number of repetitions = 32 were kept the same for all sequences. And temporal resolutions for FLASH, TSE, and CS-TSE were 3.84s, 3.84s, and 0.96s, respectively.

First of all, the signal enhancement for each phantom was normalized by dividing each signal intensity with that of 0.3 mM phantom to show the benefits of CS-TSE in sensitivity. Additionally, for the calibration inversion approach, the signal intensities from 7 phantoms (*S*) were divided by the reference phantom's signal intensities from 0.1mM (FLASH), and 0.5mM (TSE). Corresponding signal ratios ($S/S_{0.1mM}$ *and* $S/S_{0.5mM}$) were fitted with a bi-exponential function to generate calibration curves for FLASH and TSE acquisitions. For the calibration-free inversion approach, the signal intensity from FLASH was converted to the R_1 value by using the below equations [51],

$$R_1(t) = \frac{1}{TR} ln\left(\frac{S_0 \cdot \sin(FA) \cdot e^{-\frac{TE}{T_2^*}} - S(t) \cdot \cos(FA)}{S_0 \cdot \sin(FA) \cdot e^{-\frac{TE}{T_2^*}} - S(t)}\right) \quad (3.2.4)$$

$$S_0 = S_{ss}\frac{1-\cos(FA)\cdot e^{-\frac{TR}{T_{1,0}}}}{\left(1-e^{-\frac{TR}{T_{1,0}}}\right)\cdot\sin(FA)\cdot e^{-\frac{TE}{T_2^*}}} \quad (3.2.5)$$

where S_{ss} and $S(t)$ are pre- and post-injection signal intensities. The contribution of T_2^* was ignored by assuming that it is negligible at short TE. R_1 was converted to Gd-concentration as follows:

$$\frac{1}{T_1} = r_{1,Gd-DOTA} \times C_p \times (1 - H_{ct}) + \frac{1}{T_{1,0}} \quad (3.2.6)$$

where $r_{1,Gd-DOTA}$ is T_1 relaxivity of Gd-DOTA, and was calculated as 4.547 $s^{-1}mM^{-1}$ from IRSE measurements, C_p is the Gd-concentration in plasma, H_{ct} is hematocrit and was set as 0.45 based on literature value [52], and $T_{1,0}$ and T_1 are pre- and post-injection relaxation times, respectively.
In the case of CS-TSE acquisition, signal intensity was converted using the below equations [53],

$$S = S_0\frac{sin(FA)}{1+cos(FA)} \times \left[1 - (E_1 - cos(FA))\sqrt{\frac{1-E_2^2}{1-E_1^2E_2^2-2E_1(1-E_2^2)cos(FA)+(E_1^2-E_2^2)cos^2(FA)}}\right] e^{-\frac{TE}{T_2}} \quad (3.2.7)$$

$$\frac{1}{T_2} = r_{2,Gd-DOTA} \times C_p \times (1 - H_{ct}) + \frac{1}{T_{2,0}} \quad (3.2.8)$$

where E_1 is exp(-TR/T_1), E_2 is exp(-TR/T_2), $r_{2,Gd-DOTA}$ is T_2 relaxivity of Gd-DOTA, and was calculated as 5.359 $s^{-1}mM^{-1}$ from MSME measurements. $T_{2,0}$ and T_2 are pre- and post-injection relaxation times, respectively. For the inversion of CS-TSE signals to Gd-concentration, Eq. (3.2.6) and Eq. (3.2.8) were inserted in Eq. (3.2.7) and Gd-concentration was estimated.

AIF measurement among FLASH, TSE, and CS-TSE at multiple doses

For *in vivo* calibration approach, reference phantoms of 0.1, and 0.5mM for FLASH, and TSE, CS-TSE were attached near kidney region. When tissue signal is divided by reference signal from attached phantom, proton density difference between reference phantom and tissue needs to be considered as shown in the following equation,

$$\frac{S_{tissue}}{S_{ref}} = \frac{S_{0,tissue}}{S_{0,ref}} \times signal\ ratios\ (SR) \quad (3.2.9)$$

To compensate the proton density ratio ($S_{0,tissue}/S_{0,ref}$), the inverse of proton density ratio ($S_{0,ref}/S_{0,tissue}$) was multiplied to uncompensated signal intensity ratio ($S_{0,tissue}/S_{0,ref}$ × signal ratios (SR)) to acquire corresponding signal ratios (SR), so that calibration curve can be used.
Before DCE – MRI experiment, T_1, T_2, and proton density measurements were needed to convert

signal intensities to Gd-concentration. $T_{1,0}$ was measured by TSE with the following parameters: TE = 5.04 ms, TR = 110 to 5000 ms (13), turbo factor = 4, the measurement time = 8 mins. $T_{2,0}$ was measured by MSME sequence with the following parameters: TE = 5.1 to 127.5 ms (25), TR = 6000 ms, the measurement time = 12 mins 48s. Proton density was measured by TSE sequence with the following parameters: TE/TR = 5.04/9000 ms, the measurement time = 9mins 36s. After acquiring three parameters, DCE – MRI study was performed. In the case of FLASH, the imaging parameters were as follows: TE/TR = 2.5/30 ms, FA = 30° with RF spoiling, NR = 256, and temporal resolution = 3.84s. In the case of TSE, the imaging parameters were as follows: TE/TR = 5.04/60 ms, and turbo factor = 2, NR = 256, and temporal resolution = 3.84s. In the case of CS-TSE, the imaging parameters were as follows: TE/TR = 5.04/60 ms, and turbo factor = 2, CS acceleration factor = 4, NR = 1024, and temporal resolution = 0.96s. The matrix size = 128 × 128, spatial resolution = 352 × 352 μm^2, slice thickness = 1 mm, the number of slices = 4, and the total acquisition time = 16min 23s with the injection time of 2min after starting the acquisition were kept the same for all sequences.

Two different doses of Gd-DOTA were administered with FLASH at 0.1 mmol/kg (n = 2), 0.2 mmol/kg (n = 2), and three different doses of Gd-DOTA were administrated with TSE and CS-TSE at 0.1 mmol/kg (n = 3), 0.2 mmol/kg (n = 3), and 0.3 mmol/kg (n = 3) for the dose dependent peak AIF enhancement.

To minimize inflow effect in artery region, the imaging was performed in a sagittal view as shown in **Figure 3.2.5 (A)**. Time-to-peak (TTP) was calculated to extract the artery region by selecting minimum TTP regions and averaging highest top ten enhancement voxels.

3.2.3 Results

Sparse phase encoding scheme to dynamic TSE with compresses sensing

Firstly, to optimize random sparse sampling scheme for dynamic DCE – MRI applications, the variance of Gaussian weighting and the portion of *k*-space center sampling were varied. The variance (α) controls the width of Gaussian sampling distribution, and smaller α value includes more of high *k* values as shown in the inset of **Figure 3.2.2 (D)**. The center keep fraction (*f*) determines the portion of low *k* values and sparse sampling scheme with *f* value of 0.2 and 0.6 were shown in the inset of **Figure 3.2.2 (E)**. Corresponding CCC value was calculated by varying the variance (α) and the center keep fraction (*f*) as shown in **Figure 3.2.2 (D)**, and **(E)**, respectively. Stable and high CCC values were observed in the ranges of α between 4 and 13, and *f* between 0.1 and 0.4. The variance of 13 and center keep fraction of 0.1 were selected as optimal α, and *f*. Secondly, to determine the practical segmentation size (*n*) along temporal dimension for DCE – MRI, corresponding CCC values for different segmentation sizes from 16 to 128 were compared. For example, in the case of number of repetition (NR) of 256, and segmentation size (*n*) of 32, CS reconstruction with segmentation size of 32 were repeated 8 times separately. From the segmentation size of 32, CCC values showed saturating as shown in **Figure 3.2.2 (F)**. For this reason, the optimal segmentation size was decided by 32 as the minimum segmentation size without deteriorating the reconstruction quality. Thirdly, with optimized sparse sampling scheme with α of 13, *f* of 0.1, $n = 32$, and CS acceleration factor of 4, the constraint (ε) were optimized by varying it from 10^{-1} to 10^{-5}. From the constraint of 10^{-2}, CCC value was saturated, which means that there is no benefit to the reconstruction quality even tighter constraint as shown in **Figure 3.2.2 (G)**. Based on this behavior, optimized constraint was set as 10^{-2}. Finally, CS reconstructions were performed at three different CS acceleration factors of 4, 8, and 16 with optimized parameters determined above. The residual images from between fully-sampled and CS reconstructed images were shown in **Figure 3.2.2 (A)** and **(B)** for CS acceleration factors of 4 and 8, respectively. The degradation of the image quality for CS acceleration factor of 8 was observed comparing that for CS acceleration factor of 4. The corresponding CCC value plot was depicted in **Figure 3.2.2 (C)**, and acceptable CS acceleration factor was determined as 4 based on those CCC values.

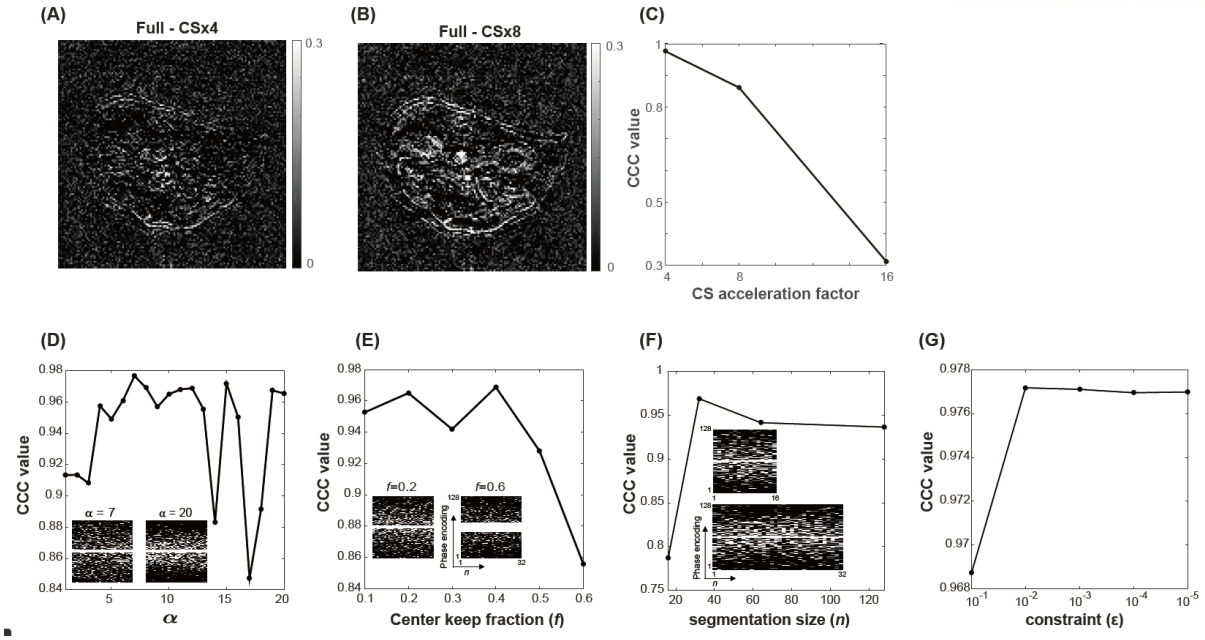

Figure 3.2.2 (A), (B) Residual images between fully-sampled image and CS reconstructed images with CS acceleration factors of 4 and 8. **(C) – (G)** CCC value plots corresponding to CS acceleration factors, Gaussian weighting variance (α), center keep fraction (*f*), segmentation size (*n*), and constraint (ε).

The feasibility from fully-sampled data and implementation of CS-TSE

The feasibility of CS to DCE – MRI should be validated not only for the static image quality but also for the temporal signal intensity variations in uptake curve. For this purpose, sparse sampling scheme with optimized parameters was applied to fully-sampled DCE – MRI data. **Figure 3.2.3 (A)** shows uptake curves from three different regions of interest (ROI) of kidney. Representative ROIs for artery, cortex, and medulla regions were depicted as red, green, and blue squares in **Figure 3.2.3 (A-1)**, respectively The good agreement between fully-sampled and CS reconstructed uptake curves for artery, cortex, and medulla regions was observed in **Figure 3.2.3 (A-2)**, **(A-3)**, and **(A-4)**, respectively. These results validate the potential for the application of CS for TSE acquisition to DCE – MRI application.

Next, based on these optimization steps, temporally varying sparse sampling schemes were implemented for Bruker PV6.0 platform and CS-TSE was tested with water phantom to prove its functionality. Fully-sampled and CS reconstructed images were shown in **Figure 3.2.3 (B-1)**, and **(B-2)**, respectively. Signal intensity line profiles across the water phantom as indicated by the blue and red lines in **Figure 3.2.3 (B-1)**, and **(B-2)** were compared and demonstrated that the signal intensity information is faithfully conserved in CS reconstructed image.

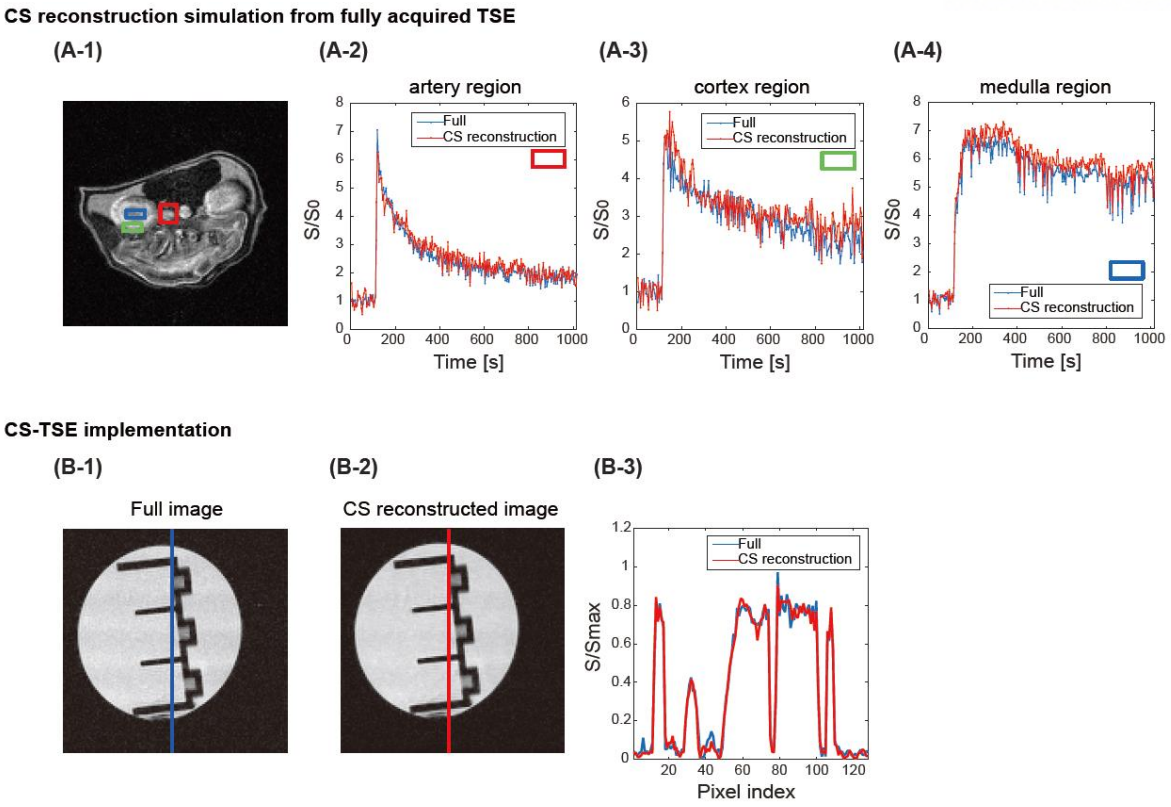

Figure 3.2.3 (A-1) DCE – MRI image of kidney region and ROIs of artery (red), cortex (green), and medulla (blue) regions. **(A-2) – (A-4)** Uptake curves from fully-sampled data (blue dot line) and CS reconstructed data (red dot line) for artery, cortex, and medulla regions, respectively. **(B-1), (B-2)** Images of water phantom from conventional TSE, and implemented CS-TSE. **(B-3)** Signal intensity profile from conventional TSE (blue) and CS-TSE (red).

Calibration-free and calibrated inversions of the FLASH and CS-TSE signals in Gd-doped phantoms

The signal intensity of each phantom was divided by that of the 0.3 mM phantom. Green circle, red star, and red circle lines represent signal enhancement of FLASH, TSE, and CS-TSE, respectively as shown in **Figure 3.2.4 (A)**. The level of enhancement from CS-TSE acquisitions was equivalent to those from TSE, ensuring that the application of CS does not introduce significant signal intensity artifacts. It is also important to note that the linearity between Gd-concentration *versus* signal enhancement from FLASH was maintained at up to 2 mM. On the other hand, the linearity from CS-TSE was steadily maintained at up to 6 mM. Moreover, the degree of signal enhancement was higher with CS-TSE than with FLASH.

The calibration curves, which relate the signal ratios of FLASH and CS-TSE to the corresponding T_1 values of different phantoms were shown in **Figure 3.2.4 (B-1)** and **(B-2)**, respectively. Theoretical signal ratio (black line) was calculated from Eq. (3.2.5) and (3.2.7) for FLASH and CS-TSE,

respectively. The measured signal ratio (blue line dots) was fitted with the bi-exponential function and labeled as the calibration curve (red line). In FLASH as shown in **Figure 3.2.4 (B-1)**, the measured ratios deviated from the theoretical ratios. On the contrary, the measured ratios correctly reproduced the corresponding theoretical ratios in CS-TSE acquisition, as shown in **Figure 3.2.4 (B-2)**. This result indicates that calibration is not needed to invert the signal ratios to corresponding T_1 values of different phantoms for CS-TSE over a wide range of Gd-concentrations.

The estimation of Gd-concentration from both calibration and calibration-free inversions was shown in **Figure 3.2.4 (C-1)** and **(C-2)** for FLASH and CS-TSE, respectively. The expected Gd-concentration was determined from T_1 values from IRSE by using Eq. (3.2.6). In FLASH acquisition, the calibration-free inversion method failed to extract the correct Gd-concentration starting even at relatively low Gd-concentration. The calibration approach improved the estimation, but it was limited to Gd-concentrations up to 2 mM. In CS-TSE acquisition, both the calibrated and calibration-free inversion agreed well with the expected Gd-concentration as shown in **Figure 3.2.4 (C-2)** at Gd-concentrations up to 6 mM.

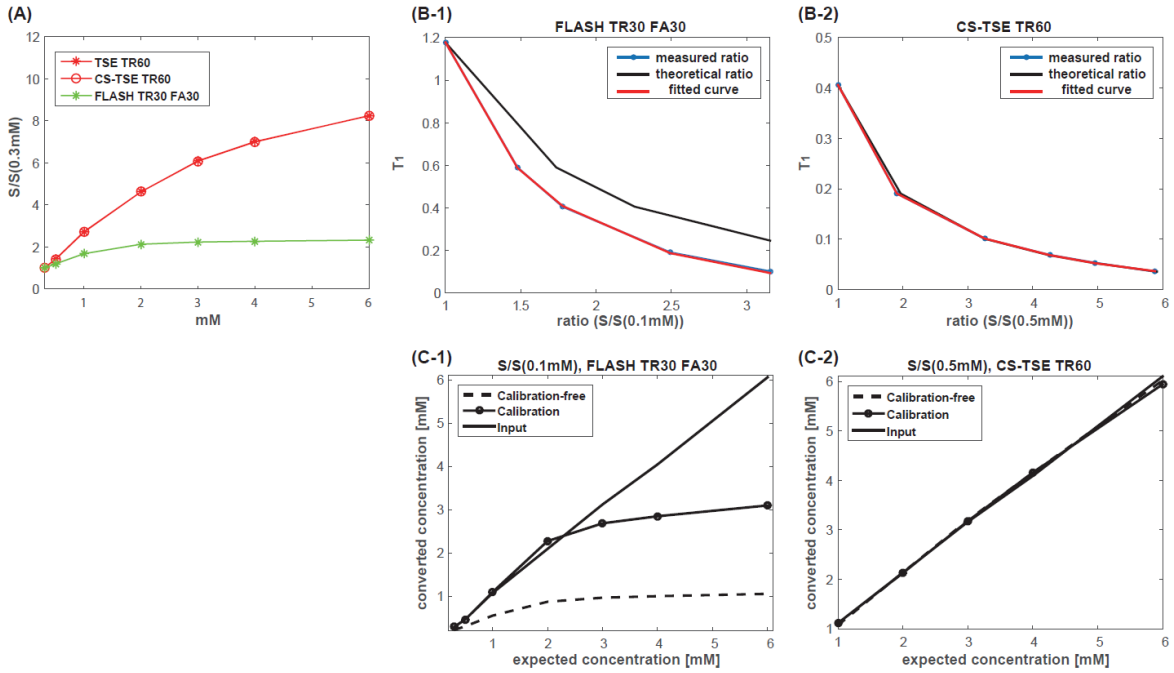

Figure 3.2.4 (A) Signal enhancement (S/S(0.3mM)) plots for FLASH (green star line), TSE (red star line), and CS-TSE (red circle line). **(B-1), (B-2)** Signal ratios versus T_1 curves for calibration with FLASH, and CS-TSE, respectively. Blue dot line, black line, and red line were from measurement by experiment, calculation by theoretical equations, and fitted by bi-exponential model. **(C-1), (C-2)** Concentration from IRSE versus that from calibration or calibration-free approaches for FLASH and

CS-TSE, respectively.

AIF measurement among FLASH, TSE, and CS-TSE at multiple doses

For *in vivo* kidney applications, the sagittal image after 10s of the Gd-DOTA administration, and the reference phantom for the signal calibration attached in left side of the body was shown in **Figure 3.2.5 (A)**. TTP map was shown in **Figure 3.2.5 (B)** and artery region was determined as white arrow region which has minimum TTP value area due to fast uptake.

To show the importance of sub-second temporal resolution to measure AIF first-pass peak, CS-TSE acquired AIF (red dots) at the administration dose of 0.1mmol/kg were shown at the temporal resolution of 0.96s and overlapped with of blue dots at the temporal resolution of 3.84s, which were obtained by under-sampling CS-TSE acquired AIF as shown in **Figure 3.2.5 (C)**. Temporal resolution degraded blue dot line tended to miss the AIF first-pass peak, which would cause the lower peak concentration. To further investigate this behavior at multiple cases with varying administration dose, AIF peak enhancements for FLASH, TSE, and CS-TSE were plotted on **Figure 3.2.5 (D)** as triangle, star, and circle shapes, respectively. Mean AIF peak enhancements for FLASH, TSE, and CS-TSE were marked as horizontal solid lines with triangle, star and circle, and administration doses at 0.1 (blue), 0.2 (green), and 0.3 (red) mmol/kg, respectively. Linear correlation between AIF peak enhancement and administration dose was apparent in TSE, and CS-TSE, but that in FLASH did not follow increasing dose, likely from T_2* effect. For example, the AIF peak enhancement with CS-TSE was 1.1439 and 2.1258 times higher than those with TSE and FLASH acquisitions, respectively at the administration dose of 0.1mmol/kg. Higher AIF peak enhancement in CS-TSE compared to TSE is likely from the sub-second temporal resolution as it would improve the robust acquisition of fast AIF first-pass peak.

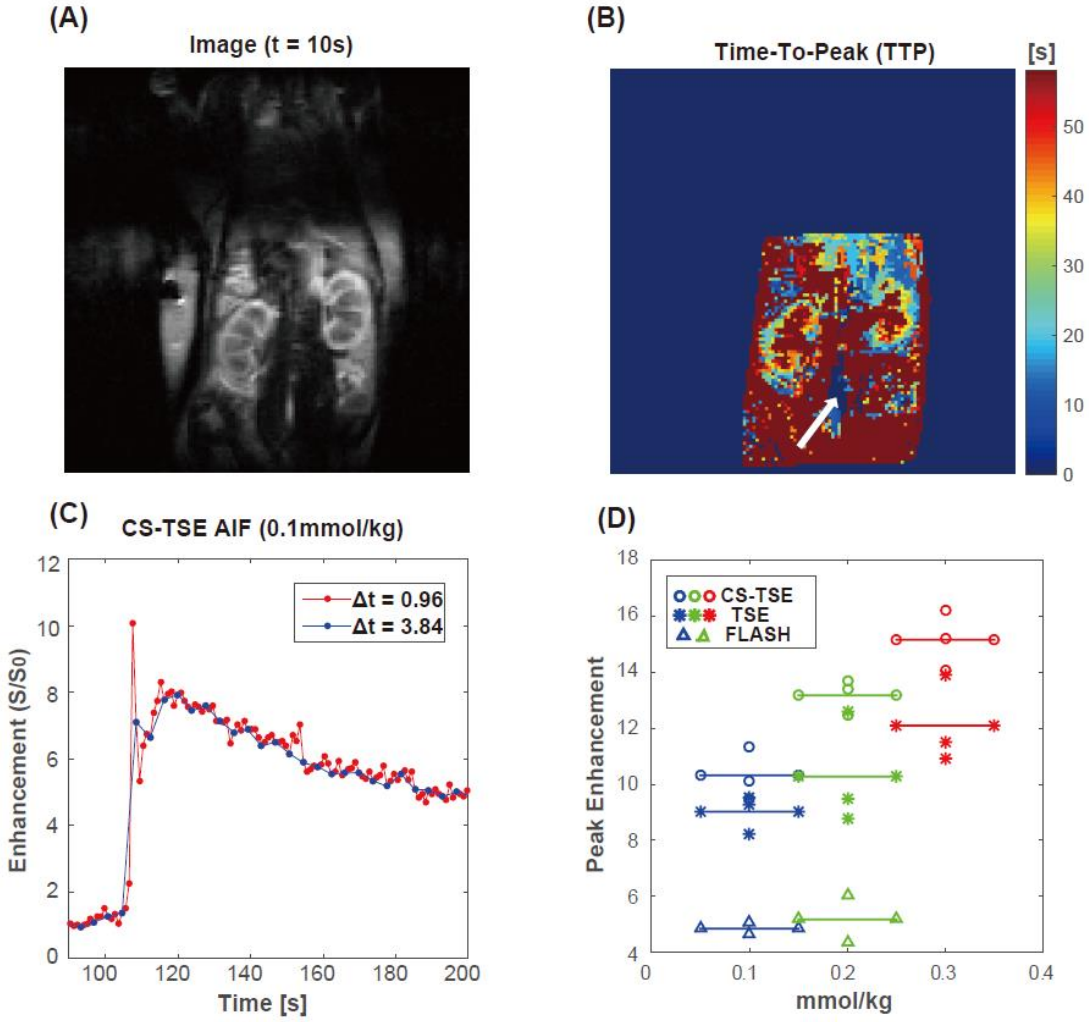

Figure 3.2.5 (A) Sagittal image after 10s of the administration of contrast agent. **(B)** Time-to-peak map. White arrow is minimum TTP corresponding to artery region. **(C)** AIF uptake curve from CS-TSE with temporal resolution of 0.96s (red dot line), under-sampled AIF with temporal resolution of 3.84s (blue dot line). **(D)** Relation between administration dose and peak enhancement of peak AIF for FLASH (triangle), TSE (star), and CS-TSE (circle). Horizontal lines are mean peak AIF enhancement.

Calibration-free and calibrated inversions of CS-TSE signals in AIF

To demonstrate the feasibility of calibration-free *in vivo* Gd quantification in AIF, below procedures were conducted and results were shown. To compensate the proton density ratio ($S_{0,tissue}/S_{0,ref}$) for *in vivo* calibration, the inverse of proton density ratio ($S_{0,ref}/S_{0,tissue}$) was averaged with 9 mice for CS-TSE and set to 1.1. Pre-injection $T_{1,0}$ and $T_{2,0}$ values were also measured to convert signal intensity to Gd-concentration with 9 mice for CS-TSE and averaged to 1.74s, and 1.00s,

respectively. Next, the estimation of AIF Gd-concentration at the administration dose of 0.1 mmol/kg from CS-TSE was compared between calibration-free (blue) and calibration (red) approaches as overlapped in **Figure 3.2.6 (A)**. There was no difference between calibration-free and calibration approaches, which shows the feasibility of calibration-free *in vivo* Gd-quantification. Estimated peak AIF Gd-concentrations from calibrated and calibration-free inversions were compared at three different administration doses as shown in **Figure 3.2.6 (B)** with apparent linear correlation (scatter plot slope = 0.7800, r^2 = 0.8014).

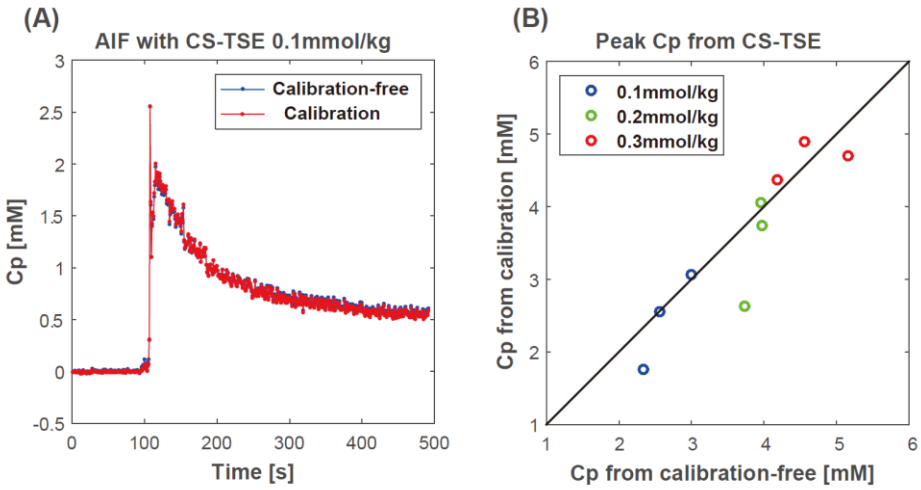

Figure 3.2.6 (A) AIF uptake curve with the dose of 0.1mmol/kg from calibration (red) and calibration-free (blue) approaches. **(B)** Scatter plot of AIF peak concentration between calibration and calibration-free approaches with varying administration dose from 0.1 to 0.3 mmol/kg.

Enhancing of kidney perfusion heterogeneity with CS-TSE

Contrast enhancement maps for FLASH and CS-TSE were shown in **Figure 3.2.7 (A)** and **(B)**, respectively. Black and white arrows correspond to medulla and cortex regions in kidney, respectively. In the case of FLASH, non-visible difference was observed, but visible difference in the signal uptake was shown in the case of CS-TSE. Uptake curves of cortex and medulla regions for FLASH and CS-TSE were plotted in **Figure 3.2.7 (C)**. Higher sensitivity in the enhancement was observed in CS-TSE compared to FLASH in agreement with previous phantom experiments, and the higher difference in peak concentrations between cortex and medulla regions were distinct with CS-TSE, reflecting higher Gd-concentration in kidney medulla. The kidney perfusion heterogeneity between cortex and medulla regions can be clearly differentiated with CS-TSE acquisition from improved contrast enhancement and faithful reflection of *in vivo* Gd-concentration.

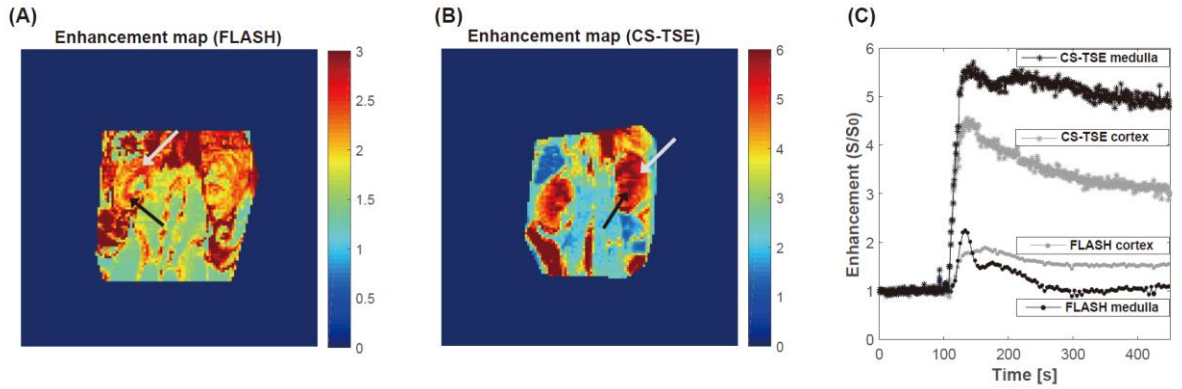

Figure 3.2.7 (A), (B) Enhancement map of FLASH and CS-TSE, respectively. **(C)** Uptake curves of cortex (gray) and medulla (black) regions for FLASH (dot line) and CS-TSE (star line)

3.2.4 Discussion and conclusions

In this work, the benefit of CS-TSE acquisition for DCE – MRI applications can be characterized with (1) calibration-free estimation of Gd-concentration, (2) increased temporal resolution without compromising slice coverage, and (3) improved contrast enhancements. The saturation of linearity between signal enhancement and Gd-concentration limits dynamic FLASH T_1 quantification. On the other hand, the signal enhancement from CS-TSE shows an increasing trend without apparent signal enhancement saturation up to 6 mM. Moreover, signal enhancement from CS-TSE acquisition for AIF with increasing administration dose showed linear relationship with administration dose. This dose-independency in AIF would be beneficial as the concentration gradient between the arterial and tissue signal would not further hamper accurate pharmacokinetic analysis, leading to potentially more accurate MR perfusion quantification.

To improve contrast enhancement of perfusion measurements from DCE – MRI, many efforts are focused in synthesizing new contrast agent with improved relaxation characteristics. As an alternative way in overcoming these issues, CS-TSE is promising acquisition method with significantly improved contrast enhancement with comparable acquisition parameters with FLASH, utilizing conventional contrast agent. Improvement in spatio-temporal resolution with CS-TSE will also benefit accurate determination of AIF in the small and rapid varying region as well.

Several limitations and future works of current study must be considered as follows. First, the possibility of inaccurate measurements of $T_{1,0}$, $T_{2,0}$, and proton density would give rise to errors in the quantification of Gd-concentration with calibration-free approach. Accurate measurements of T_1, T_2, and proton density are tricky because acquisition time is limited to *in vivo* application. Second, avoiding inflow effects are still challengeable even though the acquisition is performed in a sagittal view due to the arbitrary orientation of artery. One way to minimize inflow effect is to scan during diastole to minimize velocity, but it is hard to apply in small animal due to its fast heart rate. Future studies should explore the application of CS to 3D TSE acquisition to avoid inflow effect.

In conclusion, the present work validates the feasibility of CS-TSE for the application to calibration-free DCE – MRI for sub-second acquisition without reducing the number of slices. And distinguishability in kidney region also was shown, which reflects the accuracy in Gd-concentration without transverse artifact.

3.3 Improved contrast enhancement using ultrafast 3D spin-echo acquisition with compressed sensing assisted MMME

3.3.1 Introduction

3D acquisitions in MRI provides thin contiguous slices without cross-talks and unambiguous spatially specific positive contrast for *in vivo* applications with easier manipulation of resolution and signal to noise ratio (SNR) [54-61]. On the other hand, acquiring 3D images causes prolonged scan times from multiple repetitions due to the increased number of phase encodings for 3D *k*-space coverage [62]. To acquire 3D images in a reasonable scan time, ultrafast gradient echo acquisitions such as Echo Planar Imaging (EPI) or fast low angle shot (FLASH) are widely used for 3D T_1-weighted acquisitions. However, gradient echo based images are well known to be sensitive to susceptibility artifact from magnetic field inhomogeneities [63-64]. Susceptibility artifact results in inevitable T_2^* effect of contrast agent, which compromises the signal contrast enhancement and limits MR acquisition parameters and administration doses for contrast enhanced (CE) MRI [65-66]. For this reason, there has been developing the novel positive contrast agent able to increase the *in vivo* r_1/r_2^* ratio to minimize susceptibility artifact while maximizing positive contrast enhancement [67-70].
Previously,
rapid spin echo acquisition called rapid acquisition with relaxation enhancement (RARE) is used to reduce susceptibility artifact [71]. On the other hand, repeated RF pulses cause high RF power deposition which is more severe in repetitive 3D acquisition, especially as the magnetic field strength increases.
To increase the ratio of the number of echoes per RF pulse, many techniques have been developed by splitting the echoes from the multiple coherence pathways [72-81]. Especially, the multiple modulation multiple echo (MMME) sequence can maximize the number of echoes as 57 with only 5 RF pulses within 30~50ms, which shows the potential to reduce necessary repetitions of RF irradiations. Although the number of echoes can be exponentially increased as the number of RF pulses are increased in theory, the later echoes have lower SNR due to the signal decay by diffusion [3]. These lower SNR echoes deteriorate image quality and limit the methodological efficiency to fill the entire 3D *k*-space coverage of high resolution images for conventional MMME acquisitions.
Recently, compressed sensing (CS) was established and proved that only a small fraction of the samplings is sufficient to reconstruct sparse signals with compressive transformations such as Fourier or wavelet. By using CS theory, sampling requirement can be reduced, which provides the possibility to exclude lower SNR echoes without increasing repetitions to fill *k*-space. In other words, CS-assisted sampling allows the allocation of high SNR echoes to the center of *k*-space more efficiently.

In this work, we developed a new ultrafast 3D T_1-weighted imaging method with compressed sensing (CS) assisted multiple modulation multiple echo (MMME) sequence to maximize the positive contrast enhancement of 3D CE-MRI using Gd-DOTA. MMME is spin echo based acquisition method which can reduce susceptibility artifact and maximizes the ratio of the number of echoes per RF pulse, minimizing RF power deposition.

A multiplicative acceleration factor from multiple spin echoes (×32) by MMME and CS factor (×4, ×8) was studied for ultrafast 3D T_1-weighted images in susceptibility/relaxivity phantom, fruits, and *in vivo* animals. First, reduced susceptibility artifact with MMME sequence compared to conventional EPI acquisitions with the glass water phantom was conducted. Second, the proton density images with minimized T_2^* and diffusion weightings in MMME sequence was verified using the phantom which consisted of water, oil, and Gd-doped water at long repetition time (TR) and compared to RARE sequence with same multiple echo factor of 32. Third, the image quality was tested by varying the multiple echo factor in MMME called MMME factor, echo times (TE), and CS acceleration factors for multiple phantoms with fine morphology and *in vivo* animals. Finally, 3D CS assisted MMME sequence was implemented to show the improved contrast enhancement by the administration of Gd-DOTA at doses of 0.1, and 0.3 mmol/kg for multiple TR in rats. Contrast enhancement with CS-MMME was compared with corresponding conventional FLASH in kidney region which is sensitive to T_2^* effect due to its high dose compared to other tissue.

This work demonstrated the feasibility of CS-MMME with acceleration factors to achieve up to ×128 ~ ×256 in the number of repetitions required for 3D T_1-weighted spin echo acquisition, with in-plane resolution of ~200μm. Susceptibility artifact, unwanted T_2^* weighting, and RF power deposition can be minimized at the acquisition speed similar to corresponding EPI sequence with 3D coverage capabilities.

3.3.2 Materials and Methods

Scanner and animal approval

All experiments were performed on 4.7 T MRI scanner (Bruker BioSpin, Billerica, MA) using 72mm volume coil and gradient strength up to 38G/cm. Experiments using animal were performed with protocols approved by the Institutional Animal Care and Use Committee of the Korea Basic Science Institute.

MMME sequence and amplitude and phase correction

The diagram of the MMME sequence was shown in **Figure 3.3.1 (A)**. Five RF pulses with flip angles as [54°-71°-71°-71°-110°] were used to reduce the echo amplitude variation [3]. The delay between the first and the second pulse depicted as τ_1 was determined by considering the digitization time and the size of the matrix. And τ_2, τ_3, and τ_4 were set to $3\tau_1$, $9\tau_1$, and $17\tau_1$ to acquire separated echoes.

The MMME sequence is composed of a few RF pulses, which separates the echoes from independent coherence pathway [3]. The number of echoes is calculated as $(3^{N-1}-1)/2$ after N RF pulses. Following this equation, the number of echoes is exponentially increased when the number of RF pulses is increased. On the other hand, diffusion in the presence of the gradient attenuates the amplitude of echoes, causing lower SNR images when the later echoes were included. Moreover, variations in amplitude and phase for each echo from their different coherent pathways [3], which results in severe image artifacts without proper correction steps before Fourier reconstructions has to be considered as well.

For the amplitude correction, the amplitude ratio w_i of the ith echo is calculated as $w_i = A_m/A_i$, where A_i is the maximum amplitude in each echo and A_m is the largest amplitude for all echoes from the reference echoes without phase encoding gradients. After acquiring the amplitude ratio, each echo is multiplied by it. For the phase correction, the echoes from the reference echoes are Fourier transformed in the readout direction, and the phase of each echo is calculated. Acquired phases are subtracted from the phase of each echo and phase of each echo is corrected with respect to reference phase.

CS scheme for MMME

Undersampling scheme for implementing CS in the MMME sequence was generated by following Gaussian random sampling. The center region of *k*-space was always sampled to ensure SNR of image and the remaining region was sampled following Gaussian random weighting. This strategy guarantees low *k*-space region which ensures good SNR while covering enough high *k*-space

region to obtain detailed information of the images. Phase and slice encodings were undersampled following the centered Gaussian shaped scheme with the acceleration factors of 4, 8 and 16 because the readout direction can be fully sample at no costs. The example of undersampling scheme was shown in **Figure 3.3.1 (B)**. And **Figure 3.3.1 (C)** shows workflow from acquisition to reconstruction of 3D CS-MMME sequence. For example, a 3D image with the matrix size of 128×128×128 was selected, and 32 echoes from MMME and the acceleration factor of 8 from CS were applied. Therefore, undersampled scheme with the size as 128×128/8 was generated and ordered by calculating total gradient strength ($G_y^2 + G_z^2$), and allocated to 32 echoes from MMME sequence. In this case, only 64 repetitions were required to cover 3D *k*-space with total acceleration factor of 256 (32×8).

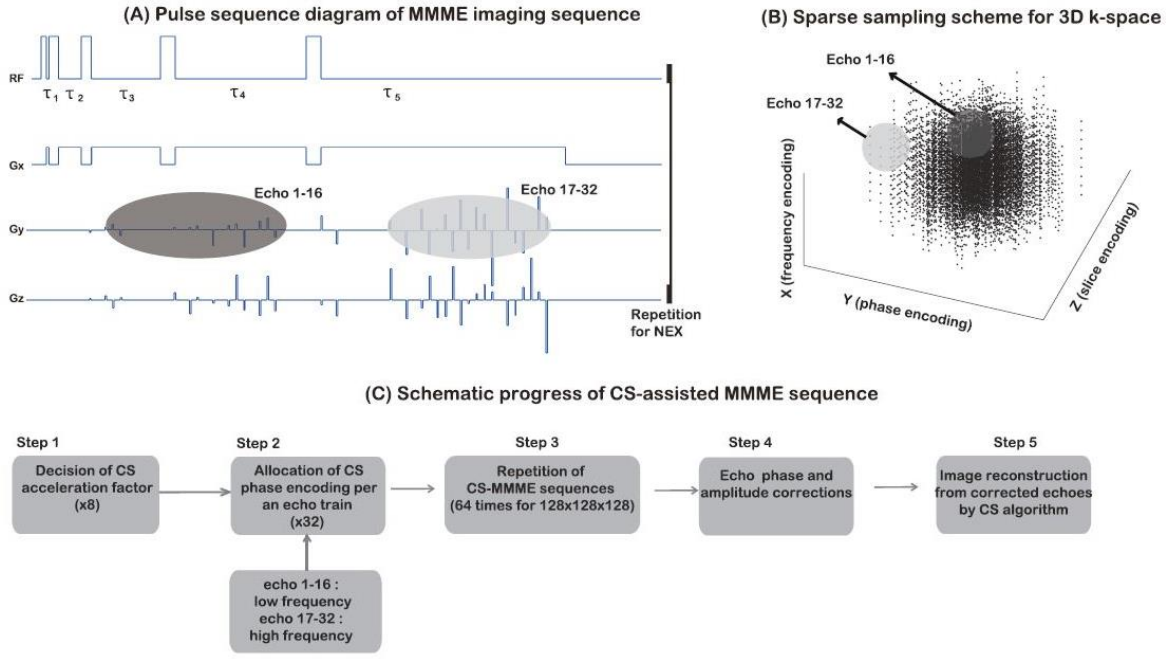

Figure 3.3.1 (A) Pulse sequence diagram. **(B)** Phase encoding scheme. **(C)** Workflow of CS-MMME sequence. Readout gradient is turned off during the RF pulses. The reference echoes are acquired by turning only on the readout gradient.

MR parameters for phantom and in vivo experiments with CS-MMME

First, MMME sequence with MMME factor of 32 was compared to conventional gradient echo and spin echo based EPI with glass water phantom to show the benefit of MMME for susceptibility artifact. MR parameters for EPI were following: TR = 3s, FOV = 2.59×2.59cm^2, resolution = 405×405μm^2, TE = 15ms. Second, RARE image with echo train length as 32 and MMME image with MMME factor as 32 were compared with the relaxivity/diffusion phantom consisted with water, oil, and Gd-doped water. And MR parameters for RARE were following: TR = 5s, FOV = 5×5cm^2, resolution = 195×195μm^2, effective TE = 165ms. MR parameters for MMME were following: the matrix size = 256×256×64, resolution = 203×203×813μm^3, dwell time = 5μs, phase/slice encoding gradient on time = 300μs, and τ_1 = 800μs. Third, fruits such as a tangerine and a kiwi were selected for optimizing the echo time, MMME factor, and the acceleration factor for CS-MMME due to its fine morphology. MR parameters for CS-MMME were following: TR = 3s, FOV = 5.22×5.22×5.22cm^3, the matrix size = 128×128×128 (64) and 256×256×64, dwell time = 5μs, phase/slice encoding gradient on time = 150 and 300μs, and τ_1 = 800 and 500μs. Fourth, *in vivo* proton density imaging was conducted. MR parameters for CS-MMME were following: TR = 3s, FOV = 5.22×5.22×5.22cm^3, the matrix size = 256×256×64 and 128×128×64, dwell time = 5μs, phase/slice encoding gradient on time = 300, and 150μs, τ_1 = 500μs, and the acceleration factors = 4,8, and 16. Finally, CS-MMME was compared to FLASH sequence to demonstrate the benefit of CS-MMME in terms of CE-MRI by the administration of Gd-DOTA at multiple TR and doses as 0.1, and 0.3mmol/kg. MR parameters for CS-MMME were following: TR = 45, 100, 250ms, FOV = 7.50×7.50×12.8cm^3, the matrix size = 256×256×64, dwell time = 5μs, phase/slice encoding gradient on time = 300μs, τ_1 = 500μs, and the acceleration factor = 8. MR parameters for FLASH were following: TR = 10, 40, 160, and 250ms, TE = 3ms, FOV = 0.2~2.4×8×8cm^3, the matrix size = 1~12×128×128. Contrast enhancement in kidney region was compared to each other.

3.3.3 Results

Minimal susceptibility artifact and T_2^* weighting with MMME

Spin echo based and gradient echo based EPI images for the glass water phantom were shown in **Figure 3.3.2 (A-2)** and **(A-3)**, respectively. Severe susceptibility artifact was shown in the EPI sequence. On the other hand, the image from MMME sequence showed less susceptibility artifact by taking advantage of spin echo as shown in **Figure 3.3.2 (A-1)**.

The RARE image for the relaxavity/diffusion phantom was shown in **Figure 3.3.2 (B-2)** with echo train length (ETL) of 32 and effective TE of 165ms. Gd-doped phantom showed smallest signal intensity due to its shortest T_2 relaxation time. However, MMME image with MMME factor of 32 showed similar signal intensities from three different samples. From this result, we can observe that MMME provides accurate proton density image insensitive to T_2 and diffusion by the echo amplitude correction step.

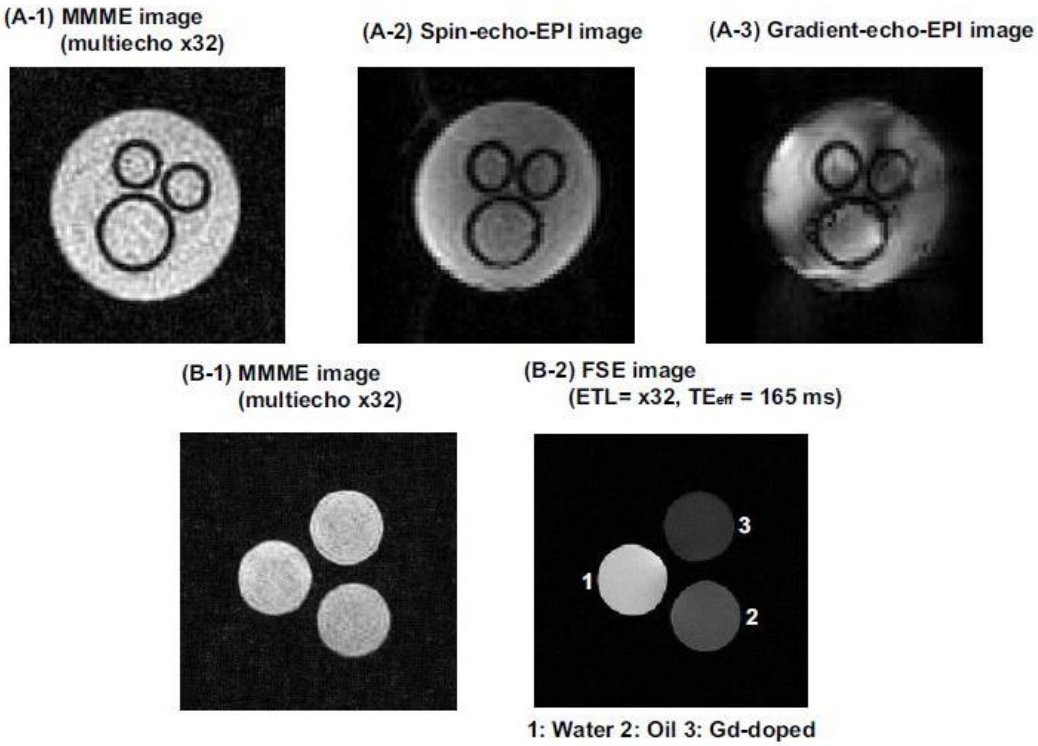

Figure 3.3.2 (A-1), (A-2), and **(A-3)** are the images of glass water phantom from MMME, spin echo EPI, and gradient echo EPI, respectively. **(B-1)** and **(B-2)** are the images of relaxivity/diffusion phantom from MMME and RARE with ETL as 32 and MMME factor as 32, respectively.

Optimization of the acceleration factor, MMME factor, and echo time for CS-MMME

First, the acceleration factor was studied by comparing the image quality between fully sampled image with MMME and CS-MMME image with the acceleration factors of 4 and 8 for a tangerine. The fully sampled image with MMME was acquired as the reference images for comparing it with CS-MMME images with MMME factors of 16 and 32. **Figure 3.3.3 (A-1)** and **(B-1)** showed sliced axial image from 3D image from MMME sequence with MMME factors of 16 and 32, respectively. CS-MMME images with the acceleration factor of 4 (**Figure 3.3.3 (A-2)** and **(B-2)**) and with the acceleration factor of 8 (**Figure 3.3.3 (A-3)** and **(B-3)**) were shown. The image quality from CS-MMME was morphologically consistent with that from fully sampled MMME with high correlation concordance coefficient (CCC) value above 0.92. On the other hand, the blurring effect on the boundary region of the tangerine was observed as the acceleration factor was increased. Second, the MMME factor was studied. For example, smaller MMME factor improves the image quality by discarding poor echoes, but it increases the requirement of the number of repetitions to fill 3D *k*-space. To verify the effect of MMME factor for the image quality, the acceleration factor was fixed and MMME factor was varied. CS-MMME image with MMME factor of 16 showed less background noise than that with MMME factor of 32. Images with MMME factor of 16 at the acceleration factors of 4 and 8 were shown in **Figure 3.3.3 (A-2)** and **(A-3)**. And images with MMME factor of 32 at the acceleration factors of 4 and 8 were shown in **Figure 3.3.3 (B-2)** and **(B-3)**. CCC values from the images with acceleration factors of 4 and 8 with fully sampled MMME image with MMME factor of 16 were 0.9909 and 0.9879, respectively. And CCC values from the images with acceleration factors of 4 and 8 with fully sampled MMME image with MMME factor of 32 were 0.9566 and 0.9233, respectively, showing lower image quality compared to that with MMME factor of 16. Finally, the effect of echo time depicted as τ_1 was studied, which determines the speed of scan time and the signal intensity of echoes. For example, the longer echo time decreases the SNR of each echo due to diffusion and T_2 weighting. Shortest echo time can increase not only SNR of each echo but also the speed of acquisition. On the other hand, the required dwell time and matrix size from FOV limit the echo time. Considering these limitations, echo times as 500 and 800μs were selected and compared the image quality with a kiwi sample as shown in **Figure 3.3.3 (C)**. The image quality of tangerine was not significantly different in terms of MMME echo time. High resolution image with the matrix size of 256×256×64 with the acceleration factor of 8 was shown in **Figure 3.3.3 (C-1)**. And the image with echo time of 800μs, the matrix size of 128×128×64, and the acceleration factor of 4 was shown in **Figure 3.3.3 (C-2)**. The seeds in kiwi were poorly observed in the lower resolution image compared to high resolution image. And the image with echo time of 500μs, the matrix size of 128×128×64, and the acceleration factor of 4 was shown in **Figure 3.3.3 (C-3)**. Shortened echo time with the same resolution and the acceleration factor showed less blurring in seeds as shown in **Figure**

3.3.3 (C-3) compared to the image in **Figure 3.3.3 (C-2)**.

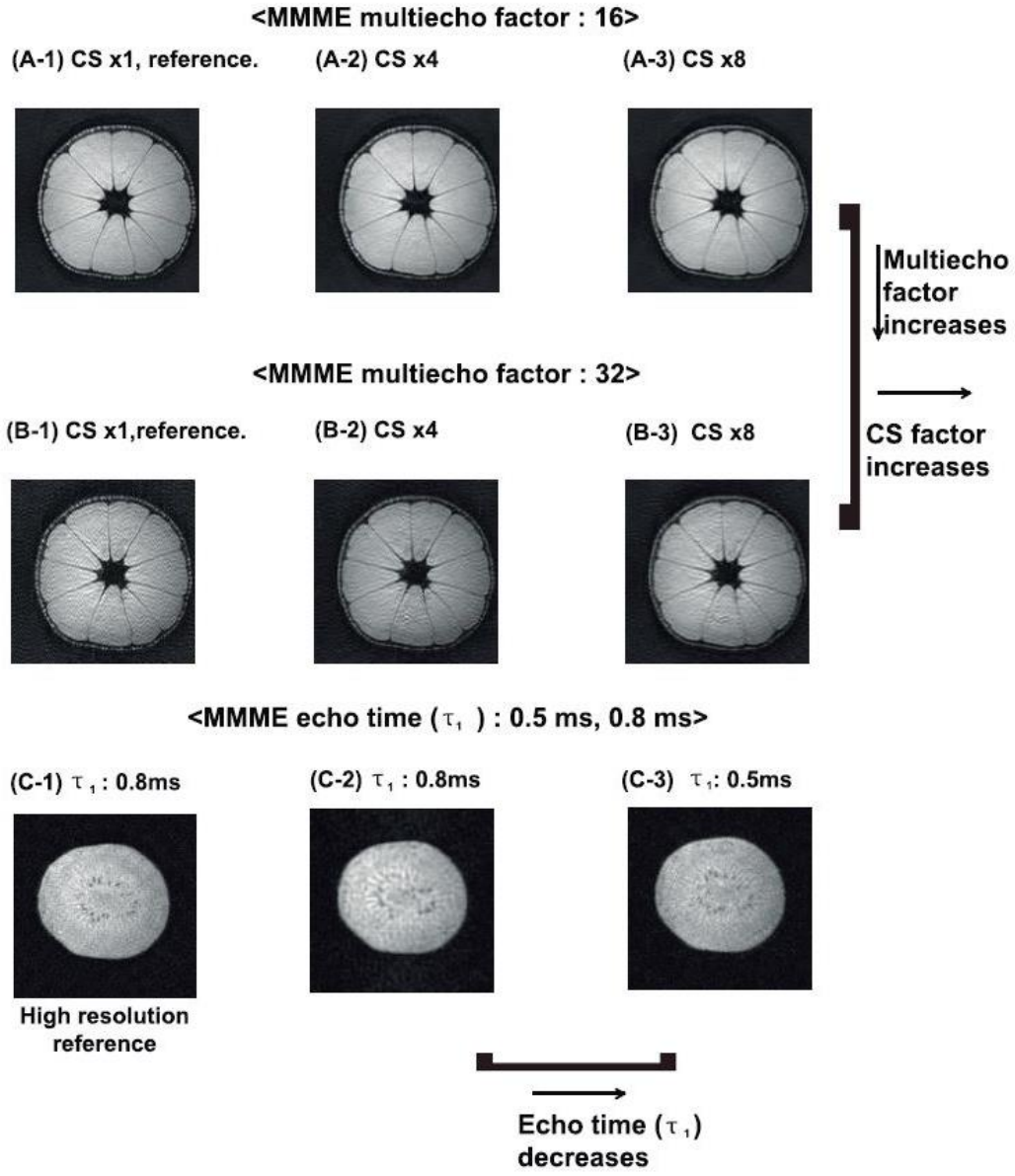

Figure 3.3.3 Images of a tangerine with MMME factor of 16 **(A)** and that of 32 **(B)**. The MMME images by fully sampled MMME as references **(A-1)** and **(B-1)**. **(A-2)** and **(A-3)** are CS-MMME images with the acceleration factors of 4 and 8 with MMME factor of 16. **(B-2)** and **(B-3)** are CS-MMME images with the acceleration factors of 4 and 8 with MMME factor of 32. All tangerine images were scanned with the matrix size of 128×128×128, and echo time of 800μs. **(C-1)** is the high resolution image with echo time of 800μs, the matrix size of 256×256×64, and the acceleration factor of 8 as a reference image. **(C-2)** and **(C-3)** are the images with echo times 800, 500μs at fixed matrix size of 128×128×64, and the acceleration factor of 4.

Application CS-MMME to in vivo experiments

Firstly, CS-MMME images were acquired using a rat. Sagittal slices in 3D image with the matrix size of 128×128×64, and the acceleration factors of 4 and 8 were shown in **Figure 3.3.4 (B-1)** and **(B-2)**, respectively. Same images with the matrix size of 256×256×64, and the acceleration factors of 8 and 16 were shown in **Figure 3.3.4 (C-1)** and **(C-2)**. The high resolution image in **Figure 3.3.4 (C-1)** provided more accurate anatomical information than other images. The number of excitations would reduce when the acceleration factor is increased, but induces more blurred images.

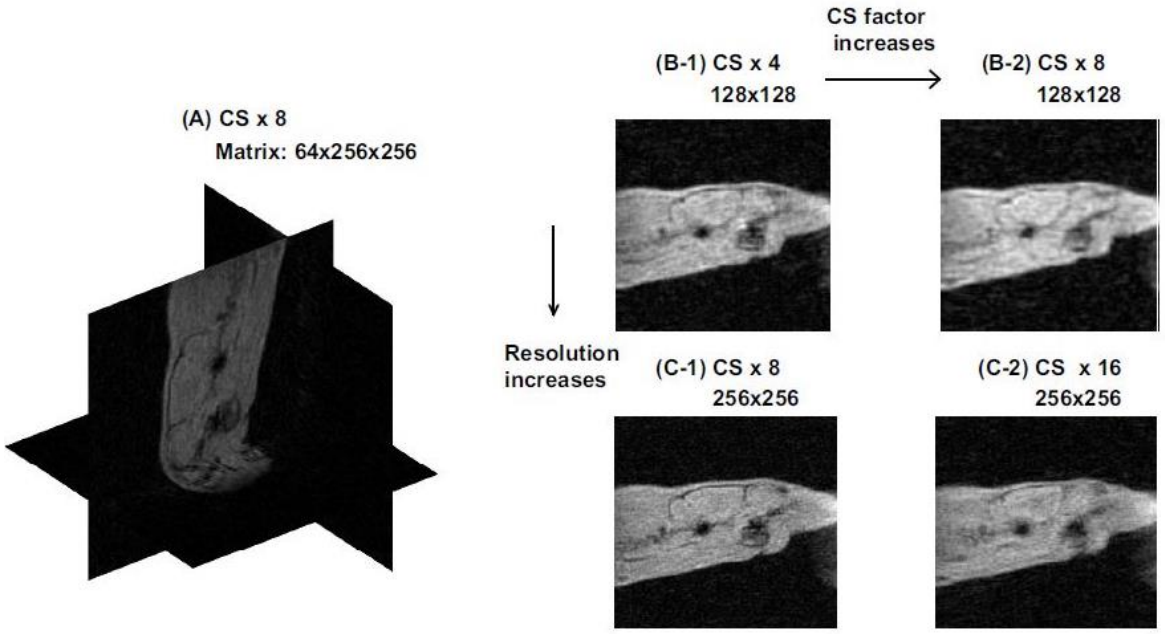

Figure 3.3.4 (A) 3D image of rat with the matrix size of 256×256×64. **(B-1)** and **(B-2)** are the CS-MMME images with echo time of 500μs, the matrix size of 128×128×64, MMME factor of 32, and the acceleration factors of 4 and 8. **(C-1)** and **(C-2)** are the CS-MMME images with echo time of 500μs, the matrix size of 256×256×64, MMME factor of 32, and the acceleration factors of 8 and 16.

Secondly, CE-MRI was acquired by the administration of Gd-DOTA with CS-MMME and FLASH images at the doses of 0.1 and 0.3mmol/kg. Pre-injection images of kidney region with FLASH and CS-MMME at TR of 250ms were shown in **Figure 3.3.5 (A-1)** and **(B-1)**. And post-injection images with FLASH and CS-MMME were shown in **Figure 3.3.5 (A-2)** and **(B-2)**. At the administration dose of 0.3mmol/kg, CS-MMME image showed a positive contrast enhancement (S_{post}/S_{pre}) of 3.89 in the kidney region. On the other hand, negative contrast enhancement as 0.39 was observed in FLASH even at minimum TE. In a lower administration dose as 0.1mmol/kg, CS-MMME showed a positive contrast enhancement of 3.62 as shown in **Figure 3.3.5 (B-4)**. But, negative contrast enhancement as

0.89 was observed in FLASH even at lower administration dose of 0.1mmol/kg as shown in **Figure 3.3.5 (A-4)**. Pre-injection images were shown in **Figure 3.3.5 (A-3)** and **(B-3)**.

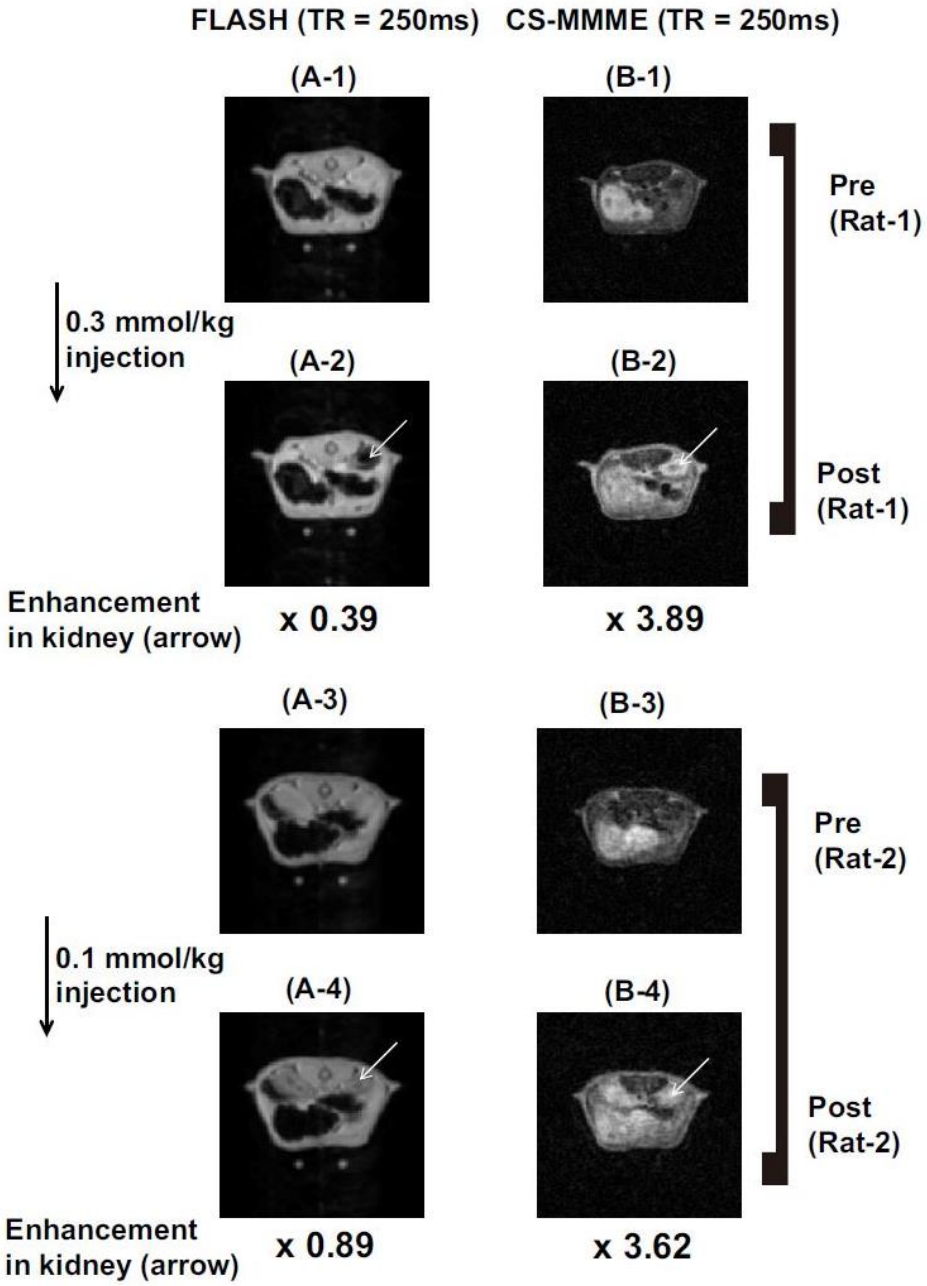

Figure 3.3.5 At the administration dose of 0.3mmol/kg, **(A-1)** and **(B-1)** are FLASH and CS-MMME images before the injection of Gd-DOTA at TR of 250ms. Corresponding images after the injection of Gd-DOTA are shown in **(A-2)** and **(B-2)**. At the administration dose of 0.1mmol/kg, **(A-3)** and **(B-3)** are FLASH and CS-MMME images before the injection of Gd-DOTA. Corresponding images after the injection of Gd-DOTA are shown in **(A-4)** and **(B-4)**.

Comparisons of contrast enhancement were calculated for rats (N = 4) with different TR were plotted in **Figure 3.3.6**. Contrast enhancement was increased when TR decreases for FLASH and CS-MMME. CS-MMME showed significantly improved positive contrast enhancement compared to conventional FLASH. The contrast enhancement at high administration dose as 0.3mmol/kg was significantly increased compared to that at low dose as 0.1mmol/kg in CS-MMME. But there was not significantly different between high dose and low dose enhancements in FLASH.

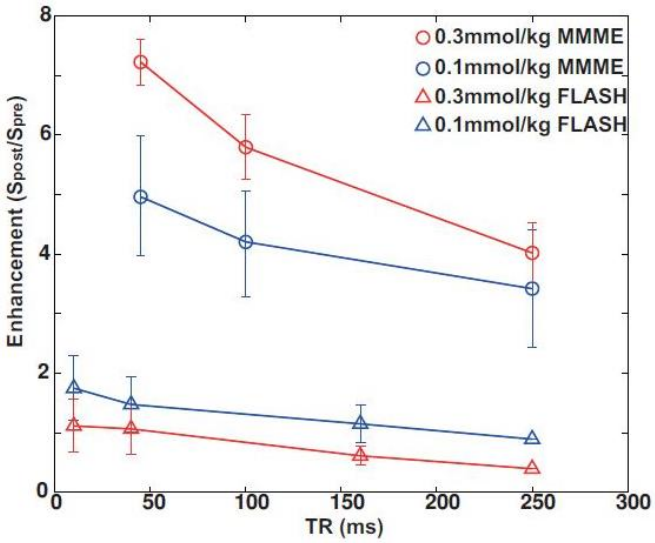

Figure 3.3.6 The contrast enhancement of CS-MMME and FLASH was plotted at the administration doses of 0.1 and 0.3mmol/kg at various TR.

3.3.4 Discussion and conclusions

CS-MMME proposes the potential strategy to acquire more accurate 3D proton density and T_1-weighted images due to minimized T_2, diffusion effects, and susceptibility artifact with minimized RF excitations. Furthermore, CS-MMME will provide accurate estimation of contrast agent concentrations over a wide range of administration dose and TR, which can avoid tricky positive contrast enhancement optimization with conventional gradient echo based sequences. The temporal resolution of 3D CS-MMME reaches about 7s for the matrix size of 128×128×128, MMME factor of 32, and the acceleration factor of 4. The speed of acquisition is significantly increased compared to corresponding 3D FLASH (~ 120s) and 3D RARE with RARE factor of 32 (~190s), but comparable to EPI (~10s). In case of the application of CS to FLASH, RARE, and EPI, the speed of acquisition is as follows: CS-EPI (2.5s) < CS-MMME (7s) < CS-FLASH (30s) < CS-RARE (48s) for the same TR and TE. The MR parameters are determined according to the purpose of the experiments. For this reason, 3D CS-MMME also should balance the tradeoffs between the acceleration factor and the image quality. As an example, lower MMME factor increases SNR of the image, but increases the number of repetitions to fill 3D *k*-space, which causes prolonged acquisition time. And the increase of acceleration factor can decrease scan time, but induces blurring artifact in the reconstructed image. Also, reduced MMME echo time would be beneficial to minimize T_2 and diffusion decays. On the other hand, echoes would overlap as echo time is too small, and stronger gradient strength is required to separate echoes for proper encodings, which increases diffusion decay. Also, when echo time is short as 500μs, only about 100 points along readout direction are sampled with dwell time of 5μs, which reduces the size of the matrix for readout direction. The clinical application of 3D CS-MMME is out of the scope for this work at this point, but it is worth to mention. The restricted maximum gradient strength and its slew rate of clinical scanner would limit the parameters for CS-MMME. This limitation would lead to increased echo time of CS-MMME, increasing TR for the clinical applications, which require further optimization steps.

We proved the feasibility of 3D CS-MMME sequence for acquiring proton density or T_1-weighted images with fewer RF excitations on various phantoms and animals. The first benefit is the maximized ratio of the number of echoes per RF pulse (6.4), which enables the acquisition of proton density or T_1-weighted images with reasonable scan time comparable to EPI and reduced RF power deposition. Second benefit is minimized T_2 effect even at a large MMME factor.

In conclusion, CS-MMME sequence showed the possibility to acquire 3D T_1-weighted spin echo based imaging by combining CS with MMME with the total acceleration factor as 128~256. Also, spin echo based CS-MMME improves the contrast enhancement in CE-MRI with minimized susceptibility artifact.

Chapter 4. Alternative methods to improve accuracy in detecting microvasculature

4.1 Robust assessment of cerebral blood volume and mean vessel size using SPION

4.1.1 Introduction

Cerebrovascular related diseases, vascular malfunction, and neovascularization within tumor are often caused by the alternation in microvascular parameters such as cerebral blood volume (CBV) and vessel size [82-88]. Detection of variation in microvasculature plays an important role in assessing brain diseases and monitoring the therapeutic response in both preclinical and clinical settings [89]. Many non-invasive methods for estimation of microvasculature have been developed, such as iodinated contrast radiography [90-91], positron emission tomography using oxygen-15-labeled carbon monoxide [92-95], and single photon emission computed tomography using 99 mTc-pertechnetate labeled red blood cells [96]. On the other hand, the lack of spatial resolution and exposure to ionizing radiation limit for the accurate quantification of microvasculature such as CBV and vessel size. Recently, many methods using MRI with various contrast agents have been investigated to overcome these limitations of radioactive tracer approaches [97-99]. Especially, the contrast agent called superparamagnetic iron oxide nanoparticles (SPION) has a long blood half-life [100]. SPION induces susceptibility perturbations in surrounding tissue as shown by an increase in the transverse relaxations (ΔR_2 and ΔR_2^*) [101-102]. The change in transverse relaxation is used to calculate CBV and microvascular volume (MVV) which are used for microvascular characterizations [103]. However, measurements of MR transverse relaxation may not present a representative regional comparison of vascular parameters. For example, the magnitude of susceptibility-induced field inhomogeneities is changed by the capillary direction with respect to B_0 magnetic field, which deteriorates the quantification of CBV from ΔR_2 or ΔR_2^* [104-105]. Furthermore, ΔR_2^* based CBV can be biased in tissue neighboring large vessels or air tissue interface [106]. These tissue environment variations can complicate the measurement of CBV in regions such as cortex, where vessels are well aligned, and olfactory bulb and cerebellum, which are close to air-tissue interface. Additionally, accurate quantification of SPION concentration is needed to avoid dose dependency of transverse relaxation. When regional and dose independent measurement of CBV is required, the ratio between tissue and vessel signal enhancements correspond to the fractional blood volume from ΔR_1 is preferable rather than ΔR_2 and ΔR_2^*. ΔR_1 is not influenced by susceptibility-induced artifact from

vessel structure, and realizes dose independent concentration ratio of the contrast agent. Moreover, $\Delta R_2^*/\Delta R_2$ is used to assess mean vessel size index (mVSI) by taking advantage of strong transverse relaxation rates of SPION and diffusion modeling in the presence of susceptibility-induced field [107]. On the other hand, susceptibility-induced field inhomogeneities due to variation in vessel orientation or air-tissue interface would affect the accuracy of mVSI estimation. Previously, Gd-based T_1 and SPION-based T_2/T_2^* contrast agents were used to extract both CBV from ΔR_1 and mVSI from $\Delta R_2^*/\Delta R_2$ [108-110]. More recently, ultra-short echo time (UTE) sequence minimizes susceptibility perturbations [111-114], and shows the opportunity to acquire dual-contrast effect using a single contrast agent, SPION [115]. However, direct comparison between UTE-based and ΔR_2^*-based CBV measurement has not been investigated.

In this work, Monte-Carlo simulations were performed to represent the dependence of transverse relaxation in vessel orientation and bias in ΔR_2^* near air-tissue interface. In addition, the feasibility of alternative mVSI measurement with UTE-based CBV was shown and proved. And direct comparison of UTE-based and ΔR_2^*-based CBV was performed in cortex, olfactory bulb, and cerebellum regions in nude mice. For the validation of alternative mVSI, $\Delta R_2^*/\Delta R_2$ and UTE-based CBV/ΔR_2 were compared in the same brain regions. After that, the relationship between UTE-based and ΔR_2^*-based CBV was investigated in cortex, olfactory bulb, caudate putamen, thalamus, superior colliculus, and cerebellum. Moreover, the relation between $\Delta R_2^*/\Delta R_2$ and UTE-based CBV/ΔR_2 was investigated for same regions as well. Furthermore, UTE-based CBV was compared with previously reported CBV in many studies. Finally, dose dependence of UTE-based and ΔR_2^*-based CBV was investigated.

4.1.2 Materials and Methods

Monte-Carlo (MC) simulation information

All MC simulations were performed using in-house matlab code, which is similar to the method in [116]. Firstly, 3D-binary matrices were generated to set the vascular structure with randomly oriented cylinders. The number of vessels corresponded to the blood volume fraction (V_b). For example, around 100 cylinders were used for 2% blood volume, and the blood volume fraction was set to 5% and 10%. The vessel length was generated to be 40 times greater than the vessel radius (R_v). The 3D-binary matrix was generated three times to calculate mean and standard deviation for each data point. Secondly, finite perturber method (FPM) was applied to calculate the magnetic field shift by the contrast agent filling the cylinder using the Fourier convolution theorem [116]. Finally, MC was performed to calculate the change of transverse relaxations (ΔR_2 and ΔR_2^*) by proton diffusion with susceptibility-induced inhomogeneous magnetic field. 200,000 protons were positioned randomly within the diffusion space. Each proton was moved randomly with increment of the interval (Δt) at standard deviation of displacement as the diffusion length calculated as $\sqrt{2D\Delta t}$, where D is the diffusion coefficient, and each spin experienced different magnetic field shifts. These steps induced the phase accumulation of each spin at each interval time (Δt). The total phase accumulation of the nth proton during total time t was as following equation,

$$\phi_n(t) = \sum_{i=1}^{t/\Delta t} \gamma \Delta B(P_n(i\Delta t))\Delta t \qquad (4.1.1)$$

where Δt is the diffusion time interval, γ is gyromagnetic ratio of proton, $P_n(t)$ is the position of nth proton, and $\Delta B(P_n(t))$ is the magnetic field shift at position $P_n(t)$. After that, MR signal was calculated as following equation,

$$S(t) = \frac{1}{N}\sum_{n=1}^{N} e^{i\phi_n(t)} \qquad (4.1.2)$$

Using calculated MR signal, the change in transverse relaxations was calculated as following equation,

$$\Delta R_2, \Delta R_2^* = -\frac{\ln[S(TE)]}{TE} \qquad (4.1.3)$$

The following simulation parameters were fixed: the number of total spins was 2×10^5, diffusion coefficient (D) was 10^{-5} cm^2/s, diffusion time interval was set to 0.2ms, and the simulation was repeated 200 times to obtain mean MR signal. On the other hand, V_b, R_v, B_0, $\Delta\chi$, TE were varied.

Vulnerability of transverse relaxation due to vessel orientation and air-tissue interface

In this simulation, V_b was set to 2%, R_v as 2μm, B_0 as 3T along the *z* direction, $\Delta\chi$ as 4×10^{-7}, and TE for spin echo (SE) and gradient echo (GE) were set to 100ms, and 15ms, respectively. The degree of randomness of vessel orientation was varied 0% (all aligned) to 100% (completely random) while keeping V_b as shown in subsection of **Figure 4.1.1 (A-1)**. The vessel orientation effect for ΔR_2 and ΔR_2^* with three directions along x, y, and z by varying the randomness was simulated as in **Figure 4.1.1 (A-1)** and **(A-2)**, respectively. Secondly, the simulation for air-tissue interface effect was performed by increasing air-bubble size. The air-bubble was set as a sphere and located in the center region of the simulation space in a completely random vessel orientation. The example of increasing the bubble size was shown in subsection of **Figure 4.1.1 (B)**. The ratio of the bubble radius to the simulation space size was varied from 0 to 0.2, and the susceptibility difference between air-bubble and tissue was set to 7×10^{-7}.

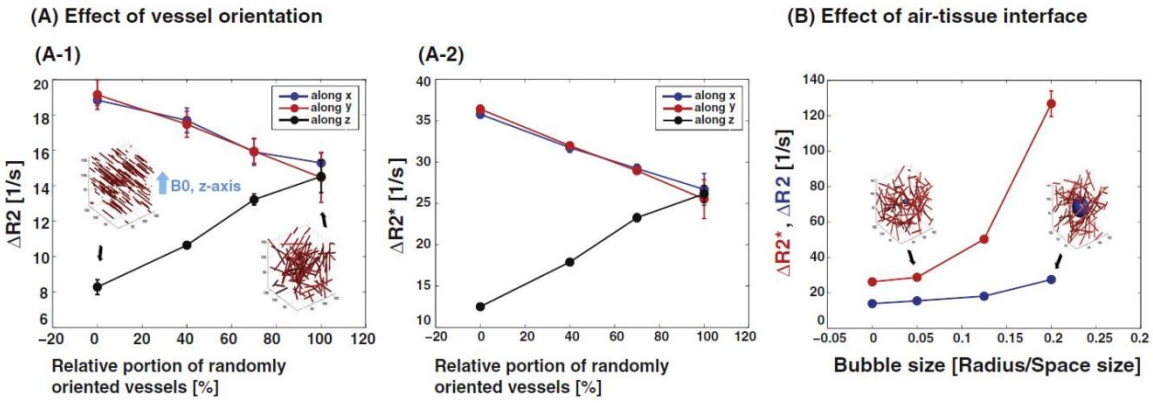

Figure 4.1.1 (A-1), **(A-2)** ΔR_2 and ΔR_2^* with three directions along x, y, and z as a function of randomness. **(B)** Air-tissue interface simulation as a function of bubble size.

Alternative mean vessel size index simulation

To show the feasibility of alternative mean vessel size (mVSI) as UTE-based CBV/ΔR_2, the vessel size dependency in ΔR_2, ΔR_2^*, $\Delta R_2^*/\Delta R_2$, and UTE-based CBV/ΔR_2 was simulated. B_0 was 3T and susceptibility difference between pre and post administration of SPION was set to 2×10^{-7}, and 4×10^{-7}, respectively [106]. And V_b was varied as 2%, 5%, and 10%, and these values were used as UTE-based CBV for the simulation. Rv was varied from 1μm to 23μm as shown in **Figure 4.1.2**.

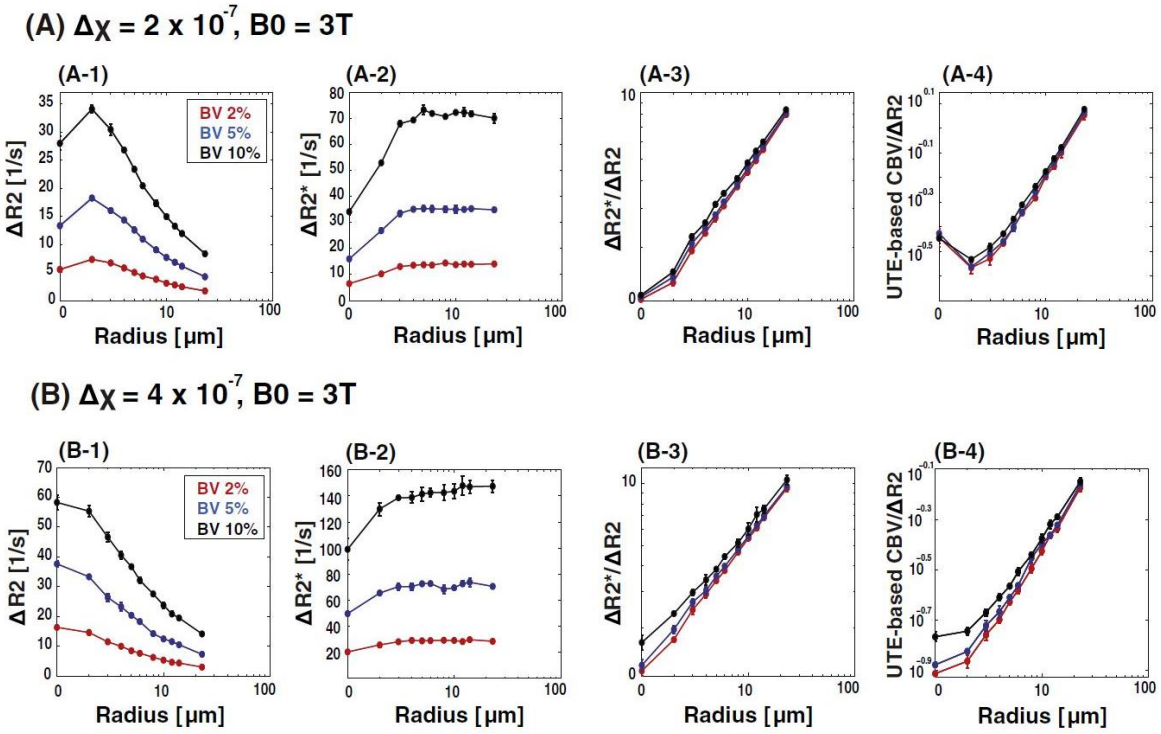

Figure 4.1.2 ΔR_2 **(A-1)**, and **(B-1)**, ΔR_2^* **(A-2)**, and **(B-2)**, $\Delta R_2^*/\Delta R_2$ **(A-3)**, and **(B-3)**, and UTE-based CBV/ΔR_2 **(A-4)**, and **(B-4)**. A and B show the effect of different susceptibility difference as 2×10^{-7}, and 4×10^{-7}, respectively. V_b was varied 2% (red), 5% (blue), and 10% (black).

In vivo experiments scanner, animal, and contrast agent

All experiments were performed on 3T MRI scanner (Philips Achieva, Best, Netherlands), and Institutional Animal Care and Use Committee of the Korea Basic Science Institute approved *in vivo* experiments. A total 29 male nude mice (20~28g) were used in this study. The contrast agent was SPION which was characterized in previous study [34]. The administration dose was varied by 70μmol/kg (n = 21), 120μmol/kg (n = 4), and 140μmol/kg (n = 4).

Regional CBV measurement criteria

Anatomical brain atlas template for mouse was registered to the T_2^*-weighted images from MEGE sequence to generate the mask for regional information. Anatomical mouse brain template was acquired at http://scalablebrainatlas.incf.org/main/coronal3d.php?template=WHS10. Slice averaging of template was firstly performed because the slice thickness between template and T_2^*-weighted image was different.

CBV measurement with UTE acquisition

UTE acquisition was performed with the following parameters: Flip angle (FA) = 90°, TR = 50ms, TE = 90μs, FOV = 5×5×8 cm^3, and spatial resolution = 195×195×1000 μm^3. The signal intensities of before and after the administration were presented by ($S_{tissue\_pre} = (1-V_b)S_{extra} + V_bS_{intra}$) and ($S_{tissue\_post} = (1-V_b)S_{extra} + V_bS_{intra}'$) based on two compartment model with intravascular and extravascular spaces. S_{extra} and S_{intra} are the signal intensities of extravascular and intravascular spaces before administration of SPION. The signal intensity is only altered in intravascular space because SPION is intravascular contrast agent (S_{intra}'). By taking advantage of this behavior, V_b was calculated by the following equation,

$$V_b = \frac{S_{tissue\_post} - S_{tissue\_pre}}{S_{bloop\_post} - S_{bloop\_pre}} \qquad (4.1.4)$$

CBV measurement with MEGE acquisition

MEGE images were acquired with the following parameters to measure ΔR_2^*: FOV = 5×5×2.4 cm^3, spatial resolution = 195×195×1000 μm^3, TR = 3000ms, and TE = 7, 13, 19, 25, 31, and 37ms. The signal differences before and after the administration of SPION were converted to ΔR_2^* at TE of 15ms, using the single exponential model. By the following equation with the assumption that the static dephasing was dominant, CBV (%) was estimated [105].

$$\Delta R_2^* = \frac{4}{3}\pi \cdot (1 - Hct) \cdot V_b \cdot \Delta\chi \cdot \gamma B_0 \qquad (4.1.5)$$

where *Hct* is the hematocrit as 0.4, and $\Delta\chi$ is the susceptibility difference at 3T as 0.36 ppm [106].

ΔR_2^*-based and UTE-based mVSI

MSME images were acquired with the following parameters to measure ΔR_2: FOV = 5×5×2.4 cm^3, spatial resolution = 195×195×2000 μm^3, TR = 3800ms, and TE = 60, and 100ms. The signal differences before and after the administration of SPION were converted to ΔR_2 at TE of 60ms, using the single exponential model. ΔR_2^*-based mVSI was calculated as $\Delta R_2^*/\Delta R_2$, and UTE-based mVSI was calculated as UTE-based CBV/ΔR_2.

4.1.3 Results

Vulnerability of transverse relaxation due to vessel orientation and air-tissue interface

Figure 4.1.1 (A) represented the relation of ΔR_2^*, and ΔR_2 as a function of randomness of vessel orientation while maintaining V_b as 2%. The directions of alignment along x, y, and z were showed as blue, red, and black lines, respectively. Similar behavior between ΔR_2 and ΔR_2^* was shown in **Figure 4.1.1 (A)**. ΔR_2^*, and ΔR_2 were decreased as the randomness of vessel orientation was increased for x and y directions, but opposite behavior was shown for z direction. **Figure 4.1.1 (B)** represented the relation ΔR_2^*, and ΔR_2 as a function of the size of air-bubble to investigate the effect of air-tissue interface. Both ΔR_2^*, and ΔR_2 were increased as the size of air-bubble was increased. On the other hand, the degree of increase of ΔR_2^* was much higher than that of ΔR_2, which means that ΔR_2^* is more sensitive to air-tissue interface than ΔR_2.

Alternative mean vessel size index simulation

The vessel size dependency in ΔR_2, ΔR_2^*, $\Delta R_2^*/\Delta R_2$, and UTE-based CBV/ΔR_2 was shown in **Figure 4.1.2**. Three different blood volume fractions of 2, 5, and 10% were simulated and depicted as red, blue, and black lines, respectively. In case of **Figure 4.1.2 (A)** with $\Delta\chi$ of 2×10^{-7}, ΔR_2 showed the peak point at around 2μm and was decreased as the vessel radius was increased as shown in **Figure 4.1.2 (A-1)**. And ΔR_2^* showed the peak point at around 3μm and was plateaued as the vessel radius was increased as shown in **Figure 4.1.2 (A-2)**. This shape was observed for all three different V_b. In case of **Figure 4.1.2 (B)** with $\Delta\chi$ of 4×10^{-7}, ΔR_2 was steadily decreased as the vessel radius was increased as shown in **Figure 4.1.2 (B-1)**. And ΔR_2^* showed the peak point rapidly than **Figure 4.1.2 (A-2)** and was plateaued as the vessel radius was increased as shown in **Figure 4.1.2 (B-2)**. After showing ΔR_2, ΔR_2^*, mVSI as $\Delta R_2^*/\Delta R_2$ and alternative mVSI as UTE-based CBV/ΔR_2 were plotted in **Figure 4.1.2 (3)** and **(4)**, respectively. There was no significant difference in V_b for both $\Delta R_2^*/\Delta R_2$ and UTE-based CBV/ΔR_2. For $\Delta\chi$ of 2×10^{-7}, UTE-based CBV/ΔR_2 was followed $\Delta R_2^*/\Delta R_2$ except at low radius below 2μm as shown in **Figure 4.1.2 (A-4)**. For $\Delta\chi$ of 4×10^{-7}, UTE-based CBV/ΔR_2 was steadily increased, which is in a good agreement with $\Delta R_2^*/\Delta R_2$. This linear relation between UTE-

based CBV/ΔR_2 and vessel radius and its independency of V_b showed the feasibility in estimating mVSI at our experimental conditions.

Comparison of CBV and mVSI maps from UTE, MEGE, and MSME

Voxel-wise CBV, and mVSI maps from UTE, MEGE, and MSME sequences were shown in **Figure 4.1.3** in cortex, cerebellum, and olfactory bulb regions in mouse brain. T_2^*-weighted images for cortex, cerebellum, and olfactory regions in mouse brain were shown in **Figure 4.1.3 (A)**. UTE-based CBV, ΔR_2^*, ΔR_2, $\Delta R_2^*/\Delta R_2$, UTE-based CBV/ΔR_2 maps were shown in **Figure 4.1.3 (B)**, **(C)**, **(D)**, **(E)**, and **(F)**, respectively. In terms of CBV, there was significant differences between UTE-based CBV and ΔR_2^* as indicated in **Figure 4.1.3 (B-1)** and **(C-1)** with black arrow. UTE-based CBV showed positive value in black arrow, but ΔR_2^* showed negative value in corresponding arrow. For the region indicated by black arrow in **Figure 4.1.3 (B-2)**, signal enhancement was not observed because this region is near from ears, but ΔR_2^* showed negative enhancement as shown in **Figure 4.1.3 (C-2)**. These results proved that UTE-based CBV distinguished the high blood volume fraction region from air-tissue interface, but ΔR_2^* failed to distinguish two different areas due to stronger air-tissue artifacts of ΔR_2^* as shown in the previous simulational results. Moreover, spatial shift was observed in ΔR_2^* maps because of the field inhomogeneity, which would require additional image registration step for direct comparison. As a result, $\Delta R_2^*/\Delta R_2$ showed an unstable behavior as shown in **Figure 4.1.3 (E)** as white arrows. On the other hand, UTE-based CBV/ΔR_2 map showed apparently stable behavior in corresponding region, indicated by the white arrows as shown in **Figure 4.1.3 (F)**.

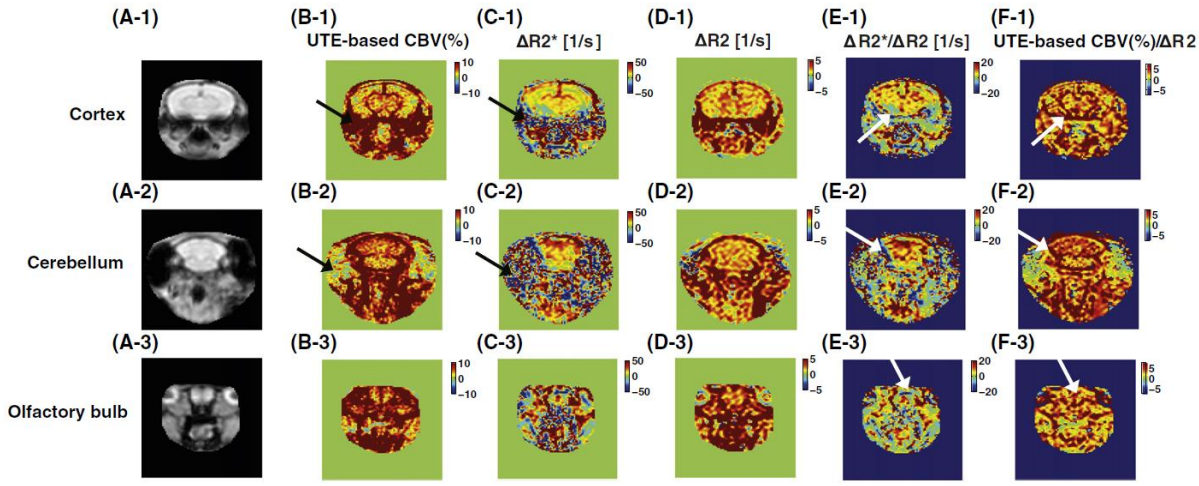

Figure 4.1.3 (A) T_2^*-weighted images before administration of SPION. **(B), (C), (D), (E),** and **(F)** are UTE-based CBV, ΔR_2^*, ΔR_2, $\Delta R_2^*/\Delta R_2$, UTE-based CBV/ΔR_2 maps for cortex, cerebellum, and olfactory bulb regions in mouse brain.

Comparison of CBV and mVSI

Firstly, Comparisons of ΔR_2^*-based and UTE-based CBV values for cortex, thalamus, caudate putamen, olfactory bulb, superior colliculus, and cerebellum were plotted in **Figure 4.1.4 (A)** and its standard deviation of the measured CBV was also marked as vertical line. ΔR_2^*-based CBV showed larger standard deviation than that from UTE-based CBV. On the other hand, ΔR_2^*-based and UTE-based CBVs showed the linear correlation when a large number of samples were calculated. Moreover, UTE-based CBV for various regions was compared with previously reported CBV for validating the feasibility of UTE-based CBV measurement as shown in **Table 1**. CBV ratio was calculated by dividing each CBV by CBV of cortex region to identify the correlation between CBV values in the different studies. The CBVs from cortex, thalamus, caudate putamen, olfactory bulb, superior colliculus, and cerebellum were consistent with earlier reports. For example, CBV in the cortex region was 2.03 and that from earlier reports were 1 to 4, which indicates a good agreement between those of two. Similar trend was investigated in thalamus, caudate putamen, and cerebellum regions. On the other hand, CBVs in olfactory bulb and superior colliculus regions were higher than earlier reports.

Secondly, $\Delta R_2^*/\Delta R_2$ and UTE-based CBV/ΔR_2 were compared as shown in **Figure 4.1.4 (B)**. UTE-based mVSI showed reduced linearity (r^2 (all) = 0.04, r^2 (w/o olfactory) = 0.49, r^2 (w/o olfactory & thalamus) = 0.85) compared to CBV (r^2 = 0.90). The reduced linearity would come from the relative spatial shift of ΔR_2^* with respect to ΔR_2, and UTE.

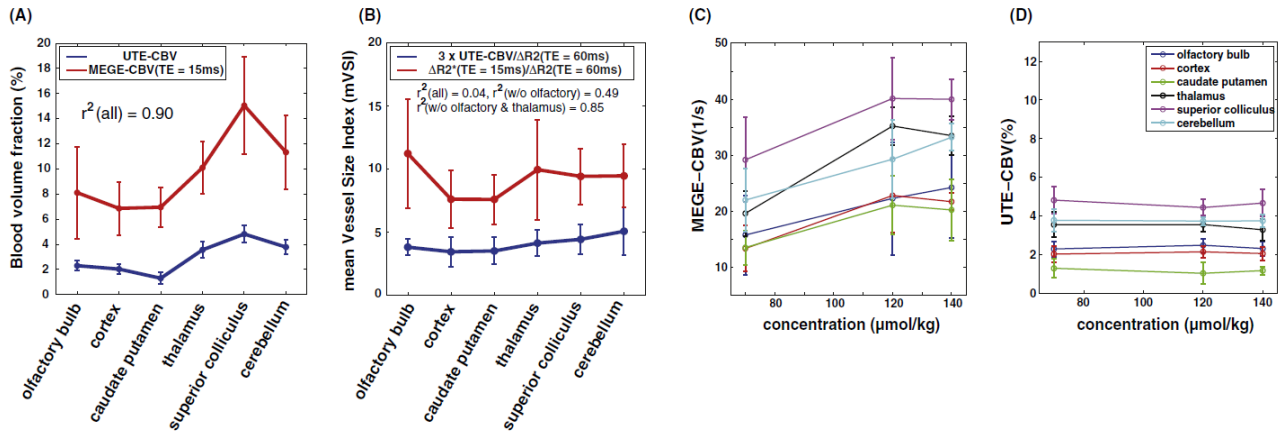

Figure 4.1.4 (A) ΔR_2^*-based and UTE-based CBV in olfactory bulb, cortex, caudate putamen, thalamus, superior colliculus, and cerebellum regions. **(B)** $\Delta R_2^*/\Delta R_2$ and UTE-based CBV/ΔR_2 comparison for various regions. **(C)** ΔR_2^*-based and **(D)** UTE-based CBV at the administration doses of 70μmol/kg (n = 21), 120μmol/kg (n = 4), and 140μmol/kg (n = 4).

Table 1

CBV compared between previous reports and current study for cortex, thalamus, caudate putamen, olfactory bulb, superior colliculus, and cerebellum regions. CBV ratio was calculated by dividing CBV with the CBV of cortex region to identify the correlation of CBV between current and previous work.

	CBV(ml·100g^{-1})	CBV ratio	Method	animal
Cortex	4.07	1	MRI [105]	Rat
	1.63	1	MRI [117]	Rat
	1.13	1	Autoradiography [118]	Rat
	1.03	1	MRI [119]	Mouse
	0.934	1	CT [120]	Rat
	3.26	1	MRI [121]	Rat
	2	1	Autoradiography [122]	Rat
	2.44	1	CT [123]	Rat
	2.03	1	**MRI(our study)**	**Mouse**
Thalamus	3.03	1.86	MRI [117]	Rat
	1.11	0.98	Autoradiography [118]	Rat
	1.1	1.07	MRI [119]	Mouse
	0.785	0.84	CT [120]	Rat
	3.56	**1.75**	**MRI(our study)**	**Mouse**
Caudate putamen	2.87	0.71	MRI [105]	Rat
	0.88	0.78	Autoradiography [118]	Rat
	0.629	0.673	CT [120]	Rat
	2	0.82	CT [123]	Rat
	1.3	**0.64**	**MRI(our study)**	**Mouse**
Olfactory bulb	1.07	1.04	MRI [119]	Mouse
	2.3	**1.13**	**MRI(our study)**	**Mouse**
Superior colliculus	1.31	1.27	MRI [119]	Mouse
	1.03	1.10	CT [120]	Rat
	4.82	**2.37**	**MRI(our study)**	**Mouse**
Cerebellum	1.17	1.14	MRI [119]	Mouse
	1.09	1.17	CT [120]	Rat
	4.28	1.31	MRI [121]	Rat
	3.78	**1.86**	**MRI(our study)**	**Mouse**

Comparison of dose dependency in ΔR_2^*-based and UTE-based CBV

The dose dependency in ΔR_2^*-based and UTE-based CBV in various regions in brain was plotted in **Figure 4.1.4 (C)** and **(D)**, respectively. The increase in the administration dose causes elevated $\Delta\chi$ [116], therefore, ΔR_2^*-based CBV was increased as shown in **Figure 4.1.4 (C)**. For this reason, dose correction is required to convert ΔR_2^* to CBV. However, UTE-based CBV showed constant as a function of administration dose. This behavior showed the stability of the measurement of CBV with UTE sequence with varying doses.

4.1.4 Discussion and conclusions

Microvascular parameters such as CBV and mVSI are detected using the change of transverse relaxation by SPION, i.e., ΔR_2, and ΔR_2^*. On the other hand, transverse relaxation from gradient echo sequence often causes severe artifacts in estimating such microvascular parameters by the variation in geometrical and environmental conditions. In this work, we theoretically and experimentally proved that replacing ΔR_2^* to UTE-based ΔR_1 for acquiring CBV and mVSI by taking advantage of the dual contrast agent ability of SPION.

As shown by MC simulations, ΔR_2^*-based CBV *in vivo* showed larger standard deviation than those from UTE-based CBV. Different geometrical information of vessel, and shimming value would account for ΔR_2^* variations. This unwanted variation of ΔR_2^* should be considered especially in longitudinal studies. However, ΔR_1 is less influenced by these environmental conditions because R_1 measurement isn't dependent on the spin signal dephasing due to molecular diffusion in the presence of field inhomogeneity. This behavior was verified by measuring regional CBV *in vivo* experiments (n = 29) with UTE sequence. Moreover, mVSI from $\Delta R_2^*/\Delta R_2$ showed severe artifacts near air-tissue interface region and large vessel region due to inevitable variations in ΔR_2^*. On the other hand, mVSI from UTE-based CBV/ΔR_2 showed stable values even near air-tissue interface region and large vessel region.

Another potential of dual contrast is that UTE-based CBV is independent on the size of underlying vessels. In other words, when we need vessel size information for the specific purpose, UTE-based CBV and UTE-based CBV/ΔR_2 can be separately measured using a single agent.

It should be mentioned that UTE-based CBV with SPION which is independent on the hematocrit and susceptibility effect shows fractional CBV, while dynamic susceptibility contrast (DSC)-MRI is known to provide absolute CBV. Direct comparisons between absolute CBV and fractional CBV would represent the potential and limitations of UTE-based CBV. In addition, even we minimized TE from UTE acquisition with 90° flip angle, the assumption of R_1 – insensitivity of extravascular space from intravascular SPION is not proved yet, and future work may focus on either compensating or

utilizing these potential errors of quantification of vascular parameters. And a potential limitation of our work is SPION is not clinically approved yet. On the other hand, iron oxide nanoparticle (Feraheme, AMAG Pharmaceuticals, Lexington, MA, USA) has been approved for the treatment of iron deficiency anemia, which is equivalent to SPION chemically.

In conclusion, UTE acquisition minimizes susceptibility artifacts and environmental dependency by taking advantage of the dual contrast agent of SPION, and provides alternative, but potentially more robust CBV measurements from ΔR_1 and mVSI from UTE-based CBV/ΔR_2. Developed methodology shows the potential to enable clear quantification of vascular parameters in longitudinal studies of microvascular brain disease with future studies.

4.2 MR tractography using magnetic field anisotropy

4.2.1 Introduction

Detection of fiber orientation in tissues such as fiber pathways in brain white matter or heart muscles provides the information about the connectivity and functionality. For example, diffusion tensor imaging (DTI) measures the degree of the restriction of apparent diffusion constant (ADC) of water molecules for multiple orientations to detect the tissue anisotropy of brain white matter known as tractography [124-126].

Although DTI is well-used for tractography, DTI may be limited when the ADC anisotropy is small, which is occurred in large capillaries. Furthermore, it may be limited at high magnetic field because susceptibility-induced magnetic field inhomogeneity is increased and causes the degradation in the DTI signal sensitivity and its resolution [127-128]. In other words, susceptibility-induced magnetic field inhomogeneity from anisotropy of tissue would be an alternative way to acquire orientation at higher magnetic field, and their presence was clearly demonstrated in both white matter and capillary vessels [129-130]. On the other hand, this method may not be practical because re-orientation of the subject is required for anisotropic susceptibility field mapping.

The purpose of this work is to validate new procedures for acquiring tractography at high magnetic field without requiring re-orientation of the subject by performing simulations and experiments. We propose a stimulated echo based MRI methodology which can track the signal decay of the diffusing spins in the presence of susceptibility induced magnetic field gradient to detect the orientation information without the need of re-orientation of the subject, even when ADC is uniform. For instance, the magnetic field inside the sample would be inhomogeneous for grain-fluid porous media and biological cells when the different magnetic susceptibility levels are immersed in a uniform magnetic field [131-135]. And, the magnitude and direction of internal field is closely related to the orientation corresponding to the applied field for cylindrical sample such as capillaries [135]. For example, no internal field gradient is shown along the orientation of the cylindrical axis. Therefore, the orientation of the minimum internal gradient distribution reflects the main capillary orientation.

In conventional technique such as spin echo sequences [136], only the magnitude of the field gradients is typically measured and it is insensitive to the orientation anisotropy of the internal gradient. Recently, we have developed a method to measure the magnitude and direction of the internal gradient ($\mathbf{g}_{int}$), taking advantage of the interference effect between the internal gradient and applied pulsed field gradient (PFG) [137]. Measurements with multiple projections of internal gradient ($\mathbf{g}_{int}$) along multiple PFG directions can characterize its orientation. As a result, the orientation of the minimum internal gradient distribution can be determined from interference experiments with different orientations of PFG in the purpose of determining the axis direction of

cylindrical geometries.

Firstly, we showed that an anisotropic susceptibility-induced magnetic field gradient exists in a single capillary when magnetic field component is perpendicular to the capillary axis. Secondly, we extended this method by determining a numerical calculation for a randomly packed capillary model to validate the mapping of angular dependence of the internal gradient distribution. The estimation of the orientation of the minimum width coincided with the orientation of cylindrical axis of capillaries, based on the similar method used in conventional DTI tractography. Third, we obtained the interference patterns between the internal and external field gradients with a stimulated echo based method using a randomly packed capillary model. We showed the feasibility of the measurement of anisotropic distribution of the internal gradient and the orientation of the capillary without rotating the sample experimentally. Finally, the sensitivity of proposed tractography was confirmed when the spatial resolution is not sufficient to resolve the pore structure so that only internal gradient distribution can be measured. Theoretical and experimental validations of proposed method showed the feasibility to detect capillary orientation without re-orientation of the subject, even when ADC values were homogeneous.

4.2.2 Materials and Methods

To visualize the anisotropic susceptibility magnetic field, the susceptibility-induced internal field gradient for a single capillary which is perpendicular to main magnetic field B_0 was considered as shown in **Figure 4.2.1 (A)**. The analytical solution of internal field gradient outside the capillary is as following [138-139],

$$g_{int}^{x} \simeq B_0 \Delta\chi (a^2 - b^2) x \frac{x^2 - 3y^2}{(x^2+y^2)^3} \qquad (4.2.1)$$

$$g_{int}^{y} \simeq B_0 \Delta\chi (a^2 - b^2) y \frac{y^2 - 3x^2}{(x^2+y^2)^3} \qquad (4.2.2)$$

$$g_{int}^{z} = 0 \qquad (4.2.3)$$

where g_{int}^{x}, g_{int}^{y}, and g_{int}^{z} are the internal gradient amplitude due to the susceptibility difference ($\Delta\chi$) along x,y, and z directions. B_0 is the main magnetic field perpendicular to the capillary axis and a and b are corresponding to the inner and outer radius of the capillary as shown in **Figure 4.2.1 (A)**. The strength of internal magnetic field with following parameters was shown in **Figure 4.2.1 (B)**: B_0 = 4.7 T, χ_{tube} = -10.66×10^{-6}, χ_{water} = -9.06×10^{-6}, a = 0.575mm, and b = 0.775mm. The strong gradient along x and y directions was driven near the outside of capillary with opposite signs across the capillary and exponentially decayed. Because susceptibility-induced internal gradient doesn't exist along z direction, a strong anisotropy is investigated, which will be the fundamental contrast for detecting the orientation of the capillary.

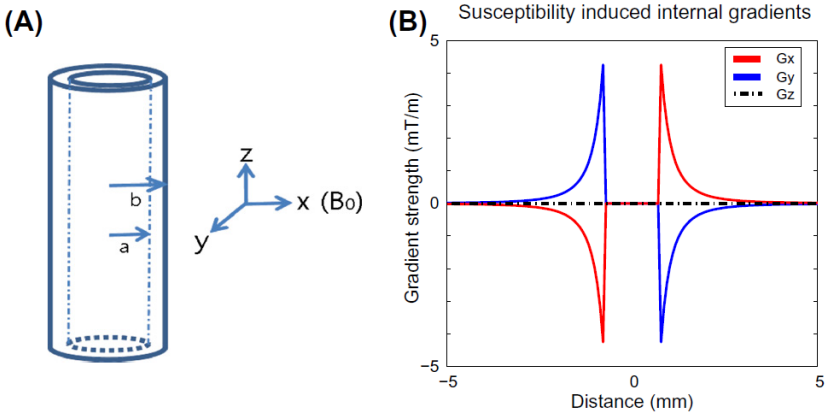

Figure 4.2.1 (A) The capillary tube model. **(B)** The susceptibility induced gradient strength calculation from the capillary model along x, y, and z directions.

The positions of all capillaries were obtained, and the contribution of magnetic field and internal gradient from each capillary was calculated and summed up for all capillaries to investigate the relation between the position and internal gradient in randomly packed capillaries. This methodology was presented in [140-142] and briefly given in here. The boundary between glass and water was assigned magnetic charge density value, i.e. $\rho_m \propto s \cdot x$, where s is the local surface and x is the applied field direction. The total susceptibility-induced magnetic field was calculated as following,

$$\vec{B}_x^{int}(\vec{r}) \backsimeq B_0 \frac{\mu_0}{4\pi} \Delta\chi \int \frac{\vec{r}-\vec{r'}}{\left|\vec{r}-\vec{r'}\right|^3} (s \cdot x) dS' \qquad (4.2.4)$$

Firstly, a binary representation of cylinders was created from the measured spin density image with the matrix size of 1024×1024 at t_d = 50ms to obtain a high resolution of the capillary model. Secondly, the susceptibility-induced magnetic field with an applied external field direction was calculated by the superposition of the dipole field of the glass as a point source [141-142]. Third, the angle resolved gradients were estimated on the image and the distribution of the angle resolved gradients was acquired along each direction.

The internal gradient distribution became complex and heterogeneous depending on the local packing structure in randomly packed capillary model [143] as shown in **Figure 4.2.2 (A)-(D)**. **Figure 4.2.2 (A) to (D)** showed the internal gradient and its histogram along the [1 0 0], [0 1 0], [1 0 1], and [0 1 1] directions, respectively. Broader distribu1tion was observed along the [1 0 0] and [0 0 1] directions compared to those along [1 0 1] and [0 1 1] directions. The width distribution of the angle-resolved gradient along an arbitrary direction for the randomly packed capillary model was shown in **Figure 4.2.2 (E)**. The oblate shape was converged to zero along z direction because $\mathbf{g}_{int} \cdot z$ is zero. The width distribution of the angle-resolved gradient when the capillaries were rotated 20° along x direction was shown in **Figure 4.2.2 (F)**.

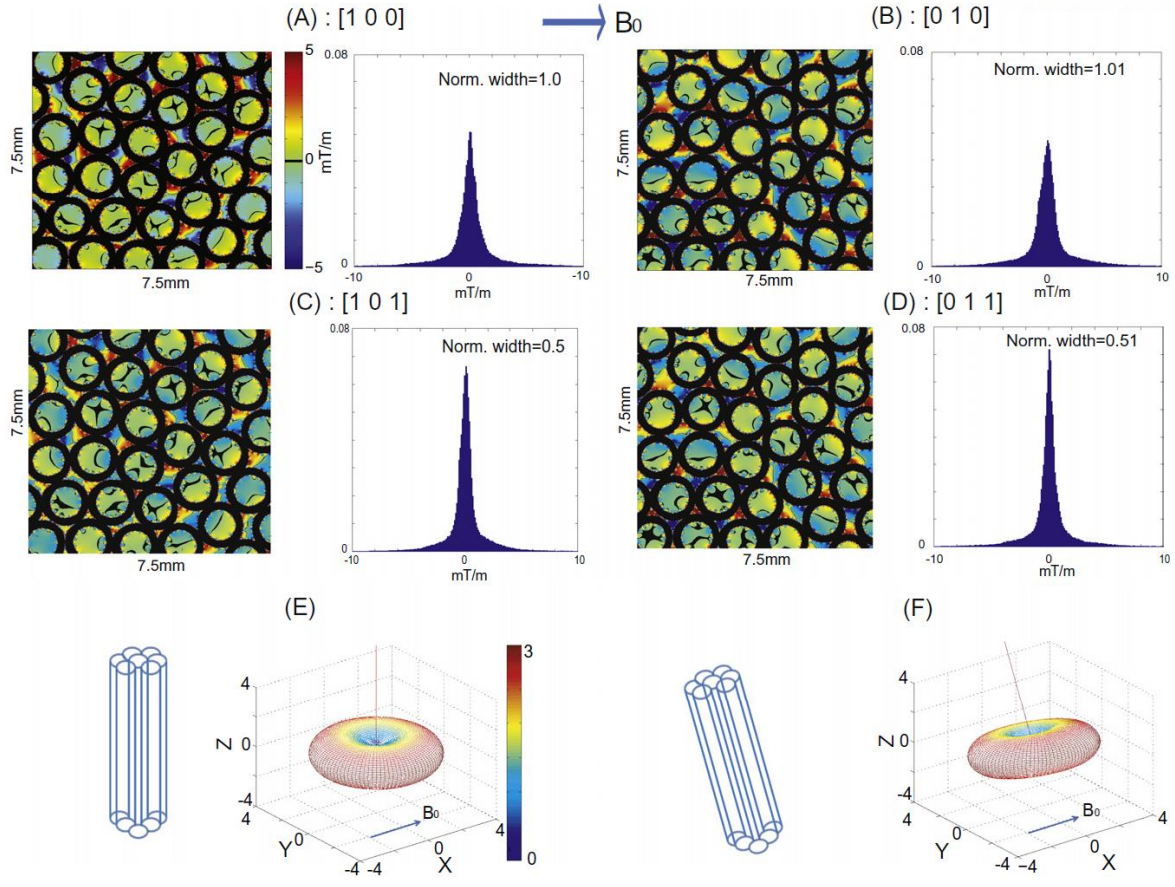

Figure 4.2.2 (A)-(D) The components of internal gradient and its histogram along [1 0 0], [0 1 0], [1 0 1], and [0 1 1] directions. **(E)** The width distribution of angle-resolved along an arbitrary direction for randomly packed capillary model. **(F)** The corresponding distribution when the capillaries are rotated 20° along *x* direction.

The ellipsoidal shape of the width distribution of the angle-resolved gradient reflects the alignment of capillaries along the orientation of the minimum width. For defining an ellipsoidal shape, six parameters are needed, and three eigenvectors are perpendicular to each other and three corresponding eigenvalues determine the lengths of eigenvectors. For this reason, six measurements of the width distribution from different directions would be sufficient to detect the ellipsoid width, whose eigenvectors and eigenvalues describe the directions and the lengths of the ellipsoid. Then, the eigenvector with minimum eigenvalue would be equivalent to the orientation of capillaries.
First, a symmetric matrix *W* was defined as following,

$$W = \begin{bmatrix} W_{xx} & W_{xy} & W_{xz} \\ W_{yx} & W_{yy} & W_{yz} \\ W_{zx} & W_{zy} & W_{zz} \end{bmatrix} \qquad (4.2.5)$$

Internal gradient width W is a symmetric, so $W_{ij} = W_{ji}$. The off diagonal components are zero when the ellipsoid is aligned in Cartesian coordinates. On the other hand, the off diagonal components are non-zero when the ellipsoid is not aligned and diagonalization is needed to obtain three eigenvectors and eigenvalues.

Corresponding to conventional DTI method of acquiring diffusion tensors, width distribution tensors W are determined with six measurements from different directions using the following equation,

$$n^T \cdot W \cdot n = var(H_n) \qquad (4.2.6)$$

where n is the unit vector along the measured distribution, H_n is the distribution along n, and var (H_n) is the variance of the distribution. The six different directions are [1 1 0], [-1 1 0], [0 1 -1], [0 -1 -1], [1 0 -1], and [-1 0 -1]. After acquiring W, A matrix diagonalization was performed to determine the orientation of the capillaries by choosing the minimum eigenvalue's eigenvector. **Figure 4.2.3** shows the determinations of the direction of the cylindrical axis at ellipsoidal angles using W tensor approach with calculated internal gradient of randomly packed capillaries. **Figure 4.2.3 (A)** compares the direction of the cylindrical axis and the direction of minimum eigenvector of W, which is in a good agreement for both the rotation of cylindrical pack along the x, and y directions. And **Figure 4.2.3 (B)** shows the maximum eigenvalues with varying the degree of rotation along x and y directions, respectively. In case of y rotation, the magnitude of internal gradient is decreased as the strength of B_0 is decreased. Even the maximum eigenvalue is decreased and finally disappeared when it perfectly aligned with B_0, the minimum width of the internal gradient still follows the cylindrical axis.

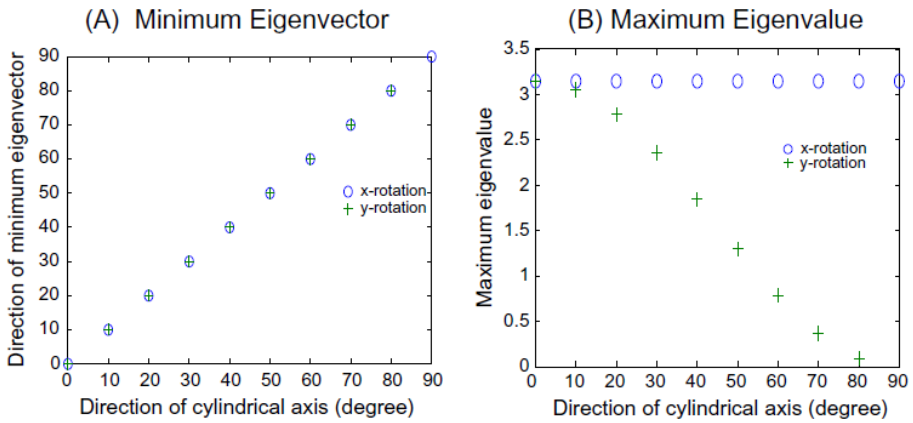

Figure 4.2.3 (A) The direction of cylindrical axis and the direction of minimum eigenvector along x and y rotations. **(B)** The change of maximum eigenvalue for x and y rotations.

The internal gradient is able to be uniquely determined in experiments using the pulsed gradient stimulated sequence. A stimulated echo based spin warp imaging sequence was applied ($\pi/2 - t_e - \pi/2 - t_d - \pi/2 - t_e -$ echo) [144]. This imaging sequence modulates the spin magnetization with internal gradients during the encoding time (t_e) and measures the decay of the magnetization corresponding to the diffusion time (t_d). The decay of the stimulated echo was measured at various diffusion times and the decay rates were measured using the following equation,

$$\frac{1}{T_{eff}} = \frac{1}{T_b} + \gamma^2 t_e^2 D g_{int}^2 \qquad (4.2.7)$$

where $1/T_b$, γ, t_e, and D are the background decay rates, he gyromagnetic ratio, the encoding time, and the diffusion constant.

Previously, we showed that the squared magnitude of internal gradients with this sequence was in a good agreement with the theoretically derived internal gradients. On the other hand, orientation information is not able to obtain using this sequence because only the squared magnitude is measured. To acquire the orientation information with the internal gradient, an external field gradient ($\mathbf{g}_{ext}$) was applied during the encoding time to create the cross-term between the external and internal gradients ($\mathbf{g}_{int} \cdot \mathbf{g}_{ext}$). This cross-term is generated by the following equation,

$$\boldsymbol{g}_{total} = \boldsymbol{g}_{int} + \boldsymbol{g}_{ext} \qquad (4.2.8)$$

$$\frac{1}{T_{eff}} = \frac{1}{T_b} + \gamma^2 t_e^2 D \boldsymbol{g}_{total}^2 \qquad (4.2.9)$$

$$\boldsymbol{g}_{total}^2 = \boldsymbol{g}_{int}^2 + \boldsymbol{g}_{ext}^2 + 2\boldsymbol{g}_{int} \cdot \boldsymbol{g}_{ext} \qquad (4.2.10)$$

The orientation information of internal gradient can be acquired, and the width of the internal gradient along any direction is also able to be measured as the orientation and the magnitude of external gradient are controlled. The randomly packed glass capillary sample with an inner diameter of 1.15mm and a wall thickness of 0.2mm filled with distilled water was prepared. Capillaries were packed into the plastic holder as shown in **Figure 4.2.4 (F)**. This sample was scanned with Bruker system (Bruker Biospin, Billerica, MA) using a commercial birdcage. The susceptibility difference between the glass capillary and distilled water generates the internal gradient around 4mT/m near the surface area for each capillary.

4.2.3 Results

Initially, the numerical calculations were compared to the experimental measurements of the internal gradient using pulsed gradient stimulated echo sequence. The measured decay rate was 2.9/s, which is from diffusion inside the internal gradient for the image voxel close to the surface. The measured decay rate was converted to the strength of internal gradient by using equation **(4.2.7)**, and it was 3.8mT/m with the parameters as t_e = 40ms, $D = 1.8\times10^{-5}$ cm^2/s. The measured internal gradient from experiment was similar to that from theoretical calculation as shown in **Figure 4.2.4 (D)** and **(E)**. And, decay rates for three directions of [1 0 0], [1 0 1], and [0 0 1] were measured, and cross-term ($\mathbf{g}_{int}\cdot\mathbf{g}_{ext}$) were shown in **Figure 4.2.4 (A) – (C)**. The external gradient strength was 5mT/m and the encoding time was 30ms. After that, the diffusion constants were measured, and those from different directions were identical. The diffusion time was varied from 50 to 500ms, and measured decay rates as a function of the diffusion time were extracted by exponential fitting. Decay rates were subtracted from reference experiments ($\mathbf{g}_{ext}$ = 0) so that only cross-term can be extracted. The intensities of the measured internal gradient strength were compared for three different directions as shown in **Figure 4.2.4 (D)** and **(E)**. The internal gradient strength was strongest in case of the [1 0 0] direction. The histogram of internal gradient distribution along *x*, and *z* directions was shown in **Figure 4.2.4 (F)**, and narrower distribution along *z* direction compared to that along x direction were observed as expected.

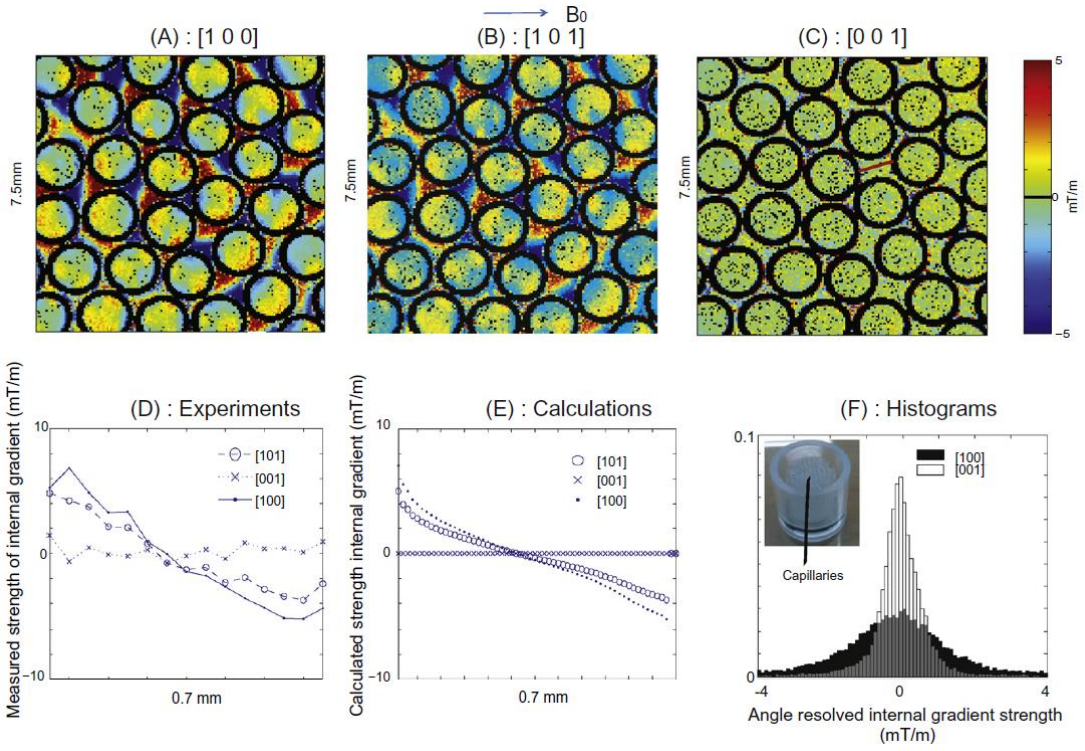

Figure 4.2.4 (A) - (C) represent the experimental results of the strength of cross-term ($\mathbf{g}_{int}\cdot\mathbf{g}_{ext}$) for three different directions. **(D)** and **(E)** are the intensities of measured and calculated internal gradient strength for three different rotations. **(F)** Histograms of internal gradient distribution along *x* and *z* directions.

The measurements with same configurations above were performed for six different directions of [1 1 0], [-1 1 0], [0 1 -1], [0 -1 -1], [1 0 -1], and [-1 0 -1]. From these results, the width tensor *W* was obtained and matrix diagonalization was performed to find minimum eigenvalue's eigenvector. A comparison between three eigenvectors from the measurements as dotted lines and principal axes was shown in **Figure 4.2.5 (A)**. The orientation of minimum eigenvalue's eigenvector followed the orientation of the cylindrical axis.

Two additional experiments were performed to validate this method in oblique angle case. Firstly, the randomly packed capillary sample was rotated 20° along *y* axis maintaining the magnetic field along *x* direction. And the measurements with reference experiments for six different directions were performed to calculate the minimum eigenvalue. The eigenvector with minimum eigenvalue was calculated as 18.2°. These results and expected direction as dotted and solid lines (3) were depicted in **Figure 4.2.5 (B)**. Secondly, the randomly packed capillary sample was rotated 20° along *x* axis and the sample experiments were conducted. The eigenvector with minimum eigenvalue was calculated as 11.2°. These results and expected direction as dotted and solid lines (2) were depicted in **Figure 4.2.5 (B)**.

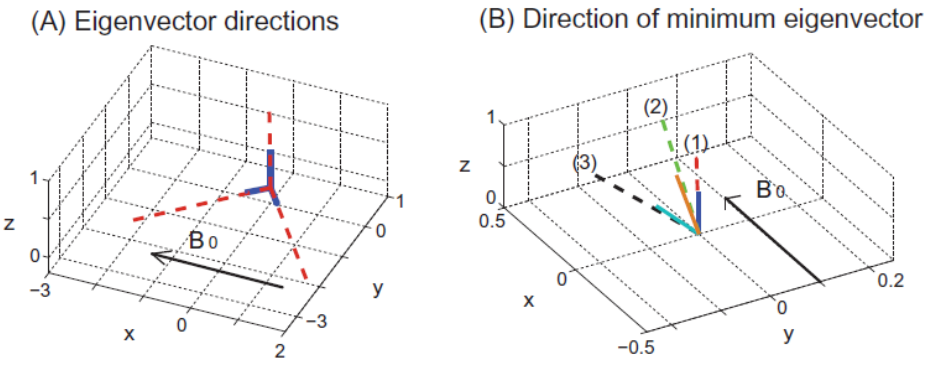

Figure 4.2.5 (A) Dotted lines and solid lines show the principal axis and measured eigenvectors. **(B)** Comparison of the expected direction (solid lines) with measured minimum eigenvalues (dotted lines) at oblique angles. (0°, 10°, and 20° are labeled as (1), (2), and (3))

The measurements with same configurations above were performed for six different directions of [1 1 0], [-1 1 0], [0 1 -1], [0 -1 -1], [1 0 -1], and [-1 0 -1]. From these results, the width tensor *W* was obtained and matrix diagonalization was performed to find minimum eigenvalue's eigenvector. A comparison between three eigenvectors from the measurements as dotted lines and principal axes was shown in **Figure 4.2.5 (A)**. The orientation of minimum eigenvalue's eigenvector followed the orientation of the cylindrical axis. To consider the situation when the spatial resolution is not sufficient to resolve the pore structure so that only distribution information of internal gradients can be acquired is worthwhile. This situation is particularly important for *in vivo* applications. The variation of internal gradients exists in a single voxel, and the measured signal intensity is formed as a weighted exponential function as following,

$$S = \sum_i f(g_i) e^{-t_d/T_{eff}} \qquad (4.2.11)$$

where $f(g_i)$ and T_{eff} are the weight and total decay rates with corresponding internal gradients. The weight was estimated from calculated internal gradient distribution and 1/ T_{eff} was calculated by theoretical approach. **Figure 4.2.6 (A)** showed the signal S as a function of t_d and external gradients along *x*, *y*, and *z* directions. Non-exponential decay was shown along *x* and *y* axes whose internal gradient distribution was broad. However, the mono-exponential decay was observed along *z* axis. Figure 4.2.6 (B) showed the measured magnetization decays along *x*, *y*, and *z* axes, which shows identical relation with theoretical values. Inverse Laplace transform can be used to obtain the direction of the minimum eigenvalue. On the other hand, the degree of deviation from single exponential shape would be utilized to characterize the width of the internal gradient distribution.

The total signals at various diffusion times were plotted for corresponding diffusion time points for six different directions to confirm the sensitivity of the proposed tractography as shown in **Figure 4.2.6 (C)**. The deviation from single exponential decay curve was shown in [1 1 0], and [-1 1 0] directions. On the other hand, less deviation was shown in directions containing *z* component of external gradient. The deviation from the single exponential decay curve was measured for six different directions by dividing the corresponding data with single exponential decay curve to detect the direction of cylinder. The direction of the minimum eigenvalue was observed to fall 2° of the deviation from the *z* direction. Finally, nine different directions of [1 1 0], [-1 1 0], [0 1 -1], [0 -1 -1], [1 0 -1], [-1 0 -1], [1 0 0], [0 1 0], and [0 0 -1] were selected and corresponding widths were measured theoretically and experimentally to validate the angular dependence of eigenvector determination. **Figure 4.2.6 (D)** showed the theoretical and experimental deviation errors, which is determined by the width measurements from six of 51 combinations of directions.

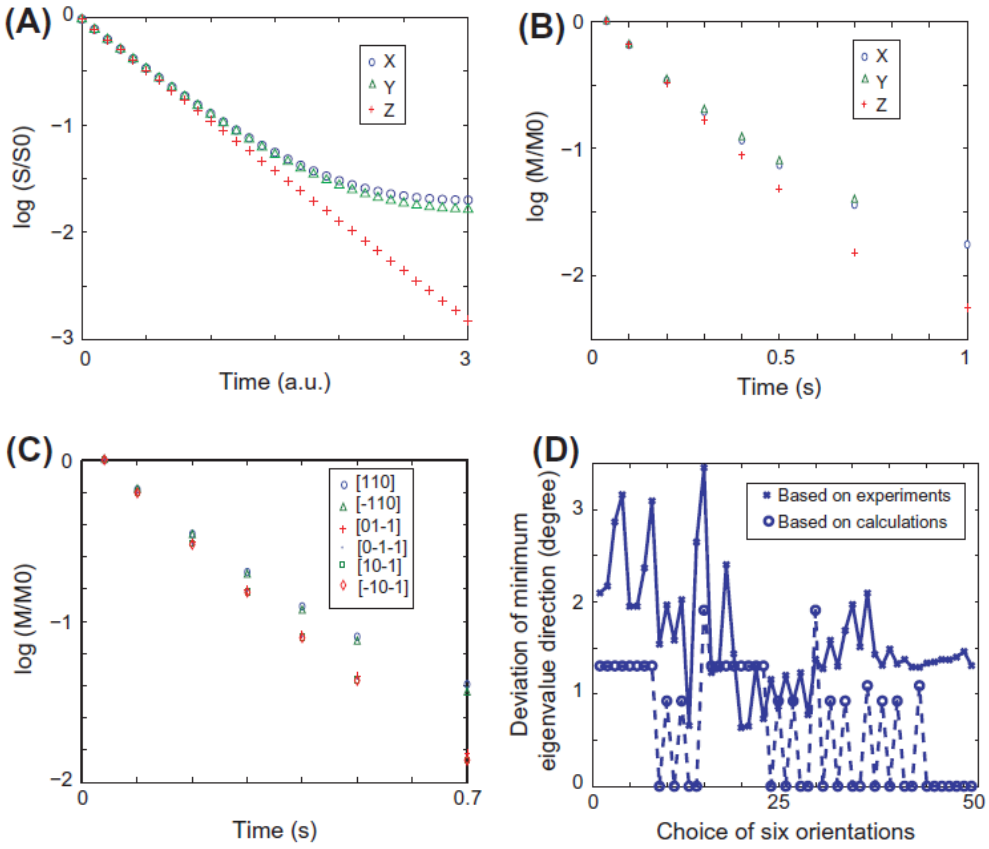

Figure 4.2.6 (A) Signal S as a function of t_d with external gradient along *x*, *y*, and *z* directions. **(B)** The experimental decay when external gradient is applied along *x*, *y*, and *z* directions. **(C)** The experimental decay when external gradient for six different directions was applied. **(D)** Deviation angle error of the minimum eigenvalue direction from the expected direction.

4.2.4 Discussion and conclusions

We theoretically and experimentally demonstrated the feasibility of magnetic field anisotropy based tractography in a randomly packed capillary model without re-orientation of the subject. A distinct angular dependence with respect to the internal gradient distribution was observed when the direction of the main magnetic field was not corresponding to the direction of cylindrical axis. The widths of internal gradient distribution for six different directions were used to extract the minimum width eigenvalue and eigenvector. The direction of the minimum width eigenvalue was shown to follow the expected direction of cylindrical axis, which demonstrates the feasibility of the developed method as an alternative way of tractography. And the sensitivity of this contrast was also verified.

The proposed tractography in this work implicated two important points. Firstly, magnetic field anisotropy induced approach would be sensitive to the fiber orientation. However, the utilization of conventional DTI would not be possible in case that there are small angular variations for large vessels or severe susceptibility induced interference at higher magnetic field. Therefore, the developed method would be a good complement to conventional DTI. Secondly, susceptibility tensor imaging for providing new structural contrast has developed recently [129-130], but it may not be practical due to the need of re-orientation of the subject. The developed method does not need re-orientation of the subject by utilizing the angular variations by interference of internal and external gradients. Therefore, the developed method would offer a practical possibility to obtain anisotropy information without re-orientation of the subject, even when ADC variations are small.

Chapter 5. Concluding remarks

The importance of quantification of microvasculature using MRI methods, and certain limitations in the current methods were explained in Abstract. My thesis research throughout combined Master-Doctoral course was focused on overcoming these limitations by developing new pulse sequences or novel methodologies.

First, in Chapter 3, I applied compressed sensing algorithm to conventional fast imaging sequences, such as FLASH, TSE, and MMME. In CS-FLASH study, improved spatial and temporal resolution for *in vivo* DCE – MRI was shown by implementing CS-FLASH sequence with systematic optimization process. As the FLASH sequence is well accepted for preclinical and clinical investigations, CS-FLASH has a great potential to directly assist investigations of tumor microenvironment with improved temporal or spatial resolution. In CS-TSE study, calibration-free estimation of Gd-concentration was demonstrated with increased temporal resolution without compromising slice coverage, and further improved contrast enhancements by replacing T_2^* to T_2. CS-TSE showed the realistic T_1-weighted DCE – MRI study avoiding inevitable transverse relaxation artifact otherwise, which may provide more accurate and sensitive quantitative perfusion biomarkers. In CS-MMME study, 3D T_1-weighted spin echo based imaging by combining CS with MMME with the total acceleration factor as 128~256 was achieved. CS-MMME showed improved contrast enhancement with minimized susceptibility artifact. Even CS-MMME did not reach the temporal resolution necessary to DCE – MRI including arterial input function yet, it has sufficient potential to acquire ultrafast 3D DCE – MRI with further optimization process.

Second, in Chapter 4, I developed alternative methods to acquire microvasculature information such as cerebral blood volume, vessel size index, and vessel orientation. In SPION based study, total CBV measurements from ΔR_1 and mVSI from UTE-based CBV/ΔR_2 were introduced and proved by both simulation and experiment. Developed methodology showed the potential to enable clear quantification of vascular parameters in longitudinal studies of microvascular brain disease by minimizing susceptibility artifacts and environmental dependency. In MR tractography study, utilization of the angular variations by interference of internal and external gradients without re-orientation of the subject was investigated. The developed method would offer a practical possibility to obtain anisotropy information without re-orientation of the subject. Even the vessel orientation was not directly studied using this tractography technology, it gives the possibility to measure vessel orientation using this method without rotating the subject and may find useful applications for *in vivo* studies with further investigations.

References

[1] HAASE, A., FRAHM, J., MATTHAEI, D., H NICKE, W. & MERBOLDT, K.-D. 2011. FLASH imaging: rapid NMR imaging using low flip-angle pulses. *Journal of Magnetic Resonance,* 213**,** 533-541.

[2] HENNIG, J., NAUERTH, A. & FRIEDBURG, H. 1986. RARE imaging: a fast imaging method for clinical MR. *Magnetic Resonance in Medicine,* 3**,** 823-833.

[3] CHO, H., CHAVEZ, L., SIGMUND, E., MADIO, D. & SONG, Y.-Q. 2006. Fast imaging with the MMME sequence. *Journal of Magnetic Resonance,* 180**,** 18-28.

[4] TAUBMAN, D. & MARCELLIN, M. 2012. *JPEG2000 Image Compression Fundamentals, Standards and Practice: Image Compression Fundamentals, Standards and Practice*, Springer Science & Business Media.

[5] BUCH, G., BURKERT, F., HAGENAUER, J. & KUKLA, B. To compress or not to compress? Global Telecommunications Conference, 1996. GLOBECOM'96.'Communications: The Key to Global Prosperity, 1996. IEEE, 198-203.

[6] STRINTZIS, M. G. 1998. A review of compression methods for medical images in PACS. *International journal of medical informatics,* 52**,** 159-165.

[7] CHRONIK, B. A. & RUTT, B. K. 2001. Simple linear formulation for magnetostimulation specific to MRI gradient coils. *Magnetic resonance in medicine,* 45**,** 916-919.

[8] PRUESSMANN, K. P., WEIGER, M., SCHEIDEGGER, M. B. & BOESIGER, P. 1999. SENSE: sensitivity encoding for fast MRI. *Magnetic resonance in medicine,* 42**,** 952-962.

[9] SODICKSON, D. K. & MANNING, W. J. 1997. Simultaneous acquisition of spatial harmonics (SMASH): fast imaging with radiofrequency coil arrays. *Magnetic Resonance in Medicine,* 38**,** 591-603.

[10] DONOHO, D. L. 2006. For most large underdetermined systems of linear equations the minimal *Communications on pure and applied mathematics,* 59**,** 797-829.

[11] JACKSON, A., BUCKLEY, D. L., PARKER, G. J. & AH-SEE, M. 2005. *Dynamic contrast-enhanced magnetic resonance imaging in oncology*, Springer.

[12] TOFTS, P. S. & KERMODE, A. G. 1991. Measurement of the blood? brain barrier permeability and leakage space using dynamic MR imaging. 1. Fundamental concepts. *Magnetic Resonance in Medicine,* 17**,** 357-367.

[13] BARRETT, T., BRECHBIEL, M., BERNARDO, M. & CHOYKE, P. L. 2007. MRI of tumor angiogenesis. *Journal of magnetic resonance imaging,* 26**,** 235-249.

[14] EGELAND, T. A., GAUSTAD, J. V., VESTVIK, I. K., BENJAMINSEN, I. C., MATHIESEN, B. & ROFSTAD, E. K. 2006. Assessment of fraction of radiobiologically hypoxic cells in human melanoma xenografts by dynamic contrast-enhanced MRI. *Magnetic resonance in medicine,* 55**,** 874-

882.

[15] HYLTON, N. 2006. Dynamic contrast-enhanced magnetic resonance imaging as an imaging biomarker. *Journal of clinical oncology,* 24**,** 3293-3298.

[16] PADHANI, A. R. 2002. Dynamic contrast-enhanced MRI in clinical oncology: Current status and future directions. *Journal of Magnetic Resonance Imaging,* 16**,** 407-422.

[17] YANKEELOV, T. E. & GORE, J. C. 2009. Dynamic contrast enhanced magnetic resonance imaging in oncology: theory, data acquisition, analysis, and examples. *Current medical imaging reviews,* 3**,** 91.

[18] CHO, H., ACKERSTAFF, E., CARLIN, S., LUPU, M. E., WANG, Y., RIZWAN, A., O'DONOGHUE, J., LING, C. C., HUMM, J. L. & ZANZONICO, P. B. 2009. Noninvasive multimodality imaging of the tumor microenvironment: registered dynamic magnetic resonance imaging and positron emission tomography studies of a preclinical tumor model of tumor hypoxia. *Neoplasia,* 11**,** 247-IN3.

[19] HOFFMANN, U., BRIX, G., KNOPP, M. V., HEB, T. & LORENZ, W. J. 1995. Pharmacokinetic mapping of the breast: a new method for dynamic MR mammography. *Magnetic resonance in medicine,* 33**,** 506-514.

[20] TOFTS, P. S., BRIX, G., BUCKLEY, D. L., EVELHOCH, J. L., HENDERSON, E., KNOPP, M. V., LARSSON, H. B., LEE, T.-Y., MAYR, N. A. & PARKER, G. J. 1999. Estimating kinetic parameters from dynamic contrast-enhanced T 1-weighted MRI of a diffusable tracer: standardized quantities and symbols. *Journal of Magnetic Resonance Imaging,* 10**,** 223-232.

[21] HEISEN, M., FAN, X., BUURMAN, J., VAN RIEL, N. A., KARCZMAR, G. S. & TER HAAR ROMENY, B. M. 2010. The influence of temporal resolution in determining pharmacokinetic parameters from DCE-MRI data. *Magnetic Resonance in Medicine,* 63**,** 811-816.

[22] CAND S, E. J., ROMBERG, J. & TAO, T. 2006. Robust uncertainty principles: Exact signal reconstruction from highly incomplete frequency information. *Information Theory, IEEE Transactions on,* 52**,** 489-509.

[23] DONOHO, D. L. 2006. Compressed sensing. *Information Theory, IEEE Transactions on,* 52**,** 1289-1306.

[24] LUSTIG, M., SANTOS, J. M., DONOHO, D. L. & PAULY, J. M. kt SPARSE: High frame rate dynamic MRI exploiting spatio-temporal sparsity. Proceedings of the 13th Annual Meeting of ISMRM, Seattle, 2006.

[25] LUSTIG, M., DONOHO, D. & PAULY, J. M. 2007. Sparse MRI: The application of compressed sensing for rapid MR imaging. *Magnetic resonance in medicine,* 58**,** 1182-1195.

[26] LUSTIG, M., DONOHO, D. L., SANTOS, J. M. & PAULY, J. M. 2008. Compressed sensing MRI. *Signal Processing Magazine, IEEE,* 25**,** 72-82.

[27] ROMBERG, J. 2008. Imaging via compressive sampling [introduction to compressive sampling and recovery via convex programming]. *IEEE Signal Processing Magazine,* 25**,** 14-20.

[28] ADLURU, G., TASDIZEN, T., SCHABEL, M. C. & DIBELLA, E. V. 2010. Reconstruction of 3D dynamic contrast-enhanced magnetic resonance imaging using nonlocal means. *Journal of Magnetic Resonance Imaging,* 32**,** 1217-1227.

[29] BILGIN, A., TROUARD, T., ALTBACH, M. & RAGHUNAND, N. Three dimensional compressed sensing for dynamic MRI. Proceedings of the 16th ISMRM Scientific Meeting & Exhibition, 2008. 337.

[30] CHEN, L., SCHABEL, M. C. & DIBELLA, E. V. 2010. Reconstruction of dynamic contrast enhanced magnetic resonance imaging of the breast with temporal constraints. *Magnetic resonance imaging,* 28**,** 637-645.

[31] JI, J. & LANG, T. Dynamic MRI with compressed sensing imaging using temporal correlations. Biomedical Imaging: From Nano to Macro, 2008. ISBI 2008. 5th IEEE International Symposium on, 2008. IEEE, 1613-1616.

[32] KUHL, C. K., SCHILD, H. H. & MORAKKABATI, N. 2005. Dynamic Bilateral Contrast-enhanced MR Imaging of the Breast: Trade-off between Spatial and Temporal Resolution 1. *Radiology,* 236**,** 789-800.

[33] SCHNALL, M. D. & IKEDA, D. M. 1999. Lesion diagnosis working group report. *Journal of Magnetic Resonance Imaging,* 10**,** 982-990.

[34] SMITH, D. S., WELCH, E. B., LI, X., ARLINGHAUS, L. R., LOVELESS, M. E., KOYAMA, T., GORE, J. C. & YANKEELOV, T. E. 2011. Quantitative effects of using compressed sensing in dynamic contrast enhanced MRI. *Physics in medicine and biology,* 56**,** 4933.

[35] WANG, H., MIAO, Y., ZHOU, K., YU, Y., BAO, S., HE, Q., DAI, Y., XUAN, S. Y., TARABISHY, B. & YE, Y. 2010. Feasibility of high temporal resolution breast DCE-MRI using compressed sensing theory. *Medical physics,* 37**,** 4971-4981.

[36] JUNG, H., SUNG, K., NAYAK, K. S., KIM, E. Y. & YE, J. C. 2009. k-t FOCUSS: A general compressed sensing framework for high resolution dynamic MRI. *Magnetic Resonance in Medicine,* 61**,** 103-116.

[37] VAN DEN BERG, E. & FRIEDLANDER, M. P. 2008. Probing the Pareto frontier for basis pursuit solutions. *SIAM Journal on Scientific Computing,* 31**,** 890-912.

[38] DONOHO, D. L., STODDEN, V. C. & TSAIG, Y. 2007. About sparselab.

[39] LAISSY, J.-P., FARAGGI, M., LEBTAHI, R., SOYER, P., BRILLET, G., M RY, J.-P., MENU, Y. & LE GULUDEC, D. 1994. Functional evaluation of normal and ischemic kidney by means of gadolinium-DOTA enhanced TurboFLASH MR imaging: A preliminary comparison with< sup> 99m</sup> Tc-MAG3 dynamic scintigraphy. *Magnetic resonance imaging,* 12**,** 413-419.

[40] YAMASHITA, Y., MIYAZAKI, T., HATANAKA, Y. & TAKAHASHI, M. 1995. Dynamic MRI of small renal cell carcinoma. *Journal of computer assisted tomography,* 19**,** 759-765.

[41] HAASE, A. 1990. Snapshot flash mri. applications to t1, t2, and chemical-shift imaging. *Magnetic Resonance in Medicine,* 13**,** 77-89.

[42] MATERNE, R., SMITH, A., PEETERS, F., DEHOUX, J.-P., KEYEUX, A., HORSMANS, Y. & VAN BEERS, B. 2002. Assessment of hepatic perfusion parameters with dynamic MRI. *Magnetic resonance in medicine,* 47**,** 135-142.

[43] PARKER, G. J., SUCKLING, J., TANNER, S. F., PADHANI, A. R., REVELL, P. B., HUSBAND, J. E. & LEACH, M. O. 1997. Probing tumor microvascularity by measurement, analysis and display of contrast agent uptake kinetics. *Journal of Magnetic Resonance Imaging,* 7**,** 564-574.

[44] VALL E, J. P., SOSTMAN, H. D., MACFALL, J. R., WHEELER, T., HEDLUND, L. W., SPRITZER, C. E. & COLEMAN, R. E. 1997. MRI quantitative myocardial perfusion with compartmental analysis: a rest and stress study. *Magnetic resonance in medicine,* 38**,** 981-989.

[45] KLEPPEST , M., LARSSON, C., GROOTE, I., SALO, R., VARDAL, J., COURIVAUD, F. & BJ RNERUD, A. 2014. T2*-correction in dynamic contrast-enhanced MRI from double-echo acquisitions. *Journal of Magnetic Resonance Imaging,* 39**,** 1314-1319.

[46] PORT, R. E., KNOPP, M. V. & BRIX, G. 2001. Dynamic contrast-enhanced MRI using Gd-DTPA: Interindividual variability of the arterial input function and consequences for the assessment of kinetics in tumors. *Magnetic resonance in medicine,* 45**,** 1030-1038.

[47] YANKEELOV, T. E., ROONEY, W. D., LI, X. & SPRINGER, C. S. 2003. Variation of the relaxographic "shutter-speed" for transcytolemmal water exchange affects the CR bolus-tracking curve shape. *Magnetic resonance in medicine,* 50**,** 1151-1169.

[48] MAKOWSKI, M., JANSEN, C., WEBB, I., CHIRIBIRI, A., NAGEL, E., BOTNAR, R., KOZERKE, S. & PLEIN, S. 2010. First-pass contrast-enhanced myocardial perfusion MRI in mice on a 3-T clinical MR scanner. *Magnetic Resonance in Medicine,* 64**,** 1592-1598.

[49] PAULSEN, J., BAJAJ, V. S. & PINES, A. 2010. Compressed sensing of remotely detected MRI velocimetry in microfluidics. *Journal of Magnetic Resonance,* 205**,** 196-201.

[50] LAWRENCE, I. & LIN, K. 1989. A concordance correlation coefficient to evaluate reproducibility. *Biometrics***,** 255-268.

[51] LANDIS, C. S., LI, X., TELANG, F. W., CODERRE, J. A., MICCA, P. L., ROONEY, W. D., LATOUR, L. L., V TEK, G., P LYKA, I. & SPRINGER, C. S. 2000. Determination of the MRI contrast agent concentration time course in vivo following bolus injection: effect of equilibrium transcytolemmal water exchange. *Magnetic resonance in medicine,* 44**,** 563-574.

[52] RAABE, B. M., ARTWOHL, J. E., PURCELL, J. E., LOVAGLIO, J. & FORTMAN, J. D. 2011. Effects of weekly blood collection in C57BL/6 mice. *Journal of the American Association for*

Laboratory Animal Science: JAALAS, 50**,** 680.

[53] ZUR, Y., STOKAR, S. & BENDEL, P. 1988. An analysis of fast imaging sequences with steady-state transverse magnetization refocusing. *Magnetic resonance in medicine,* 6**,** 175-193.

[54] BOMANS, M., H HNE, K.-H., LAUB, G., POMMERT, A. & TIEDE, U. 1991. Improvement of 3D acquisition and visualization in MRI. *Magnetic resonance imaging,* 9**,** 597-609.

[55] BRUNNER, P. & ERNST, R. 1979. Sensitivity and performance time in NMR imaging. *Journal of Magnetic Resonance (1969),* 33**,** 83-106.

[56] CHENG, H. L. M. 2007. T1 measurement of flowing blood and arterial input function determination for quantitative 3D T1-weighted DCE-MRI. *Journal of Magnetic Resonance Imaging,* 25**,** 1073-1078.

[57] IRARRAZABAL, P. & NISHIMURA, D. G. 1995. Fast three dimensional magnetic resonance imaging. *Magnetic resonance in medicine,* 33**,** 656-662.

[58] KARANTANAS, A., PAPANIKOLAOU, N., VASIOU, K. & LAVDAS, E. 1999. Comparison of T 1-weighted spin-echo and 3D T 1-weighted multi-shot echo planar pulse sequences in imaging the brain at IT. *Magnetic resonance imaging,* 17**,** 663-668.

[59] KARANTANAS, A. H., ZIBIS, A. H. & KITSOULIS, P. 2002. Fat-suppressed 3D-T1-weighted-echo planar imaging: comparison with fat-suppressed 3D-T1-weighted-gradient echo in imaging the cartilage of the knee. *Computerized medical imaging and graphics,* 26**,** 159-165.

[60] REINER, C., NEVILLE, A., NAZEER, H., BREAULT, S., DALE, B., MERKLE, E. & BASHIR, M. 2013. Contrast-enhanced free-breathing 3D T1-weighted gradient-echo sequence for hepatobiliary MRI in patients with breath-holding difficulties. *European radiology,* 23**,** 3087-3093.

[61] TOMURA, N., NARITA, K., TAKAHASHI, S., OTANI, T., SAKUMA, I., YASUDA, K., NISHII, T. & WATARAI, J. 2007. Contrast-enhanced multi-shot echo-planar FLAIR in the depiction of metastatic tumors of the brain: comparison with contrast-enhanced spin-echo T1-weighted imaging. *Acta Radiologica,* 48**,** 1032-1037.

[62] MEZRICH, R. 1995. A perspective on K-space. *Radiology,* 195**,** 297-315.

[63] FRAHM, J., HAASE, A. & MATTHAEI, D. 1986. Rapid three-dimensional MR imaging using the FLASH technique. *Journal of computer assisted tomography,* 10**,** 363-368.

[64] MANSFIELD, P. 1977. Multi-planar image formation using NMR spin echoes. *Journal of Physics C: Solid State Physics,* 10**,** L55.

[65] BUCKLEY, D. L. 2002. Uncertainty in the analysis of tracer kinetics using dynamic contrast-enhanced T1-weighted MRI. *Magnetic Resonance in Medicine,* 47**,** 601-606.

[66] TOFTS, P. S. 1997. Modeling tracer kinetics in dynamic Gd-DTPA MR imaging. *Journal of Magnetic Resonance Imaging,* 7**,** 91-101.

[67] ANDERSON, E. A., ISAACMAN, S., PEABODY, D. S., WANG, E. Y., CANARY, J. W. &

KIRSHENBAUM, K. 2006. Viral nanoparticles donning a paramagnetic coat: conjugation of MRI contrast agents to the MS2 capsid. *Nano letters,* 6**,** 1160-1164.

[68] CARAVAN, P. 2006. Strategies for increasing the sensitivity of gadolinium based MRI contrast agents. *Chemical Society Reviews,* 35**,** 512-523.

[69] LIEPOLD, L. O., ABEDIN, M. J., BUCKHOUSE, E. D., FRANK, J. A., YOUNG, M. J. & DOUGLAS, T. 2009. Supramolecular protein cage composite MR contrast agents with extremely efficient relaxivity properties. *Nano letters,* 9**,** 4520-4526.

[70] MIN, J., JUNG, H., SHIN, H.-H., CHO, G., CHO, H. & KANG, S. 2013. Implementation of p22 viral capsids as intravascular magnetic resonance T 1 contrast conjugates via site-selective attachment of Gd (III)-chelating agents. *Biomacromolecules,* 14**,** 2332-2339.

[71] OSHIO, K. & JOLESZ, F. A. 1993. Fast MRI by creating multiple spin echoes in a CPMG sequence. *Magnetic resonance in medicine,* 30**,** 251-254.

[72] COUNSELL, C. 1993. PREVIEW: a new ultrafast imaging sequence requiring minimal gradient switching. *Magnetic resonance imaging,* 11**,** 603-616.

[73] HEID, O., DEIMLING, M. & HUK, W. 1993. QUEST-a quick echo split nmr imaging technique. *Magnetic resonance in medicine,* 29**,** 280-283.

[74] HENNIG, J. & HODAPP, M. 1993. Burst imaging. *Magma,* 1**,** 39-48.

[75] JEREČIĆ, R., BOCK, M. & SCHAD, L. R. 2000. An amplitude optimized single-shot hybrid QUEST technique. *Magnetic resonance imaging,* 18**,** 23-32.

[76] LOWE, I. & WYSONG, R. 1993. DANTE ultrafast imaging sequence (DUFIS). *Journal of Magnetic Resonance, Series B,* 101**,** 106-109.

[77] MADIO, D. P. & LOWE, I. J. 1995. Ultra-fast imaging using low flip angles and fids. *Magnetic resonance in medicine,* 34**,** 525-529.

[78] NELSON, R. J., MAGUIRE, Y., CAPUTO, D. F., LEU, G., KANG, Y., PRAVIA, M., TUCH, D., WEINSTEIN, Y. S. & CORY, D. G. 1998. Counting echoes: Application of a complete reciprocal-space description of NMR spin dynamics. *Concepts in Magnetic Resonance,* 10**,** 331-341.

[79] SODICKSON, A. & CORY, D. G. 1998. A generalized k-space formalism for treating the spatial aspects of a variety of NMR experiments. *Progress in nuclear magnetic resonance spectroscopy,* 33**,** 77-108.

[80] WHEELER-KINGSHOTT, C., THOMAS, D., LYTHGOE, M., GUILFOYLE, D., WILLIAMS, S. & DORAN, S. 2000. Burst excitation for quantitative diffusion imaging with multiple b-values. *Magnetic resonance in medicine,* 44**,** 737-745.

[81] ZHA, L. & LOWE, I. J. 1995. Optimized Ultra-Fast Imaging Sequence (OUFIS). *Magnetic resonance in medicine,* 33**,** 377-395.

[82] ARONEN, H. J., GAZIT, I. E., LOUIS, D. N., BUCHBINDER, B. R., PARDO, F. S.,

WEISSKOFF, R. M., HARSH, G. R., COSGROVE, G., HALPERN, E. F. & HOCHBERG, F. H. 1994. Cerebral blood volume maps of gliomas: comparison with tumor grade and histologic findings. *Radiology,* 191**,** 41-51.

[83] ARONEN, H. J., GLASS, J., PARDO, F., BELLIVEAU, J., GRUBER, M., BUCHBINDER, B., GAZIT, I., LINGGOOD, R., FISCHMAN, A. & ROSEN, B. 1995. Echo-planar MR cerebral blood volume mapping of gliomas: clinical utility. *Acta Radiologica,* 36**,** 520-528.

[84] GIBBS, J., LEENDERS, K., WISE, R. & JONES, T. 1984. Evaluation of cerebral perfusion reserve in patients with carotid-artery occlusion. *The Lancet,* 323**,** 310-314.

[85] HAMBERG, L. M., MACFARLANE, R., TASDEMIROGLU, E., BOCCALINI, P., HUNTER, G. J., BELLIVEAU, J. W., MOSKOWITZ, M. A. & ROSEN, B. R. 1993. Measurement of cerebrovascular changes in cats after transient ischemia using dynamic magnetic resonance imaging. *Stroke,* 24**,** 444-450.

[86] KUCHARCZYK, J., ROBERTS, T., MOSELEY, M. E. & WATSON, A. 1993. Contrast-enhanced perfusion-sensitive MR imaging in the diagnosis of cerebrovascular disorders. *Journal of Magnetic Resonance Imaging,* 3**,** 241-245.

[87] SPETZLER, R., WILSON, C., WEINSTEIN, P., MEHDORN, M., TOWNSEND, J. & TELLES, D. 1977. Normal perfusion pressure breakthrough theory. *Clinical neurosurgery,* 25**,** 651-672.

[88] WARACH, S., LI, W., RONTHAL, M. & EDELMAN, R. R. 1992. Acute cerebral ischemia: evaluation with dynamic contrast-enhanced MR imaging and MR angiography. *Radiology,* 182**,** 41-47.

[89] DENNIE, J., MANDEVILLE, J. B., BOXERMAN, J. L., PACKARD, S. D., ROSEN, B. R. & WEISSKOFF, R. M. 1998. NMR imaging of changes in vascular morphology due to tumor angiogenesis. *Magnetic resonance in medicine,* 40**,** 793-799.

[90] GRUBB, R. L., PHELPS, M. E. & TER-POGOSSIAN, M. M. 1973. Regional cerebral blood volume in humans: x-ray fluorescence studies. *Archives of neurology,* 28**,** 38-44.

[91] RISBERG, J., LUNDBERG, N. & INGVAR, D. H. 1969. Regional cerebral blood volume during acute transient rises of the intracranial pressure (plateau waves). *Journal of neurosurgery,* 31**,** 303.

[92] EICHLING, J. O., RAICHLE, M. E., GRUBB, R., LARSON, K. B. & TER-POGOSSIAN, M. 1975. In vivo determination of cerebral blood volume with radioactive oxygen-15 in the monkey. *Circulation research,* 37**,** 707-714.

[93] LEGGETT, R. & WILLIAMS, L. 1991. Suggested reference values for regional blood volumes in humans. *Health Physics,* 60**,** 139-154.

[94] PHELPS, M., HUANG, S., HOFFMAN, E. & KUHL, D. 1979. Validation of tomographic measurement of cerebral blood volume with C-11-labeled carboxyhemoglobin. *J. Nucl. Med.;(United States),* 20.

[95] POWERS, W. J. & RAICHLE, M. E. 1985. Positron emission tomography and its application to

the study of cerebrovascular disease in man. *Stroke,* 16**,** 361-376.

[96] TOYAMA, H., TAKESHITA, G., TAKEUCHI, A., ANNO, H., EJIRI, K., MAEDA, H., KATADA, K., KOGA, S., ISHIYAMA, N. & KANNO, T. 1990. Cerebral hemodynamics in patients with chronic obstructive carotid disease by rCBF, rCBV, and rCBV/rCBF ratio using SPECT. *Journal of nuclear medicine: official publication, Society of Nuclear Medicine,* 31**,** 55-60.

[97] KUPPUSAMY, K., LIN, W., CIZEK, G. R. & HAACKE, E. M. 1996. In vivo regional cerebral blood volume: quantitative assessment with 3D T1-weighted pre-and postcontrast MR imaging. *Radiology,* 201**,** 106-112.

[98] MOSELEY, M. E., CHEW, W. M., WHITE, D. L., KUCHARCZYK, J., LITT, L., DERUGIN, N., DUPON, J., BRASCH, R. C. & NORMAN, D. 1992. Hypercarbia-induced changes in cerebral blood volume in the cat: A 1H MRI and intravascular contrast agent study. *Magnetic resonance in medicine,* 23**,** 21-30.

[99] SCHWARZBAUER, C., SYHA, J. & HAASE, A. 1993. Quantification of regional blood volumes by rapid T1 mapping. *Magnetic resonance in medicine,* 29**,** 709-712.

[100] WU, E. X., TANG, H. & JENSEN, J. H. 2004. Applications of ultrasmall superparamagnetic iron oxide contrast agents in the MR study of animal models. *NMR in Biomedicine,* 17**,** 478-483.

[101] LOUBEYRE, P., DE JAEGERE, T., BOSMANS, H., MIAO, Y., NI, Y., LANDUYT, W. & MARCHAL, G. 1999. Comparison of iron oxide particles (AMI 227) with a gadolinium complex (Gd-DOTA) in dynamic susceptibility contrast MR imagings (FLASH and EPI) for both phantom and rat brain at 1.5 tesla. *Journal of Magnetic Resonance Imaging,* 9**,** 447-453.

[102] WEISSLEDER, R., ELIZONDO, G., WITTENBERG, J., RABITO, C., BENGELE, H. & JOSEPHSON, L. 1990. Ultrasmall superparamagnetic iron oxide: characterization of a new class of contrast agents for MR imaging. *Radiology,* 175**,** 489-493.

[103] YABLONSKIY, D. A. & HAACKE, E. M. 1994. Theory of NMR signal behavior in magnetically inhomogeneous tissues: the static dephasing regime. *Magnetic Resonance in Medicine,* 32**,** 749-763.

[104] BOXERMAN, J. L., HAMBERG, L. M., ROSEN, B. R. & WEISSKOFF, R. M. 1995. MR contrast due to intravascular magnetic susceptibility perturbations. *Magnetic Resonance in Medicine,* 34**,** 555-566.

[105] TROPRES, I., GRIMAULT, S., VAETH, A., GRILLON, E., JULIEN, C., PAYEN, J. F., LAMALLE, L. & D CORPS, M. 2001. Vessel size imaging. *Magnetic resonance in medicine,* 45**,** 397-408.

[106] KIM, S. G., HAREL, N., JIN, T., KIM, T., LEE, P. & ZHAO, F. 2013. Cerebral blood volume MRI with intravascular superparamagnetic iron oxide nanoparticles. *NMR in Biomedicine,* 26**,** 949-962.

[107] PRINSTER, A., PIERPAOLI, C., TURNER, R. & JEZZARD, P. 1997. Simultaneous measurement of ΔR2 and ΔR2* in cat brain during hypoxia and hypercapnia. *Neuroimage,* 6**,** 191-200.

[108] BEAUMONT, M., LEMASSON, B., FARION, R., SEGEBARTH, C., R MY, C. & BARBIER, E. L. 2009. Characterization of tumor angiogenesis in rat brain using iron-based vessel size index MRI in combination with gadolinium-based dynamic contrast-enhanced MRI. *Journal of Cerebral Blood Flow & Metabolism,* 29**,** 1714-1726.

[109] HUANG, S., KIM, J. K., ATOCHIN, D. N., FARRAR, C. T., HUANG, P. L., SUH, J. Y., KWON, S. J., SHIM, W. H., CHO, H. & CHO, G. 2013. Cerebral blood volume affects blood–brain barrier integrity in an acute transient stroke model. *Journal of Cerebral Blood Flow & Metabolism,* 33**,** 898-905.

[110] KIM, Y., TEJIMA, E., HUANG, S., ATOCHIN, D., DAI, G., LO, E., HUANG, P., BOGDANOV, A. & ROSEN, B. 2008. In vivo quantification of transvascular water exchange during the acute phase of permanent stroke. *Magnetic Resonance in Medicine,* 60**,** 813-821.

[111] GLOVER, G. H., PAULY, J. M. & BRADSHAW, K. M. 1992. Boron-11 imaging with a three-dimensional reconstruction method. *Journal of Magnetic Resonance Imaging,* 2**,** 47-52.

[112] HOLMES, J. E. & BYDDER, G. M. 2005. MR imaging with ultrashort TE (UTE) pulse sequences: basic principles. *Radiography,* 11**,** 163-174.

[113] PAULY, J., CONOLLY, S., NISHIMURA, D. & MACOVSKI, A. Slice-selective excitation for very short T2 species. Proceedings of SMRM, 1989. 28.

[114] ROBSON, M. D., GATEHOUSE, P. D., BYDDER, M. & BYDDER, G. M. 2003. Magnetic resonance: an introduction to ultrashort TE (UTE) imaging. *Journal of computer assisted tomography,* 27**,** 825-846.

[115] JUNG, H., PARK, B., LEE, C., CHO, J., SUH, J., PARK, J., KIM, Y., KIM, J., CHO, G. & CHO, H. 2014. Dual MRI T 1 and T 2 (∗) contrast with size-controlled iron oxide nanoparticles. *Nanomedicine: Nanotechnology, Biology and Medicine,* 10**,** 1679-1689.

[116] PATHAK, A. P., WARD, B. D. & SCHMAINDA, K. M. 2008. A novel technique for modeling susceptibility-based contrast mechanisms for arbitrary microvascular geometries: the finite perturber method. *Neuroimage,* 40**,** 1130-1143.

[117] CHUGH, B. P., LERCH, J. P., LISA, X. Y., PIENKOWSKI, M., HARRISON, R. V., HENKELMAN, R. M. & SLED, J. G. 2009. Measurement of cerebral blood volume in mouse brain regions using micro-computed tomography. *Neuroimage,* 47**,** 1312-1318.

[118] CREMER, J. E. & SEVILLE, M. P. 1983. Regional brain blood flow, blood volume, and haematocrit values in the adult rat. *Journal of Cerebral Blood Flow & Metabolism,* 3**,** 254-256.

[119] EVERETT, N. B., SIMMONS, B. & LASHER, E. P. 1956. Distribution of blood (Fe59) and plasma (I131) volumes of rats determined by liquid nitrogen freezing. *Circulation research,* 4**,** 419-

424.

[120] JULIEN-DOLBEC, C., TROPRES, I., MONTIGON, O., REUTENAUER, H., ZIEGLER, A., DECORPS, M. & PAYEN, J. F. 2002. Regional response of cerebral blood volume to graded hypoxic hypoxia in rat brain. *British journal of anaesthesia,* 89**,** 287-293.

[121] LEAR, J. L., KASLIWAL, R. & FEYERABEND, A. 1990. Mapping regional cerebral vascular transit time by simultaneous determination of local cerebral blood flow and local cerebral blood volume. *Metabolic brain disease,* 5**,** 155-165.

[122] SCHWARZBAUER, C., MORRISSEY, S. P., DEICHMANN, R., HILLENBRAND, C., SYHA, J., ADOLF, H., N TH, U. & HAASE, A. 1997. Quantitative magnetic resonance imaging of capillary water permeability and regional blood volume with an intravascular MR contrast agent. *Magnetic resonance in medicine,* 37**,** 769-777.

[123] WU, E. X., TANG, H., ASAI, T. & DU YAN, S. 2004. Regional cerebral blood volume reduction in transgenic mutant APP (V717F, K670N/M671L) mice. *Neuroscience letters,* 365**,** 223-227.

[124] BASSER, P. J., MATTIELLO, J. & LEBIHAN, D. 1994. Estimation of the effective self-diffusion tensor from the NMR spin echo. *Journal of Magnetic Resonance, Series B,* 103**,** 247-254.

[125] CALLAGHAN, P., GODEFROY, S. & RYLAND, B. 2003. Use of the second dimension in PGSE NMR studies of porous media. *Magnetic resonance imaging,* 21**,** 243-248.

[126] MORI, S., CRAIN, B. J., CHACKO, V. & VAN ZIJL, P. 1999. Three-dimensional tracking of axonal projections in the brain by magnetic resonance imaging. *Annals of neurology,* 45**,** 265-269.

[127] BASSER, P. J. & JONES, D. K. 2002. Diffusion-tensor MRI: theory, experimental design and data analysis–a technical review. *NMR in Biomedicine,* 15**,** 456-467.

[128] MORI, S. & VAN ZIJL, P. C. 2002. Fiber tracking: principles and strategies-a technical review. *NMR in Biomedicine,* 15**,** 468-480.

[129] LIU, C. 2010. Susceptibility tensor imaging. *Magnetic Resonance in Medicine,* 63**,** 1471-1477.

[130] VIGNAUD, A., RODRIGUEZ, I., ENNIS, D. B., DESILVA, R., KELLMAN, P., TAYLOR, J., BENNETT, E. & WEN, H. 2006. Detection of myocardial capillary orientation with intravascular iron-oxide nanoparticles in spin-echo MRI. *Magnetic resonance in medicine,* 55**,** 725-730.

[131] BRINDLE, K. M., BROWN, F. F., CAMPBELL, I. D., GRATHWOHL, C. & KUCHEL, P. 1979. Application of spin-echo nuclear magnetic resonance to whole-cell systems. Membrane transport. *Biochem. J,* 180**,** 37-44.

[132] BROWN, R. J. 1961. Distribution of fields from randomly placed dipoles: free-precession signal decay as result of magnetic grains. *Physical Review,* 121**,** 1379.

[133] ENDRE, Z. H., KUCHEL, P. W. & CHAPMAN, B. E. 1984. Cell volume dependence of 1 H spin-echo NMR signals in human erythrocyte suspensions: The influence of in situ field gradients.

Biochimica et Biophysica Acta (BBA)-Molecular Cell Research, 803**,** 137-144.

[134] KUCHEL, P. W. & BULLIMAN, B. T. 1989. Perturbation of homogeneous magnetic fields by isolated single and confocal spheroids. Implications for NMR spectroscopy of cells. *NMR in Biomedicine,* 2**,** 151-160.

[135] SONG, Y.-Q., RYU, S. & SEN, P. N. 2000. Determining multiple length scales in rocks. *Nature,* 406**,** 178-181.

[136] HAHN, E. L. 1950. Spin echoes. *Physical review,* 80**,** 580.

[137] CHO, H., RYU, S., ACKERMAN, J. & SONG, Y.-Q. 2009. Visualization of inhomogeneous local magnetic field gradient due to susceptibility contrast. *Journal of Magnetic Resonance,* 198**,** 88-93.

[138] BHAGWANDIEN, R., VAN EE, R., BEERSMA, R., BAKKER, C., MOERLAND, M. & LAGENDIJK, J. 1992. Numerical analysis of the magnetic field for arbitrary magnetic susceptibility distributions in 2D. *Magnetic resonance imaging,* 10**,** 299-313.

[139] CHU, S. C., QIU, H. Z., SPRINGER, C. S. & WISHNIA, A. 1990. Aqueous shift reagents for high-resolution cation NMR. V. Thermodynamics of interaction of DyTTHA 3− with Na+, K+, Mg 2+, and Ca 2+. *Journal of Magnetic Resonance (1969),* 87**,** 287-303.

[140] BOUCHARD, L.-S. & WARREN, W. S. 2004. Reconstruction of porous material geometry by stochastic optimization based on bulk NMR measurements of the dipolar field. *Journal of Magnetic Resonance,* 170**,** 299-309.

[141] DEVILLE, G., BERNIER, M. & DELRIEUX, J. 1979. NMR multiple echoes observed in solid He 3. *Physical Review B,* 19**,** 5666.

[142] SEN, P. N. & AXELROD, S. 1999. Inhomogeneity in local magnetic field due to susceptibility contrast. *Journal of applied physics,* 86**,** 4548-4554.

[143] CHO, H. & SONG, Y.-Q. 2008. NMR measurement of the magnetic field correlation function in porous media. *Physical review letters,* 100**,** 025501.

[144] LISITZA, N. V. & SONG, Y.-Q. 2002. Manipulation of the diffusion eigenmodes in porous media. *Physical Review B,* 65**,** 172406.

Acknowledgements

First of all, I would like to thank to my advisor, HyungJoon Cho for his systematic guide and warm support throughout my combined Master-Doctoral periods. Especially, I always appreciate that my advisor respects my opinion and is willing to discuss about research every time. And thanks for talking about not only work but also personal matter like good father. Also, I would like to thank my dissertation committee members, Professor GilJin Jang, Woongkyu Jung, Taekwan Lee, and SeYoung Chun who gave me professional and prudent feedbacks.

I've been worked in Biomedical Imaging Science and Engineering (BISE) laboratory for almost five years. I thank all lab members to support and be with me for a long time. Specifically, Hoesu Jung is my colleague who joined combined Master-Doctoral course at the same time. I thank for his kindness and listening my troubles without any hesitation. Dongkyu Lee is not only my colleague but also my old friend. I thank for being with me always I do my experiment and spending his time with me gladly. Hansol Lee is my younger brother like family. I thank for sharing his personal matter and advising me to be better, particularly, thank you for caring me in New York City. Seokha Jin is my younger colleague. I thank for discussing about the research freely and giving me an opportunity to play the piano. Minjung Jang is also my younger colleague. I thank for following me enthusiastically in terms of research and giving me a warm tea. MyungSoo Kang is new colleague. I thank for his chocolate and being our lab's new dark horse I think. I wish my all lab members be all right regarding research and personal matter. And I want to support my lab members even after graduating.

And I would like to thank to my cousin, Suin Kim for being with me, caring me when I sick, playing with me, cheering me up when I was down. It was very special time for me and you to spend our graduate school hood together. Especially, playing baseball with you was very meaningful memory for me.

I miss my pet turtles, Whal MyungSoo and Backkus. And I thank for being my pet during my graduate school days. You guys were very nice and gave me happy virus. I believe you guys were also happy being with me and DongKyu Lee. And I thank to my new pet hamster, Bbang E. She gives me energy to have a nice day.

Lastly, I would like to thank to my family members: grandmother, grandfather, father, mother, and my older brother. I really love you guys for supporting me and warm encouragement.